

We are IntechOpen, the world's leading publisher of Open Access books Built by scientists, for scientists

6,300

Open access books available

171,000

International authors and editors

190M

Downloads

Our authors are among the

154

Countries delivered to

TOP 1%

most cited scientists

12.2%

Contributors from top 500 universities



WEB OF SCIENCE™

Selection of our books indexed in the Book Citation Index
in Web of Science™ Core Collection (BKCI)

Interested in publishing with us?
Contact book.department@intechopen.com

Numbers displayed above are based on latest data collected.
For more information visit www.intechopen.com



Introductory Chapter: Production Engineering

Majid Tolouei-Rad

1. Introduction

Production engineering is a broad term covering many activities involved in the production life cycle of industrial products. The term itself is interchangeably used with manufacturing engineering as manufacturing is the backbone of production engineering.

There have been many developments in the domain of production engineering in recent years as reported in the literature. These include developments of new methods in production methods and systems and optimization for improving productivity or maximizing profit. For example, drilling as the most used production process is still the subject of study for improvement by contemporary researchers, and many of these works can be found in the literature [1–8]. There are also reports on the improvements of conventional and nonconventional production processes [9–11], optimization of processes [6, 12, 13], and enhancement of properties [14]. In addition, there are many reports in the literature on the development of production systems including quality control, process planning, and production planning and control systems [15–23].

2. Production processes

As shown in **Figure 1**, production engineering is broadly covering production processes and production systems, and each of these includes various operations. Production processes alter the shape, geometry, and properties of the workpiece enabling it to perform its function. Processing operations may include the enhancement of properties of the workpiece by means of heat treatment operations and improving the quality of the workpiece surfaces using surface processing operations. There is a variety of manufacturing operations including conventional and nonconventional methods. Generally, conventional manufacturing processes are preferred as these are often more economical and the equipment needed is readily available. However, in some cases, the use of nonconventional manufacturing processes is inevitable despite imposing higher costs. For example, **Figure 2** shows a flat metal part with a complex external shape and many internal cut geometries. This part is cut from an 8 mm thickness AISI 304 L stainless steel plate. It is a relatively thick plate of hard-to-machine stainless steel material, making its production problematic using conventional methods. The use of a nonconventional method such as Abrasive Water Jet Machining (AWJM) makes this a relatively easy operation. This part is taken from a research work studying the optimization of AWJM process parameters for improving

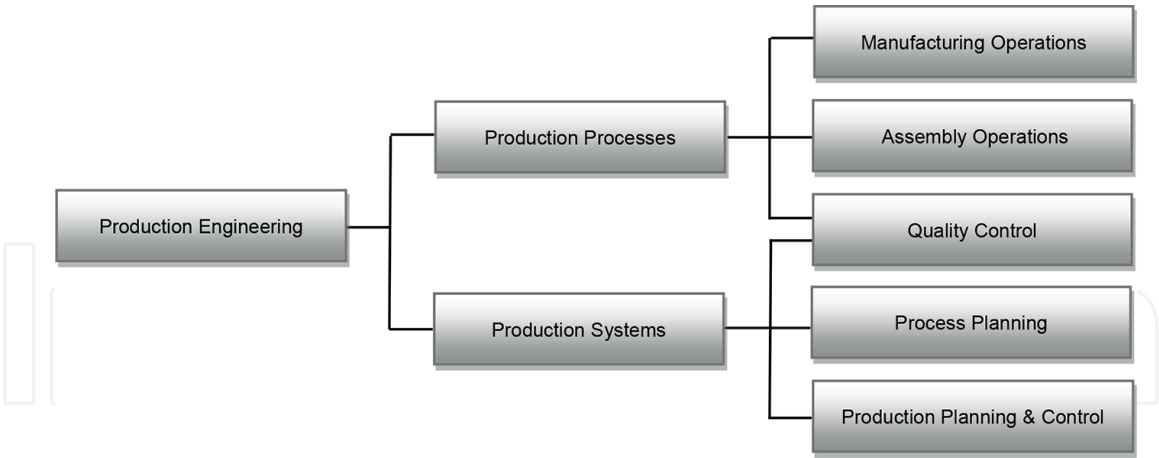


Figure 1.
Classification of activities in production engineering.

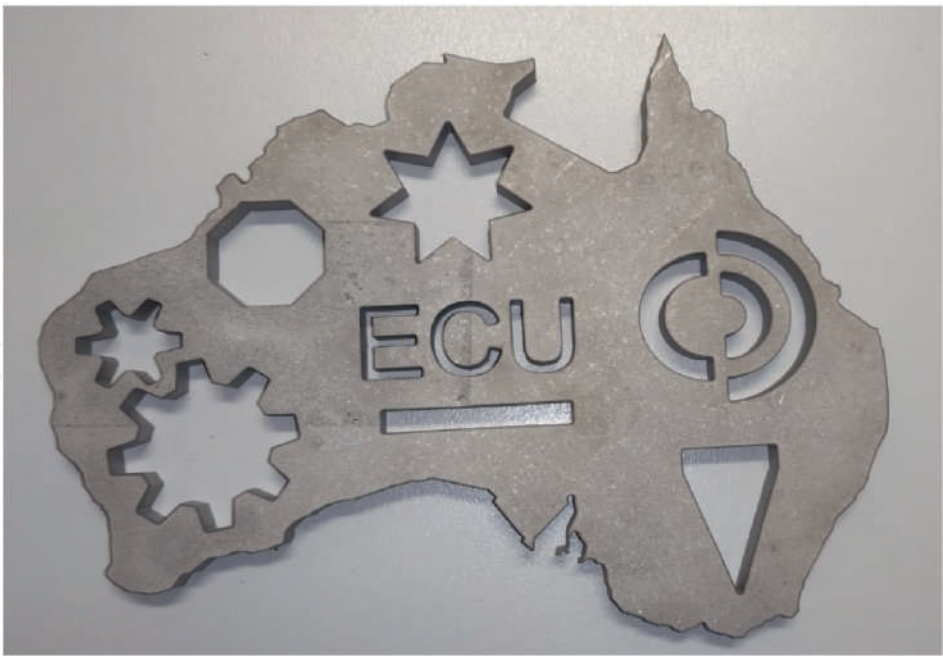
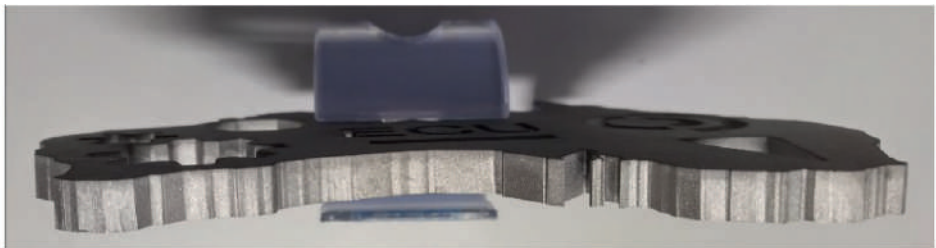


Figure 2.
Map of Australia with embedded geometrical shapes cut from an 8 mm thickness AISI 304 L stainless steel plate using abrasive water jet machining (AWJM). (a) Side view. (b) Top view.

productivity [24]. Another example is shown in **Figure 3** where a complex lattice structure is formed by connecting multiple curved surfaces with thin wall thicknesses. The material of this part is 316 stainless steel which is hard to machine, and

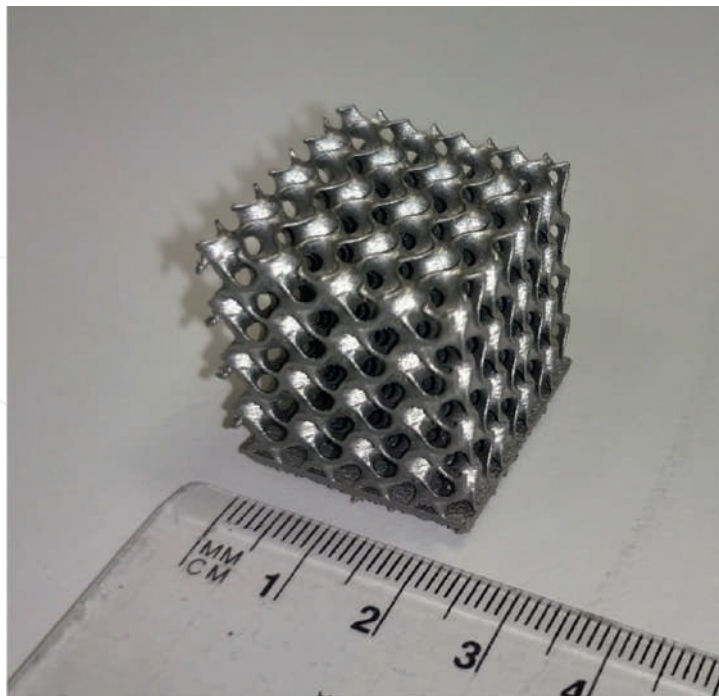


Figure 3.
A lattice structure printed from 316 stainless steel powder using the selected laser melting (SLM) technique.

its complex geometry and small wall thickness make its production impossible with conventional methods. It is produced by additive manufacturing (AM) also known as 3D printing from a powder-like material. This part is printed layer by layer using a layer thickness of 25 micrometers where powder-like metal particles are melted using a powerful laser beam in a process known as selective laser melting (SLM). The process is costly, and the rate of production is low; however, making it possible to produce some complex geometries that would have not been impossible otherwise.

Cutlery items such as spoons and forks are examples of single-part products where no joining or assembly operations are needed after the single-part product is manufactured. However, most products consist of more than one part and there is a need for joining or assembling of these parts. The number of parts in a product where assembly or joining processes are needed can go from two to millions. A screwdriver has 2, a typical car has about 20,000, and the largest passenger aircraft has over 4 million parts that are individually manufactured and assembled to form a complex product with many assemblies and subassemblies. Many types of joining, and assembly operations are used in production plants. Some are permanent joining methods such as welding, brazing, soldering, riveting, and adhesives; and some provide the possibility of disassembly where mechanical fasteners such as bolts and nuts or screws are used.

Quality control is often considered the last step of the production cycle although modern manufacturing strategies state that quality must be built into the product and must be incorporated during manufacturing and assembly operations. In either case, the quality of the product must be tested and verified before it leaves the production plant.

3. Production systems

In general, production processes are referred to those operations where there is a need for physical contact of the product with processing equipment, or the worker;

and a physical contact is not needed when the product is processed by production systems. Although some noncontact quality control methods are used, in most quality control activities there is a need for measuring the dimensional accuracy of the product or its properties requiring physical contact. Yet the quality control information is widely used in production systems for analysis of production where there is no need for physical contact. The assessment of product quality does not end in the production plant and it is still under quality assessment after delivering to the customer and beginning its service life. This is possible by receiving feedback from the customer and also by providing after-sales services. Accordingly, as shown in **Figure 1**, quality control is an activity that relates itself to both production processes and production systems.

In the literature, the production systems are also referred to as manufacturing support systems as processing operations cannot be accomplished without these activities. In addition to quality control, production systems include process planning and production planning and control systems. When a product is to be produced, one of the first steps is to design the product such that it meets the intended specifications. The number of parts, assemblies and subassemblies, processing operations, and equipment should all be identified in an activity known as process planning. Various methods of process planning and the level of detailed information provided on the process sheet varies in different production plants.

Production planning and control (PPC) takes into consideration the logistics problems such as how many products are to be produced in a day or in a year, how long the production line will continue producing the part or product considering market demands, what are the raw material and equipment requirements for responding to production needs, and so on. When production begins there is a need for production control to ensure that production is running smoothly, will be meeting the planned completion dates, and any potential problems that could disrupt a smooth production are identified and tackled.


Author details

Majid Tolouei-Rad

School of Engineering, Edith Cowan University, Joondalup, WA, Australia

*Address all correspondence to: m.rad@ecu.edu.au

IntechOpen

© 2022 The Author(s). Licensee IntechOpen. This chapter is distributed under the terms of the Creative Commons Attribution License (<http://creativecommons.org/licenses/by/3.0>), which permits unrestricted use, distribution, and reproduction in any medium, provided the original work is properly cited. 

References

- [1] Sobri SA, Heinemann R, Whitehead D. Carbon fibre reinforced polymer (CFRP) composites: Machining aspects and opportunities for manufacturing industries. In: *Composite Materials: Applications in Engineering, Biomedicine and Food Science*. Cham: Springer International Publishing; 2020. pp. 35-65
- [2] Aamir M, Tolouei-Rad M, Giasin K. Multi-spindle drilling of Al2024 alloy and the effect of TiAlN and TiSiN-coated carbide drills for productivity improvement. *The International Journal of Advanced Manufacturing Technology*. 2021;**114**(9):3047-3056
- [3] Tolouei-Rad M, editor. *Drilling Technology*. London, UK: IntechOpen; 2021 [Online]. Available from: <https://www.intechopen.com/books/10375>. DOI: 10.5772/intechopen.91561
- [4] Tolouei-Rad M, Aamir M. Introductory chapter: Drilling technology. In: *Drilling Technology*. London, UK: IntechOpen; 2021 [Online]. Available: <https://www.intechopen.com/chapters/76535>. DOI: 10.5772/intechopen.97648
- [5] Tolouei-Rad M, Aamir M. Analysis of the performance of drilling operations for improving productivity. In: *Drilling Technology*. London, UK: IntechOpen; 2021 [Online]. Available: <https://www.intechopen.com/chapters/75613>. DOI: 10.5772/intechopen.96497
- [6] Vafadar A, Hayward K, Tolouei-Rad M. Drilling reconfigurable machine tool selection and process parameters optimization as a function of product demand. *Journal of Manufacturing Systems*. 2017;**45**:58-69
- [7] Tolouei-Rad M, Shah A. Development of a methodology for processing of drilling operations. *International Journal of Industrial and Manufacturing Engineering*. 2012;**6**(12):2660-2664
- [8] Aamir M, Giasin K, Tolouei-Rad M, Ud Din I, Hanif MI, Kuklu U, Pimenov DY, Ikhlaiq M. Effect of cutting parameters and tool geometry on the performance analysis of one-shot drilling process of AA2024-T3. *Metals*. 2021;**11**(6):854
- [9] Sahoo SP, Pandey K, Datta S. Performance of uncoated/coated carbide inserts during MQL (sunflower oil) assisted machining of Inconel 718 superalloy. *Sādhanā*. 2022;**47**(4):1-31
- [10] Jalali Azizpour M, Tolouei-Rad M. Evaluation of residual stress in HVOF stellite-6 coatings using non-contact drilling. *Materials Research Express*. 2019;**6**(6):066577
- [11] Xu M, Wei R, Li C, Kurniawan R, Chen J, Ko TJ. Comprehensive study on the cutting force modeling and machinability of high frequency electrical discharge assisted milling process using a novel tool. *International Journal of Precision Engineering and Manufacturing-Green Technology*. 2022;**15**:1-28
- [12] Aamir M, Tu S, Tolouei-Rad M, Giasin K, Vafadar A. Optimization and modeling of process parameters in multi-hole simultaneous drilling using taguchi method and fuzzy logic approach. *Materials*. 2020;**13**(3):680
- [13] Tolouei-Rad M, Bidhendi IM. On the optimization of machining parameters for milling operations. *International Journal of Machine Tools and Manufacture*. 1997;**37**(1):1-6

- [14] Tolouei-Rad M, Lichter E. The heat treatment analysis of e110 case hardening steel. *Journal of Engineering Science and Technology*. 2016;**11**(3):407-415
- [15] Muthiah KM, Huang SH. A review of literature on manufacturing systems productivity measurement and improvement. *International Journal of Industrial and Systems Engineering*. 2006;**1**(4):461-484
- [16] Tolouei-Rad M. Integration of part classification, cell formation and capacity adjustment. *Journal of Achievements in Materials and Manufacturing Engineering*. 2010;**39**(2):197-203
- [17] Tamás P, Illés B. Process improvement trends for manufacturing systems in industry 4.0. *Academic Journal of Manufacturing Engineering*. 2016;**14**(4):119-125
- [18] Tolouei-Rad M. Intelligent analysis of utilization of special purpose Machines for Drilling Operations. In: *Intelligent Systems*. London, UK: IntechOpen; 2012 [Online]. Available: <https://www.intechopen.com/chapters/30663>. DOI: 10.5772/36896
- [19] Zhao C, Li J, Huang N. Efficient algorithms for analysis and improvement of flexible manufacturing systems. *IEEE Transactions on Automation Science and Engineering*. 2015;**13**(1):105-121
- [20] Tolouei-Rad M. An efficient algorithm for automatic machining sequence planning in milling operations. *International Journal of Production Research*. 2003;**41**(17):4115-4131
- [21] Robinson A. *Modern Approaches to Manufacturing Improvement: The Shingo System: The Shingo System*. New York, USA: Routledge; 2017
- [22] Mula J, Poler R, García-Sabater JP, Lario FC. *Models for production planning under uncertainty: A review*. *International Journal of Production Economics*. 2006;**103**(1):271-285
- [23] Kang CW, Ramzan MB, Sarkar B, Imran M. Effect of inspection performance in smart manufacturing system based on human quality control system. *The International Journal of Advanced Manufacturing Technology*. 2018;**94**(9):4351-4364
- [24] Llanto JM, Vafadar A, Tolouei-Rad M. Multi-objective optimisation in abrasive waterjet contour cutting of AISI 304L. In: *Production Engineering [Working Title]*. London, UK: IntechOpen; 2022 [Online]. Available: <https://www.intechopen.com/online-first/83563>. DOI: 10.5772/intechopen.106817

We are IntechOpen, the world's leading publisher of Open Access books Built by scientists, for scientists

6,300

Open access books available

171,000

International authors and editors

190M

Downloads

Our authors are among the

154

Countries delivered to

TOP 1%

most cited scientists

12.2%

Contributors from top 500 universities



WEB OF SCIENCE™

Selection of our books indexed in the Book Citation Index
in Web of Science™ Core Collection (BKCI)

Interested in publishing with us?
Contact book.department@intechopen.com

Numbers displayed above are based on latest data collected.
For more information visit www.intechopen.com



Multi-objective Optimisation in Abrasive Waterjet Contour Cutting of AISI 304L

Jennifer Milaor Llanto, Ana Vafadar and Majid Tolouei-Rad

Abstract

The optimum waterjet machining parameters were found for maximising material removal rate and minimising surface roughness and kerf taper angle where three levels of traverse speed, abrasive flow rate, and waterjet pressure are used. The multi-linear regression equations were obtained to investigate the relationships between variables and responses, and the statistical significance of contour cutting parameters was analysed using the analysis of variance (ANOVA). Further, the response surface methodology (desirability function approach) was utilised for multi-objective optimisation. The optimum traverse speeds were 95 mm/min for 4 mm thickness and 90 mm/min for both 8 and 12 mm thicknesses. For all material thicknesses, the abrasive mass flow rate and waterjet pressure were 500 g/min and 200 MPa, respectively. The minimum values of surface roughness, kerf taper angle, and maximum material removal rate for 4-, 8- and 12-mm material thicknesses were respectively 0.799°, 1.283 μm and 297.98 mm^3/min ; 1.068°, 1.694 μm and 514.97 mm^3/min ; and 1.448°, 1.975 μm and 667.07 mm^3/min . In this study, surface roughness and kerf taper angle decreased as the waterjet pressure and abrasive mass flow rate increased; and this is showing a direct proportional relationship with traverse speed, abrasive mass flow rate and waterjet pressure.

Keywords: abrasive water jet, contour cutting, surface roughness, kerf taper angle, material removal rate, response surface methodology, multi-objective optimisation

1. Introduction

Contour cutting is one of the processes applied in metal fabrication industries. There are several non-traditional technologies employed for contour cutting, such as electro discharge machining, laser beam machining and electrochemical discharge machining, that have been noted to provide exemplary performance [1]. Accordingly, Abrasive Water Jet Machining (AWJM) is an advanced manufacturing techniques that demonstrated advantages to non-traditional machining technology owing to: its capability in cutting complex geometries, its absence of tool wear, its absence of thermal distortion, and it being environmentally friendly [2, 3]. The cutting process in AWJM is based on removing materials from a target workpiece via erosion [4]. Within this process, contour profiles in various types of programs are downloaded in a

computer-based controller, where subsequently a high-pressure pump releases pressurised water in the nozzle system. The pressurised water, moving with a high velocity, is released from the orifice in a very thin stream structure [5]. The high-speed water jet that contains abrasive particles is then accelerated to generate an abrasive waterjet. Finally, the focusing tube drives the abrasive waterjet to its target point for cutting the material [4, 6]. The compounded granular abrasive and high-pressure waterjet stream makes the abrasive waterjet capable of machining various workpieces, such as metals.

The performance of AWJM is influenced by several process parameters, which can be varied constantly within a period. In general, the primary goal of the metal fabrication industry is to manufacture high quality products in a shortened period. To attain productivity and economy objectives, it is imperative to select an optimum combination of process parameters within the abrasive waterjet cutting processes. Conventionally, the identification of the most suitable values of process parameters is accomplished by the execution of many experiments. Hence, to establish the optimum combination of process parameters in the absence of extensive experimental exertion, researchers have utilised advanced modelling techniques and optimisation in progressing the performance of abrasive waterjet cutting. For instance, Rao et al. [7] have investigated the impacts of traverse speed, standoff distance and abrasive mass flow rate in AWJM of AA631-T6. They have considered single-objective and multi-objective optimisation attributes to achieve optimum solutions by utilising Jaya and MO-Jaya algorithms, which were a posterior optimisation used to solve constrained and unconstrained conditions. The objectives of maximising material removal and minimising kerf taper angle and surface roughness were achieved by lower traverse speed and standoff distance and higher abrasive mass flow rate. Moreover, they determined that multi-objective Jaya algorithm achieved better results as compared with other algorithms, such as simulated annealing (SA), particle swarm optimization (PSO), firefly algorithm (FA), cuckoo search (CS) algorithm, blackhole (BH) algorithm, bio-geography-based optimization (BBO) algorithm, non-dominated sorting genetic algorithm (NSGA), non-dominated sorting teaching-learning-based optimization (NSTLBO) algorithm and sequential approximation optimization (SAQ). Nair and Kumanan [8] have similarly applied weighted principal components analysis (WPCA) for optimising AWJM process parameters in machining Inconel 617. These authors evaluated the impacts of abrasive mass flow rate, standoff distance, table feed and waterjet pressure against material removal rate and geometric accuracy. The WPCA method uses internal tests and training samples to calculate the 'weighted' covariance matrix, establishing that an increase in standoff distance enhances the abrasive flow volume, leading to less geometric errors and a higher rate of material removal. Equivalently, Chakraborty and Mitra [9] have applied the grey wolf optimiser (GWO) technique for AWJM cutting of AL6061 to maximise material removal rate and minimise surface roughness, simultaneously considering the constrained values of input parameters i.e., nozzle diameter and titled angle, jet feed speed, surface speed, waterjet pressure and abrasive mass flow rate. This algorithm demonstrated a faster hunting of prey (discovering the optimum parameter settings), due to the existence of a social hierarchy of grey wolves. They achieved maximum MRR via higher rate of nozzle titled angle, surface speed, waterjet pressure and abrasive mass flow rate. In the case of surface roughness, it attained its minimum value at lower rate of waterjet pressure, jet feed and surface speed and higher rate of abrasive mass flow. Trivedi et al. [10] have examined the impacts of process parameters such as pressure, traverse rate and standoff distance on surface integrity in AWJM

of AISI 316 L. Analysis of variance was employed to develop an empirical model by regression analysis for surface roughness. These authors concluded traverse speed to be the most significant parameter influencing surface roughness, whereby increasing pressure improved the surface quality of the target workpiece. Additionally, they established standoff distances, as the least contributing parameter. Research focused on optimisation of cutting operations is being continuously undertaken by researchers, where varied methods have been employed to solve different single and multi-objective optimisation problems [11–14]. Whereas single-objective optimisation problems have conventionally been applied, the performance of AWJM has mainly been measured based on multiple responses. In accordance, a multi-objective approach is required in order to optimise several categories of objective functions simultaneously. Several methods have been developed to date, and are continuously being progressed, in order to solve single-objective problems. Advances in optimisation techniques, such as: genetic algorithms (GA), simulated annealing (SA), artificial bee colony (ABC), ant colony optimization (ACO), particle swarm optimization (PSO) and teaching-learning-based optimization (TLBO), and others, have been demonstrated to be remarkably efficient in defining the optimum value of AWJM process parameters [15].

In abrasive waterjet contour-cutting, it has been realised that the impacts of most influencing factors, such as waterjet pressure, abrasive mass flow rate, standoff distance and traverse speed in straight-slit cutting, are similar with contour cutting. These research studies have shown the application of computational approaches for optimising process parameters in abrasive waterjet contour cutting requires further investigation. Therefore, this research considers the optimisation of relevant process parameters, including traverse speed, abrasive mass flow rate, and waterjet pressure on surface roughness, material removal rate and kerf taper angle in abrasive waterjet contour cutting of AISI 304L of varied thicknesses.

In this work, the experiment was designed using Taguchi orthogonal array, where a regression model has been developed to formulate the optimisation fitness function. This modelling technique has been applied to predict the response and determine optimum process parameters. In addition, response surface methodology (RSM) has been employed for multi-objective optimization, in order to obtain optimum values of input process parameters and to investigate the impacts and interactions against response parameters.

2. Methodology

In this study, three major steps were employed, consisting of abrasive waterjet contour cutting experiments, regression modelling and optimisation. The experiment, modelling and optimisation procedures are presented in **Figure 1**. The experiment was conducted using the Taguchi L₉ orthogonal array to analyse the impacts of input parameters, i.e., traverse speed, abrasive mass flow rate and waterjet pressure. Desirability analysis using response surface methodology is employed for the experimental results of material AISI 304L. In this desirability analysis, multi-responses are considered. It establishes the optimum set of the selected process parameters on the performance characteristics.

A regression model was developed using the machining process parameters from the experimental execution to extract mathematical models. A linear stepwise regression analysis was performed to predict the surface roughness, material removal rate

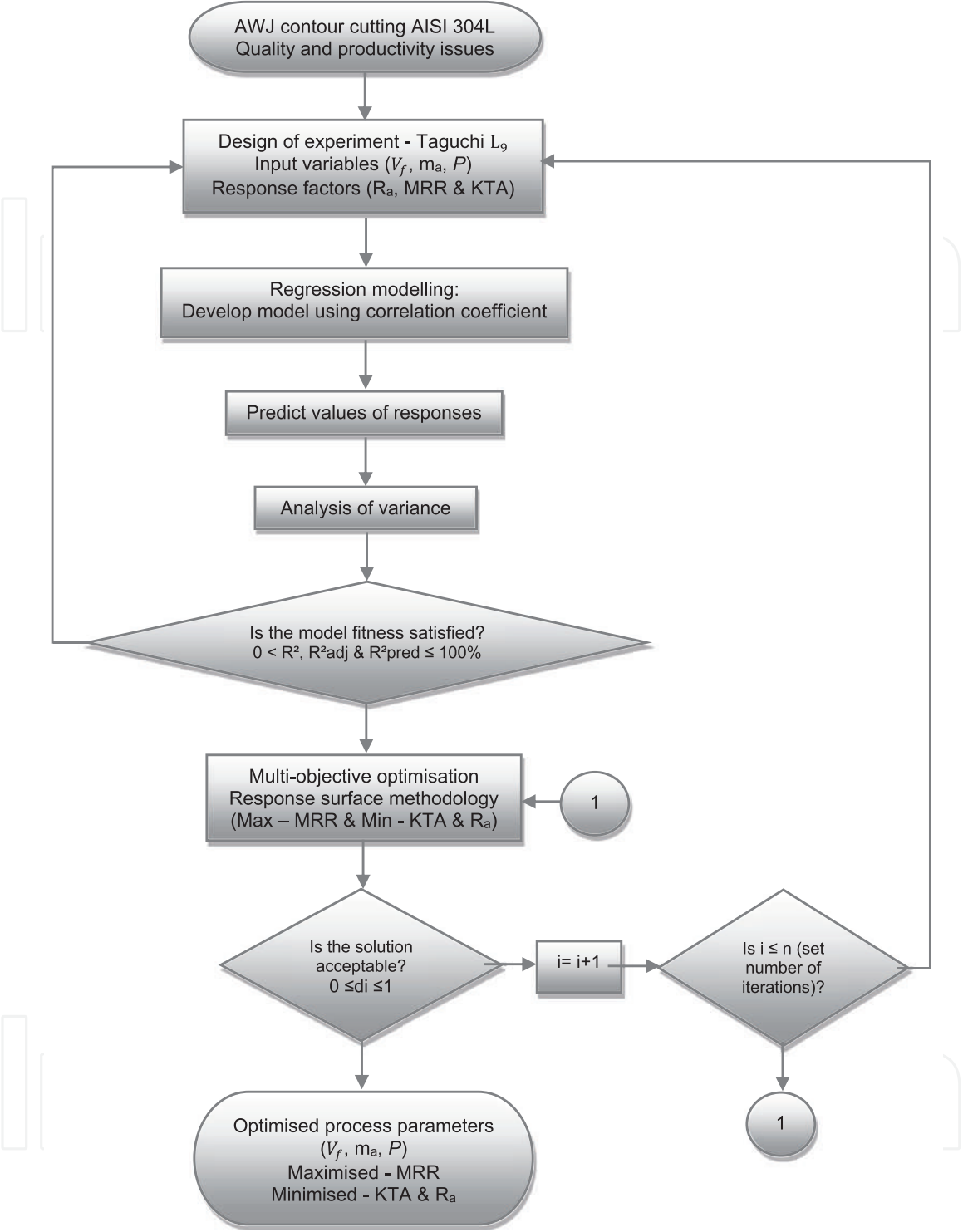


Figure 1.
Multi-objective optimisation process flow chart.

and kerf taper angle value. The reliability of the models generated was assessed based on coefficient of determination (R^2 , R^2_{adj} & R^2_{pred}). However, supposing that regression models are not within the acceptable range or do not provide preferable values of coefficients of determination set by the decision-maker, it is anticipated that these models will not provide precise prediction. Therefore, the selected parameter setting conflicts with the response variables, denoting the necessity for modification of independent variables or experimental design [16].

Referring to **Figure 1**, after achieving the fittest models, a multi-objective optimisation was performed by using response surface methodology with the objectives of maximising material removal, whilst minimising surface roughness and kerf taper angle. The number of solutions and iterations ($i = 1$ to n) may vary, depending on the machining process requirements to establish the best alternative or solution. Hence, if the composite desirability is not within the tolerable array, several iterations repeating the response surface optimisation were executed. Subsequently, if these repetitions reached the maximum number of iterations and the composite desirability is not attaining adequate values, modifying the design of experiments and the corresponding independent variables or its values is necessary [16]. Moreover, in some cases, other soft computing techniques should be considered [17].

2.1 Material and experimental design

In this work, the material machined in the experiments was AISI 304L with varied thicknesses of 4, 8 and 12 mm. The assigned material thicknesses with differing uniform gaps were used to gain a better yield of variations in AWJM cutting behaviour. Stainless steel, such as AISI 304L, is widely used in fabrication industries, where it is recognised for its high strength and corrosion and heat resistance. This results from its high alloying content of Cr and Ni [18]. The chemical and mechanical composition of this material is detailed in **Table 1**.

The setup consisted of an OMAX MAXIEM 1515 abrasive waterjet machine, possessing a direct drive pump and dynamic cutting head with maximum pressure of 413.7 MPa and cutting area of 2235 mm length and 1727 mm width. The cutting head is comprised of a mixing chamber for abrasive and waterjet, along with a nozzle diameter of 0.56 mm and a jet impact angle of 90°. An abrasive garnet with a mesh size of #80 was utilised for abrasive waterjet cutting experiments. The unit is inclusive of IntelliMax software, where the experiment setup conditions were uploaded and entered. The cutting head can move in the Z-axis over a distance of 305 mm, with a maximum traverse speed of 12,700 mm/min. Standoff distance was designated to 1.5 mm in agreement with recommended range for abrasive waterjet machining in previous works [20, 21]. The AWJM setup and process parameters are demonstrated in **Figure 2**.

Chemical composition in wt.%		Mechanical properties	
C	0.03	Hardness, Rockwell B	82
Mn	2	Tensile Strength, Ultimate, MPa	564
Si	0.75	Tensile Strength, Yield, MPa	210
Cr	18.00–20.00	Elongation at Break	58%
Ni	8.00–12.00	Modulus of Elasticity, GPa	193–200
P	0.045		
S	0.03		
Ni	0.1		
Fe	Remaining		

Table 1.
Chemical and mechanical composition of AISI 304L [19].

Upon completion of the experiments, the roughness of the machined surfaces was quantified by a surface roughness tester (TR200 model). **Figure 2** presents the cut surface captured by LEICA M80, which indicates the measurement area for the roughness. The kerf top and bottom width were measured using a LEICA M80 optical microscope model. Moreover, rate of material removal and kerf taper angle were calculated using Eqs. (1) and (2), respectively [11]. The roughness of the cut surface determined according to the ISO/TC 44 N 1770 standard, (μm); W_t is width of the cut surface at the jet inlet, (mm); W_b is the width of the cut surface at the jet outlet, (mm); u is the angularity or perpendicular deviation, (mm); α° - inclination angle of the cut surface, ($^\circ$); MRR is the Material Removal Rate, (mm^3/min); t is the thickness of the material (mm) [22].

$$MRR = ht \left(\frac{W_t + W_b}{2} \right) V_f \quad (1)$$

$$KTA = \text{Arctan} \left(\frac{W_t + W_b}{2ht} \right) \quad (2)$$

The input parameters considered in abrasive waterjet contour cutting in this experiment included traverse rate (V_f), abrasive flow rate (m_a) and water pressure (P), as these parameters have been demonstrated in previous studies as having significant impacts in AWJM applications [10, 12, 23, 24]. Surface integrity, kerf geometries

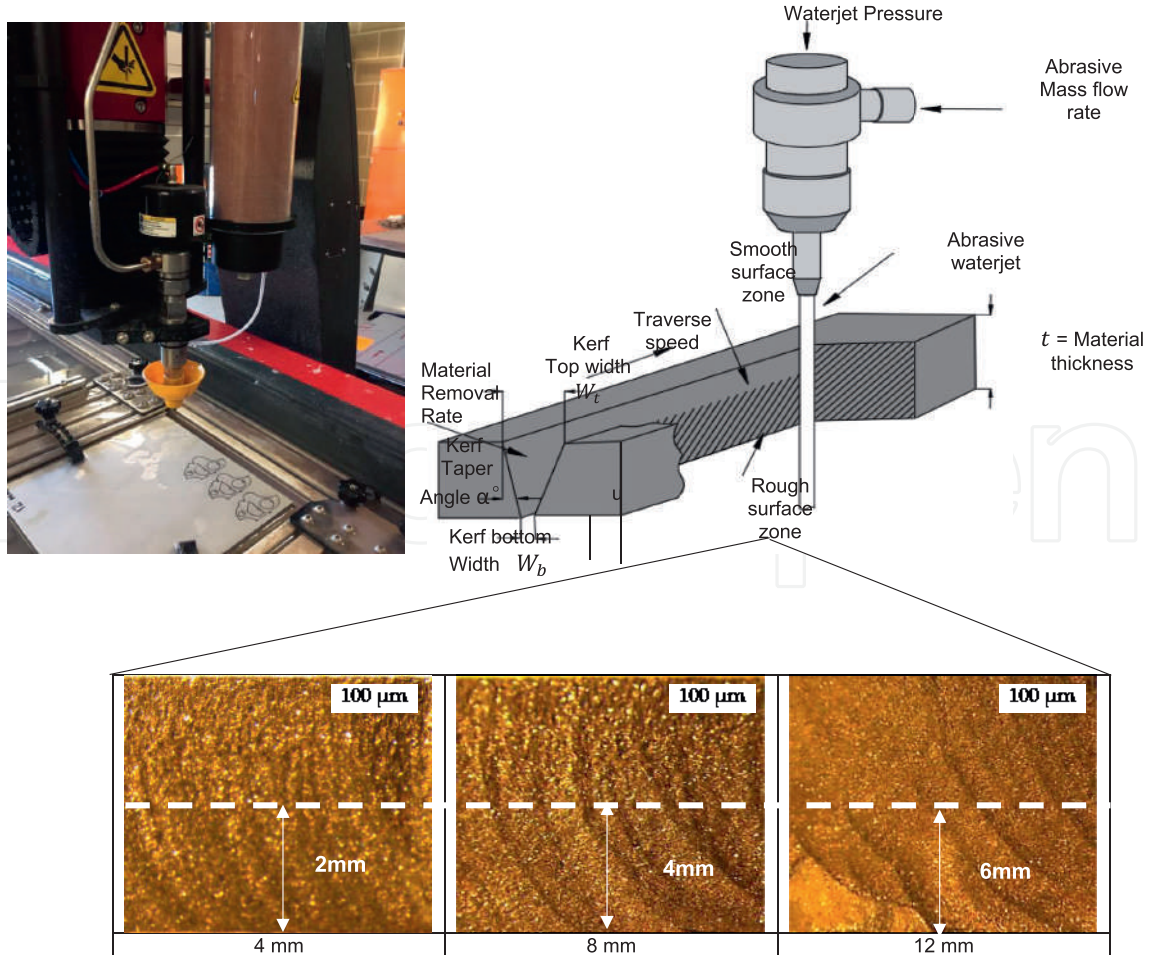


Figure 2.
AWJM setup and process parameters.

and low material removal rate evidence has been reported in machining of AISI 304L, requiring further improvement [4, 25]. Furthermore, taper angles formed in AWJM demonstrate different inclinations as contour curvature radius differs [26]. Hence, quality and productivity are an intensified demand in various manufacturing fields and are significant performance indicators for machining processes. Therefore, in this study, material removal rates (MRR), surface roughness (R_a) and kerf taper angle (KTA) have been chosen as process parameter characteristics for abrasive waterjet contour cutting investigations, due to their influence against the selected input parameters. The levels of the considered independent variables, responses and coding assignment have been detailed in **Tables 2** and **3**.

Abrasive waterjet cutting was executed for three different profiles, representing straight-line, inner arcs and outer arcs, as part of the completed twelve profiles, as demonstrated in **Figure 2**. The abovementioned profiles were selected to confirm a broad array of complicated machining profiling applications. The levels of profiles employed showed occurrences of surface roughness, low machining rate and inaccuracies of cut geometries in regard to previous works [27, 28], recommending further studies, predominantly for difficult-to-cut materials, such as AISI 304L (**Figure 3**).

The design of experimentation (DOE) was carried out using the Taguchi approach in MINITAB 19 software. The Taguchi method is useful in determining the best combination of factors under desired experimental conditions, reducing the large number of experiments which would be required in traditional experiments as the number of process parameter increases [29, 30].

In Taguchi's approach, selection of the appropriate orthogonal array depends on aspects such as: the number of input and response factors along with the interactions that are of key significance; number of levels of data for input factors; and required resolution of experiment and limitations cited on cost and performance [29, 31]. With this specific advantage, this method is suitable in conducting experiments with an appropriate number of tests to determine the optimal combination and significance of the selected factors [32]. The relevant variation in thicknesses dictates different material responses. Therefore, Taguchi L_9 orthogonal array was executed for three

Independent variables	Codes	Levels		
		1	2	3
Traverse speed, V_f = mm/min	X_1	90	120	150
Abrasive mass flow rate, m_a = g/min	X_2	300	400	500
Waterjet pressure, P = MPa	X_3	200	250	300

Table 2.
Levels of input process parameters.

Profiles	Surface roughness, μm	Material removal rate, mm^3/min	Kerf taper angle, $^\circ$
Straight-line, 20 mm	R_{a1}	MRR1	KTA1
Inner arc, R10	R_{a2}	MRR2	KTA2
Outer arc, R20	R_{a3}	MRR3	KTA3

Table 3.
Output parameters for varied profiles.

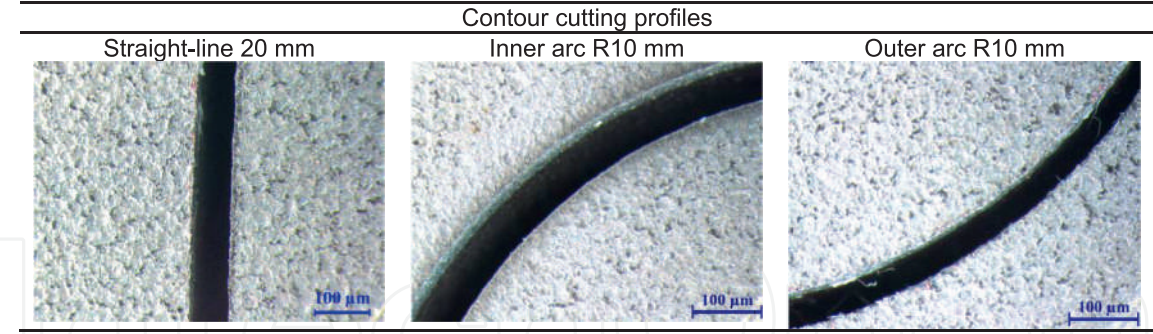


Figure 3.
Abrasive waterjet contour cutting profiles.

Exp. No.	Input Parameters		
	V_f	m_a	P
	(mm/min)	(g/min)	(MPa)
1	90	300	200
2	90	400	250
3	90	500	300
4	120	300	250
5	120	400	300
6	120	500	200
7	150	300	300
8	150	400	200
9	150	500	250

Table 4.
Taguchi L_9 orthogonal array.

levels of material thicknesses (t), i.e., 4, 8 and 12 mm, as presented in **Table 4**. The AWJM performances were analysed accordingly by the applied material thickness.

2.2 Modelling and multi-objective optimisation

A mathematical model was developed to associate the input process parameters to the response’s characteristics. To achieve this, a linear regression was employed to develop models for the prediction of responses. The empirical model for the prediction of the responses in regard to controlling parameters was established by linear regression analysis. Regression analysis was then applied to obtain the interactions between independent and dependent variables [33]. Multi-linear regression involves regression analysis of dependent and independent variables exhibiting a linear relationship [34]. It stipulates the relationship between two or more variables and a response variable by fitting a linear equation to examine data. The value of the independent variable x or process parameter is correlated with a value of the dependent variable, y , which is the output parameter. In general, this analysis is applied to investigate the degree of relationship between multiple variables fitted by a straight line [33].

In general, regression model is expressed by Eq. (3) [33].

$$y = \alpha + \beta_1 x_1 + e \quad (3)$$

$$\text{Wherein : } e = y_1 - \hat{y}_1 \quad (4)$$

where, y = dependent variable, α = constant, x_1 = Independent variable, β_1 = coefficient of independent variable x_1 , e = error, y_1 = regression line values and \hat{y}_1 = actual observation.

If this involves more than one variables, then it is categorised as multi-regression as shown in Eq. (5) [33].

$$y = \alpha + \beta_1 x_1 + \beta_2 x_2 + \beta_3 x_3 + \dots \dots \dots \beta_n x_n + e_n \quad (5)$$

A multi-linear regression analysis can be employed to fit a predictive model to an observed data set of values of output and input variables. The obtained results of surface roughness, material removal rate and kerf taper angle were expressed in terms of the input parameters such as traverse speed (X_1) abrasive mass flow rate (X_2) and waterjet pressure (X_3).

The predicted values are functional for optimising the parameters by providing an adequate comprehension of the significant parameters. The percentage of error between the experimental data and acquired predicted values has been calculated based on Eq. (6) [33]. The relative percentage of error was acceptable at <20% [35].

$$\text{Error} = \frac{1}{n} \sum_n \left[\frac{\text{Response}_{(\text{experiment})} - \text{Response}_{(\text{predicted})}}{\text{Response}_{(\text{experiment})}} \right] \% \quad (6)$$

The performance of the established regression model was assessed by statistical approaches to confirm the goodness-of-fit of the model and the impact of the predicted variables. Following this, the significance and effectiveness of the developed models were validated by *analysis of variance*. *Analysis of variance (ANOVA)* is a statistical method that facilitates the evaluation of comparative influences for each control parameter [36, 37]. The significance of input parameters including traverse speed, abrasive mass flow rate and waterjet pressure were investigated using p - values and determination of coefficient (R^2). In this work, a confidence interval of 95% ($p < 0.05$) has been applied that is in alignment with previous works [29, 38, 39]. A 95% confidence interval means that there is only a 5% chance of being the wrong estimation; therefore, the influence of each process parameter or other interactions on the responses is considered insignificant if their p -values were estimated at more than 0.05 [37].

The determination of coefficient (R^2 , R^2_{adj} and R^2_{pred}) refers to the percentage variation of responses ranging from 0–100%. These indicators determine the adequacy of the model against obtained experimental data and predicted observation. This R^2 , R^2_{adj} and R^2_{pred} value of $\geq 80\%$, proved a better model fits of the obtained data [35].

Response surface methodology (RSM) can be utilised for multi-objective optimisation. This multi-desirability is based on multi-response optimisation using an objective function $D(X)$, denoted as desirability function [40]. This method translates each response (y_i) into a desirability function (d_i), differing in the array of $0 \leq d_i \leq 1$,

where desirability function =0 indicates an undesirable response and desirability function =1 represents a fully desired response [41]. The objective function D is specified by Eq. (7) [40].

$$D = (d_1 \times d_2 \times \dots \times d_n)^{1/n} = \left(\prod_{i=1}^n d_i \right)^{1/n} \quad (7)$$

The effectiveness of multi-objective optimisation is anticipated based on the method used for establishing priority weights for each response characteristics [42]. Generally, equal importance is set for selected responses; hence, weights may differ depending on the machining process requirements in order to establish the most suitable solution [43].

A simultaneous optimisation process was employed to determine the levels of resulting to the maximum overall desirability. The responses namely R_a , MRR and KTA were optimised concurrently to assess the set of input process parameters with the objectives of maximising MRR and minimising R_a and KTA.

3. Results and discussion

3.1 Regression models and analysis for surface roughness

The multi-linear regression coefficients are summarised in **Table 5**, exhibiting the correlation between the input parameters and the output surface roughness for straight-line, inner and outer arc profiles for material thicknesses of 4, 8 and 12 mm. The values of coefficients for all profiles and thicknesses demonstrate a similar trend, showing that constant and variable X_1 is positive and variables X_2 and X_3 are negative. The coefficient indicates the change in the mean response relating in the variation of the specific term, whilst the other term in the model remains constant. The relationship between a term and response is denoted by the sign of the coefficient [44]. The negative correlation coefficient denotes an inverse relationship between variables and responses; and therefore, if it is positive as the coefficient increases, the response mean value also increases. Therefore, an increasing rate of traverse speed (X_1) results in an incremental value of surface roughness. Moreover, an increasing rate of abrasive mass flow and waterjet pressure indicates/obtains a decreasing value of surface roughness. The values of R^2 , R^2_{adj} and R^2_{pred} for 4, 8 and 12 mm ranged from 94.33–99.08%, 90.94–98.52% and 88.66–96.17%, respectively. This indicates that regression models denote an acceptable confirmation of the relationship between the independent variables and R_a response, which denotes a high significance of the model. Therefore, the multi-linear model is reliable and can be utilised in the optimisation of process parameters. It can be observed that the R^2 , R^2_{adj} and R^2_{pred} obtained from straight-line, inner and outer arcs profiles have a uniform gap of at least 2%, which is comparable for all material thicknesses. Hence, this minimal gap denotes an insignificant difference between the surface roughness achieved from straight and curvature profiles [36].

The results detailed in **Table 5** show that the highest value of R^2 , R^2_{adj} and R^2_{pred} for 4 and 8 mm material thickness are achieved in R_{a3} with the values of 97.26, 94.84 and 92.45%; 98.64, 97.82 and 95.06%; 99.08, 98.52 and 96.17% respectively. Thus, R_{a2} achieved the highest percentage of R^2 , R^2_{adj} and R^2_{pred} for 12 mm material thickness

Term	<i>t</i> = 4 mm			<i>t</i> = 8 mm			<i>t</i> = 12 mm		
	R _{a1}	R _{a2}	R _{a3}	R _{a1}	R _{a2}	R _{a3}	R _{a1}	R _{a2}	R _{a3}
	Coef	Coef	Coef	Coef	Coef	Coef	Coef	Coef	Coef
	1.418	1.5394	1.4256	2.097	1.8107	1.76	2.542	2.3854	2.272
β_1	0.003522	0.002944	0.003222	0.009814	0.003483	0.008869	0.005389	0.004276	0.003090
β_2	- 0.000310	- 0.000300	- 0.000217	- 0.001464	- 0.000422	- 0.000577	- 0.000450	- 0.000446	- 0.000515
β_3	- 0.001500	- 0.001300	- 0.001133	- 0.001955	- 0.000977	- 0.001920	- 0.002567	- 0.001924	- 0.001081
Model Summary									
R ²	95.26%	96.77%	97.26%	98.01%	98.16%	98.64%	97.73%	99.08%	94.33%
R ² (adj)	92.41%	92.41%	94.84%	96.82%	97.05%	97.82%	96.37%	98.52%	90.94%
R ² (pred)	90.58%	90.58%	92.45%	93.84%	93.77%	95.06%	93.33%	96.17%	88.66%

Table 5.
Summary of multi-linear regression coefficients for R_a.

with the values of 99.08%, 98.52% and 96.17% accordingly. Therefore, the most fitted and predominant models were R_{a3} for both 4 and 8 mm, and R_{a2} for 12 mm material thickness. The predicted R_a values of regression models applied for straight-line, inner and outer arcs profiles of three levels of material thicknesses are detailed in **Tables 6-8**. The percentage error obtained for 4, 8 and 12 mm AISI 304L thicknesses ranged from -4.22 to 3.44% , 3.30 to 6.71% and -5.75 to 2.49% , respectively. The errors determined for R_a between the predicted value and experimental results are less than 20%, denoting that these models are reliable for predicting R_a values.

Figure 4 presents the residual plot for R_a , consisting of normal probability plot, residual versus fits, histogram for residuals and residuals versus experimental values for the most fitted regression models for 4, 8 and 12 mm, at R_{a3} , R_{a3} and R_{a2} , respectively. Similarly, the normal probability plots for all the material thicknesses demonstrated a close fit to a line in a normal probability graph. The points forming an

Exp. no.	Independent variables			R_{a1} (μm)			R_{a2} (μm)			R_{a3} (μm)		
	X_1	X_2	X_3	Exp.	Pred.	Error %	Exp.	Pred.	Error %	Exp.	Pred.	Error %
1	90	300	200	1.35	1.34	0.81	1.43	1.42	0.61	1.46	1.45	0.56
2	90	400	250	1.25	1.24	1.41	1.33	1.35	-1.56	1.37	1.36	1.06
3	90	500	300	1.09	1.13	-3.99	1.25	1.27	-1.72	1.24	1.26	-2.44
4	120	300	250	1.36	1.37	-1.26	1.46	1.46	-0.39	1.48	1.48	0.22
5	120	400	300	1.29	1.27	2.35	1.42	1.39	3.44	1.40	1.38	1.72
6	120	500	200	1.41	1.39	2.45	1.50	1.48	2.28	1.48	1.48	-0.28
7	150	300	300	1.41	1.40	0.68	1.50	1.50	-0.39	1.49	1.50	-1.11
8	150	400	200	1.48	1.52	-4.22	1.58	1.60	-1.56	1.58	1.60	-2.11
9	150	500	250	1.43	1.42	1.77	1.51	1.52	-0.72	1.53	1.51	2.39

Table 6.
Predicted R_a values of regression models for $t = 4$ mm.

Exp. no.	Independent variables			R_{a1} (μm)			R_{a2} (μm)			R_{a3} (μm)		
	X_1	X_2	X_3	Exp.	Pred.	Error %	Exp.	Pred.	Error %	Exp.	Pred.	Error %
1	90	300	200	2.12	2.15	-3.30	1.81	1.80	1.06	2.01	2.00	0.47
2	90	400	250	1.88	1.91	-2.73	1.72	1.71	0.86	1.86	1.85	0.98
3	90	500	300	1.64	1.66	-2.16	1.60	1.62	-2.04	1.65	1.69	-4.40
4	120	300	250	2.41	2.35	6.71	1.84	1.86	-1.81	2.16	2.17	-1.14
5	120	400	300	2.14	2.10	3.38	1.78	1.77	1.29	2.08	2.02	6.23
6	120	500	200	2.22	2.15	6.30	1.83	1.82	0.74	2.16	2.15	0.79
7	150	300	300	2.52	2.54	-1.89	1.92	1.91	0.63	2.32	2.34	-2.15
8	150	400	200	2.56	2.59	-3.68	1.95	1.97	-1.92	2.46	2.48	-1.58
9	150	500	250	2.32	2.35	-2.62	1.89	1.88	1.18	2.33	2.32	0.79

Table 7.
Predicted R_a values of regression models for $t = 8$ mm.

Exp. no.	Independent variables			R _{a1} (μm)			R _{a2} (μm)			R _{a3} (μm)		
	X ₁	X ₂	X ₃	Exp.	Pred.	Error %	Exp.	Pred.	Error %	Exp.	Pred.	Error %
1	90	300	200	2.39	2.38	1.17	2.26	2.25	0.42	2.18	2.18	−0.09
2	90	400	250	2.20	2.21	−0.50	2.12	2.11	0.60	2.09	2.07	1.20
3	90	500	300	2.00	2.03	−3.17	1.95	1.97	−1.98	1.99	1.97	2.49
4	120	300	250	2.42	2.41	0.83	2.29	2.28	0.30	2.22	2.22	0.69
5	120	400	300	2.25	2.24	1.17	2.16	2.14	2.03	2.05	2.11	−5.75
6	120	500	200	2.48	2.45	3.00	2.29	2.29	−0.39	2.15	2.17	−2.15
7	150	300	300	2.45	2.45	0.50	2.30	2.32	−1.36	2.27	2.26	1.46
8	150	400	200	2.60	2.66	−5.67	2.45	2.46	−1.34	2.32	2.31	0.43
9	150	500	250	2.51	2.48	2.67	2.34	2.32	1.74	2.22	2.21	1.72

Table 8.
Predicted R_a values of regression models for t = 12 mm.

approximately straight-line and falling along the fitted line denotes that the data is normally distributed and there is a good relation between measured and estimated response values [45]. In general, the residuals versus fits and observation graph for each material thickness display that the points are distributed randomly and near both sides of 0, with no distinguished pattern denoting a minimal deviation within residuals and estimated values. This graph plots the difference between the experimental data as predicted on the y-axis and the fitted or predicted values on the x-axis, to validate the assumption that the residuals have constant variance [46].

Figure 4 also exhibits the histogram graph for R_a, illustrating the distribution or frequency of the residuals for all observations. The data shows the frequency of R_a for 4, 8 and 12 mm material thicknesses to range from −0.02 to 0.03, −0.05 to 0.05 and −0.02 to 0.02, respectively. The histogram presents distribution of the surface roughness obtained from varying material thicknesses. **Figure 4** histogram of residuals denotes that the residuals are normally distributed. These results reveal a minimal interval of inequalities of the experimental data, indicating that the R_a models meet their assumptions and are well fitted for the accuracy of prediction [46]. The effects of process parameters were established by ANOVA, where surface roughness results are given in **Tables A1-A3** in the Appendix section.

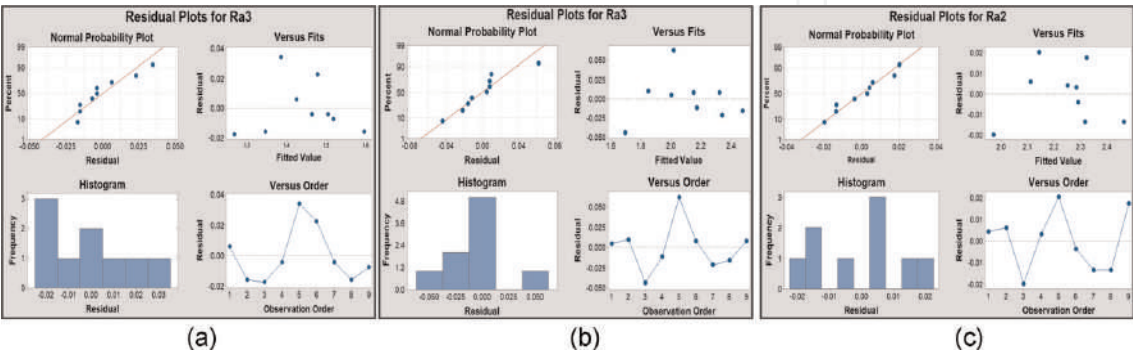


Figure 4.
Residual plots for surface roughness. (a) R_{a3} (μm) for t = 4 mm (b) R_{a3} (μm) for t = 8 mm (c) R_{a2} (μm) for t = 12 mm.

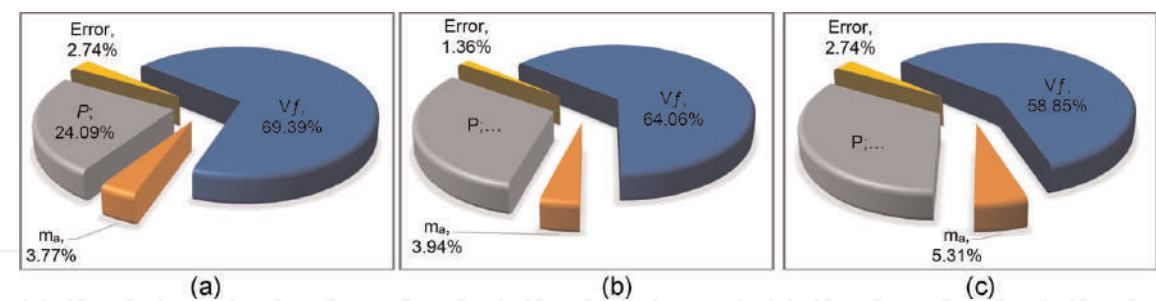


Figure 5. Percentage contribution of variables for surface roughness. (a) R_{a3} (μm) for $t = 4$ mm (b) R_{a3} (μm) for $t = 8$ mm (c) R_{a2} (μm) for $t = 12$ mm.

The impacts of the parameters for all profiles across the three levels of material thicknesses demonstrated a similar trend, denoting traverse speed and waterjet pressure to be significant factors for acquiring p-Values lower than 0.05, as detailed in **Tables A1-A3**. Accordingly, this work has established that abrasive mass flow rate is an insignificant input parameter for obtaining p-Values >0.05 , ranging from 0.002 to 0.067. **Figure 5** represents the percentage contribution of variables for R_a of the most fitted regression models for 4, 8 and 12 mm material thickness. Overall, traverse speed features as the most influencing parameter, followed by waterjet pressure and abrasive mass flow rate. It can be observed here that the influence of traverse speed decreases, ranging from 69.39 to 58.85%, as the material thickness increases. In AWJM, an increasing traverse speed reduces the number of abrasive particles, leading to higher occurrences of surface roughness [47]. **Figure 5** shows that as the material thickness increases, the percentage contribution of waterjet pressure and abrasive mass flow rate also increases, ranging from 24.09 to 33.1% and 3.77 to 5.31%, respectively. The increasing value of waterjet pressure denotes higher energy, reinforcing a larger amount of abrasive particles obtaining lower surface roughness [48]. Further, an increasing rate of abrasive mass flow breaks down abrasive particles into smaller sizes, resulting in more sharp edges that reduce surface roughness [15]. The percentage errors obtained were less than 20%, indicating acceptable reliability of the models, as described in Eq. (6).

3.2 Regression model and analysis for material removal rate

Table 9 displays multi-linear regression coefficients of models developed for material removal rate against input parameters i.e., traverse speed (X_1), abrasive mass flow rate (X_2) and waterjet pressure (X_3) for 4, 8 and 12 mm material thicknesses of AISI 304L. Regardless of material thickness and cutting profile category, the input parameter coefficients acquired a positive sign whilst the constant coefficients had a negative sign. The sign of the coefficient denotes the trend of relationship between variables and response [44]. As a result, an increasing rate of traverse speed, abrasive mass flow rate and waterjet pressure, generates a higher rate of material removal. Overall, the coefficient of determination R^2 ranged from 97.79 to 97.92%, with R^2_{adj} ranging from 96.46 to 96.67% and R^2_{pred} ranging from 92.53 to 94.35%, confirming that all generated regression models were significant. The models were established to be sufficient for accurate forecasting of material removal rate within the assigned levels of input parameters for AWJM of straight and arcs profiles. Furthermore, **Table 9** demonstrated that MRR1 (straight-line), MRR2 (inner

Term	<i>t</i> = 4 mm			<i>t</i> = 8 mm			<i>t</i> = 12 mm		
	MRR1	MRR2	MRR3	MRR1	MRR2	MRR3	MRR1	MRR2	MRR3
	Coef	Coef	Coef	Coef	Coef	Coef	Coef	Coef	Coef
	−84.2	−33	−22.8	−119	−45	−60.6	−158.8	−43.3	−73.5
β_1	1.752	1.562	1.440	2.941	2.658	2.708	3.867	4.476	3.416
β_2	0.1260	0.0833	0.0901	0.2723	0.1738	0.0333	0.3960	0.205	0.2437
β_3	0.5103	0.3430	0.4101	0.7770	0.775	0.950	0.917	0.511	1.080
Model Summary									
R^2	97.92%	97.56%	97.54%	98.86%	97.71%	94.73%	98.70%	96.37%	97.79%
R^2 (adj)	96.67%	96.09%	96.06%	98.18%	96.33%	91.56%	97.92%	94.20%	96.46%
R^2 (pred)	94.35%	90.74%	91.12%	95.73%	91.90%	82.30%	95.19%	89.41%	92.53%

Table 9.
Summary of linear regression coefficients for MRR.

arcs) and MRR3 (outer arcs) attained a uniform gap of at least 2% for R^2 , R^2 adj and R^2 pred values. This nominal disparity of the coefficient of determination indicates that AWJM performance for straight and curvature profiles are not significantly different from one another [36]. The results detailed in **Table 9** confirm that the highest values of R^2 , R^2 adj and R^2 pred for all material thicknesses was attained in MRR1 (straight-line profile) with values of 97.92, 96.67 and 94.35%; 98.86, 98.18 and 95.73%; 98.70, 97.92 and 95.19% respectively. This statistical measurement evaluates the relationship between the model and response variables, indicating that a value nearest to 100% denotes a more reliable model [49]. Therefore, MRR1 regression models are considered as the most fitted model for 4, 8 and 12 mm material thicknesses.

Tables 10-12 present the predicted MRR values using the generated regression models of 4, 8 and 12 mm thickness of AISI 304L for three varied contour profiles. The percentage error acquired for 4, 8 and 12 mm AISI 304L thicknesses ranged from −5.35 to 5.15%, −6.59 to 4.77% and − 5.05 to 6.62%, respectively. The errors determined for R_a between the predicted value and experimental results were less than 20%, indicating models to be well fitted for predicting MRR values.

Plots of all residuals of the best material removal rate (MRR1) for all material thicknesses are represented in **Figure 6**. Overall, the normal probability plots for all the material thicknesses illustrate that the adjacency of the points are linear indicating there is no deviation from the assumptions, because they are normally and independently distributed [46]. Residuals versus fits and observation for MRR1 of straight-line, inner and outer arc profiles confirm that there is no skewness or outlier pattern, revealing that individual deviated assumptions have no conflicts or contradictions. **Figure 6** also presents the histogram graph for MRR1, obtaining frequency ranging from −10 to 15 for 4 mm, −15 to 15 for 8 mm and − 18 to 20 for 12 mm material thicknesses. These results signify that the distribution or frequency of residuals for all observations fell in minimal interval or inequalities of the experimental data, justifying the adequacy of the suggested MRR1 models [46].

According to the results presented in **Tables A4-A6** in the Appendix section, detailing ANOVA for material removal rate, the effects of the input parameters for

Exp. no.	Independent variables			MRR 1 (mm ³ /min)			MRR 2 (mm ³ /min)			MRR 3 (mm ³ /min)		
	X ₁	X ₂	X ₃	Exp.	Pred.	Error %	Exp.	Pred.	Error %	Exp.	Pred.	Error %
1	90	300	200	216.2	213.3	1.36	212.1	201.2	5.15	217.7	215.9	0.83
2	90	400	250	248.6	251.4	-1.10	223.1	226.7	-1.60	242.4	245.5	-1.27
3	90	500	300	284.2	289.5	-1.86	250.6	252.1	-0.62	267.8	275.0	-2.68
4	120	300	250	280.6	291.3	-3.82	251.7	265.2	-5.35	283.0	279.6	1.19
5	120	400	300	342.5	329.4	3.82	293.7	290.7	1.03	313.7	309.2	1.44
6	120	500	200	298.8	291.0	2.61	263.5	264.7	-0.45	286.2	277.2	3.14
7	150	300	300	372.1	369.4	0.73	333.8	329.2	1.38	343.9	343.4	0.16
8	150	400	200	330.7	330.9	-0.07	299.6	303.2	-1.21	298.5	311.4	-4.32
9	150	500	250	361.5	369.1	-2.09	333.5	328.7	1.44	344.8	340.9	1.14

Table 10.
Predicted MRR values of regression model for t = 4 mm.

Exp. no.	Independent variables			MRR 1 (mm ³ /min)			MRR 2 (mm ³ /min)			MRR 3 (mm ³ /min)		
	X ₁	X ₂	X ₃	Exp.	Pred.	Error %	Exp.	Pred.	Error %	Exp.	Pred.	Error %
1	90	300	200	367.9	382.8	-4.05	405.0	401.4	0.88	399.0	383.0	4.00
2	90	400	250	456.9	448.9	1.75	450.8	457.6	-1.50	427.2	433.8	-1.56
3	90	500	300	511.2	515.0	-0.74	501.8	513.7	-2.37	493.1	484.7	1.71
4	120	300	250	526.9	509.9	3.23	526.4	519.9	1.23	488.1	511.7	-4.84
5	120	400	300	572.9	576.0	-0.54	583.5	576.1	1.27	579.8	562.6	2.97
6	120	500	200	532.9	525.5	1.39	532.2	515.9	3.06	441.8	470.9	-6.59
7	150	300	300	633.7	637.0	-0.52	639.7	638.4	0.19	629.1	640.5	-1.81
8	150	400	200	583.9	586.5	-0.45	555.1	578.3	-4.17	576.3	548.8	4.77
9	150	500	250	647.8	652.6	-0.74	641.3	634.5	1.07	601.3	599.6	0.28

Table 11.
Predicted MRR values of regression model for t = 8 mm.

straight and arc profiles at 4, 8 and 12 mm AISI 304L thicknesses display comparable results. Further, the results reveal that traverse speed and waterjet pressure are statistically and physically significant factors for obtaining p -Values<0.05. Hence, the abrasive mass flow rate features as a low impacting input parameter for obtaining p -Values greater than the acceptable value of 0.05, ranging from 0.002 to 0.751.

The percentage contribution of variables for the most fitted regression models MRR for 4, 8 and 12 mm material thicknesses are illustrated in **Figure 6**. In general, traverse speed is indicated as the most impacting variable, followed by waterjet pressure and abrasive mass flow rate, with a percent contribution ranging from 71.14–78.94%, 12.11–24.09% and 2.65–9.03% respectively for all profiles and material thicknesses. It is apparent here that the percentage contribution of traverse speed increases

Exp. no.	Independent variables			MRR 1 (mm ³ /min)			MRR 2 (mm ³ /min)			MRR 3 (mm ³ /min)		
	X ₁	X ₂	X ₃	Exp.	Pred.	Error %	Exp.	Pred.	Error %	Exp.	Pred.	Error %
1	90	300	200	472.0	491.5	−4.13	506.3	523.4	−3.37	528.9	523.1	1.10
2	90	400	250	586.2	576.9	1.58	542.1	569.5	−5.05	588.7	601.5	−2.17
3	90	500	300	655.9	662.4	−0.99	625.7	615.6	1.62	665.4	679.9	−2.18
4	120	300	250	676.0	653.4	3.35	731.7	683.2	6.62	687.5	679.6	1.15
5	120	400	300	735.0	738.8	−0.51	735.8	729.3	0.88	772.3	758.0	1.85
6	120	500	200	701.2	686.7	2.07	712.3	698.7	1.90	695.1	674.4	2.98
7	150	300	300	813.0	815.2	−0.27	822.4	843.1	−2.51	835.4	836.1	−0.09
8	150	400	200	755.6	763.1	−1.00	811.9	812.5	−0.07	725.0	752.5	−3.79
9	150	500	250	841.6	848.6	−0.83	845.6	858.6	−1.54	837.6	830.9	0.80

Table 12.
Predicted MRR values of regression model for t = 12 mm.

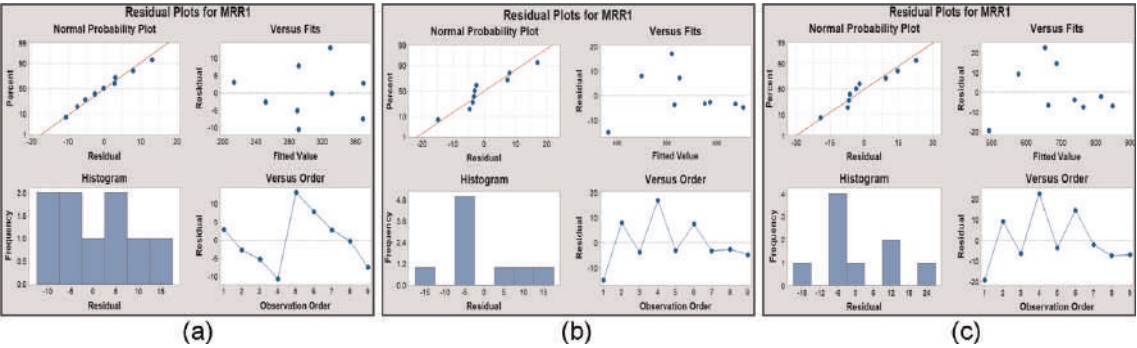


Figure 6.
Residual plots for material removal rate. (a) MRR 1 (mm³/min) for t = 4 mm (b) MRR 1 (mm³/min) for t = 8 mm (c) MRR (mm³/min) for t = 12 mm.

in range from 71.4 to 77.55% as the material thickness increases. An increasing traverse speed reinforces the contact time of the waterjet with the abrasive on the material, producing a higher volume rate of material to the machine [9]. Contrastingly, the percentage contribution of waterjet pressure and abrasive mass flow rate decreased as the material thickness and traverse speed increased, ranging from 22.42–12.11% and 4.35–9.03%, respectively. The increasing traverse speed and depth or thickness of the material to cut, results in a more prolonged machining process, which gradually leads to subsiding kinetic energy and loss of large of abrasive particles, resulting in reduced effectiveness of abrasive mass flow rate and waterjet pressure during the erosion process (**Figure 7**) [9, 47].

3.3 Regression model and analysis for kerf taper angle

The summary of the multi-linear regression coefficients for kerf taper angle of straight-line, inner and outer arc profiles using 4, 8 and 12 mm material thicknesses are detailed in **Table 13**. The results provide a similar trend, showing the constant sign

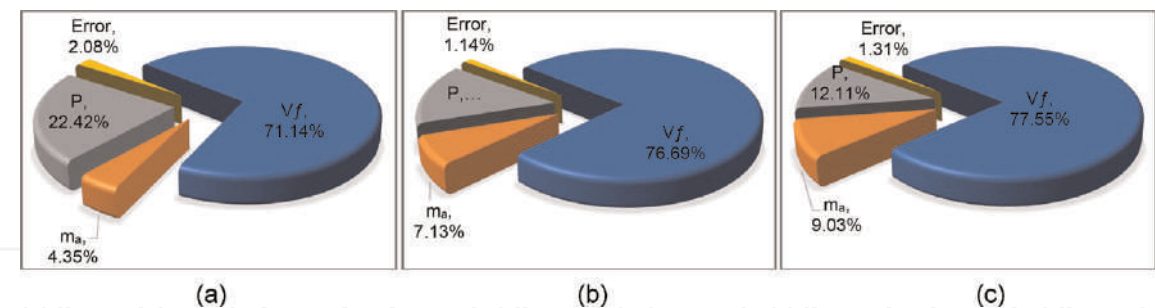


Figure 7. Percentage contribution of variables for material removal rate. (a) MRR 1 (mm^3/min) for $t = 4 \text{ mm}$ (b) MRR 1 (mm^3/min) for $t = 8 \text{ mm}$ (c) MRR (mm^3/min) for $t = 12 \text{ mm}$.

as positive, with variables X_1 , X_2 and X_3 as negative for all profiles and thicknesses. If the coefficient sign is negative, as the variable increases, the response decreases, whereas if the coefficient is positive, the relationship between variables and responses is directly proportional [44]. Therefore, an increasing rate of traverse speed (X_1) results in an increasing angle of the kerf taper. Thus, an increasing rate of abrasive mass flow and waterjet pressure reduces the value of kerf taper angle. The values of R^2 , R^2_{adj} and R^2_{pred} for 4, 8 and 12 mm ranged from 94.74–99.37%, 91.59–98.99% and 80.11–97.66%, respectively. This confirms that regression models are reliable in representing correlation between variables and responses and can be used in the optimisation of process parameters.

The coefficient of determination (R^2 , R^2_{adj} and R^2_{pred}) obtained from straight-line, inner and outer arc profiles for all material thicknesses had a similar and consistent gap of at least 2%. The AWJM provides comparable behaviour in processing both straight and curvature profiles [36]. The highest values of R^2 , R^2_{adj} and R^2_{pred} for 4 and 8 mm material thicknesses were attained in KTA1 with values of 97.56, 96.09 and 90.57%; 98.02, 96.82 and 92.01%; 99.37, 98.99 and 97.66%, respectively. These are the most fitted model, to be utilised in the optimisation of the process parameters of this study.

The predicted KTA values using the regression models applied for straight-line, inner and outer arc profiles of the three levels of material thicknesses are detailed in **Tables 14-16**. The percentage error obtained for 4, 8 and 12 mm AISI 304L thicknesses ranged between -2.55 to 1.72% , -2.67 to 3.74% and -3.14 to 2.43% , respectively. The errors calculated for KTA between the predicted value and experimental results were less than the acceptable maximum limit of 20%, indicating the reliability of the models in predicting KTA values.

Figure 8 illustrates the residual plot for KTA including normal probability plot, residual versus fits, histogram for residuals and residuals versus experimental values. The results showed that the most fitted regression model is achieved from KTA1 for all material thicknesses. Correspondingly, the normal probability plots for all material thicknesses present a near fit to a line in a normal probability graph. The points constructing an approximate straight-line and plotted along the fitted line signifies that the data is normally distributed and there is a good relation between experimental data and predicted values [45]. Predominantly, the residuals versus fits and observation graph for each material thickness exhibit that the points are plotted randomly and near both sides of 0 with no identified pattern denoting a minimal deviation within residuals and estimated values. **Figure 8** also presents the histogram graph for KTA

Term	<i>t</i> = 4 mm			<i>t</i> = 8 mm			<i>t</i> = 12 mm		
	KTA1	KTA2	KTA3	KTA1	KTA2	KTA3	KTA1	KTA2	KTA3
	Coef	Coef	Coef	Coef	Coef	Coef	Coef	Coef	Coef
	0.9674	1.0469	1.064	1.386	1.483	1.544	1.5981	1.971	1.998
β_1	0.002414	0.002155	0.001501	0.006143	0.003594	0.004333	0.006568	0.004556	0.004736
β_2	- 0.000235	- 0.000220	- 0.000136	−0.00052	−0.000525	−0.00035	- 0.000107	- 0.000400	- 0.000436
β_3	- 0.000932	- 0.000952	- 0.000668	−0.002039	−0.001346	- 0.001867	- 0.002319	- 0.002320	- 0.002286
Model Summary									
R ²	97.56%	97.26%	94.74%	98.02%	94.76%	96.79%	99.37%	96.30%	96.95%
R ² (adj)	96.09%	95.61%	91.59%	96.82%	91.61%	94.87%	98.99%	94.08%	95.12%
R ² (pred)	90.57%	88.61%	84.48%	92.01%	80.11%	88.29%	97.66%	86.50%	88.70%

Table 13.
Summary of linear regression coefficients for KTA.

Exp. no.	Independent variables			KTA1 (°)			KTA2 (°)			KTA3 (°)		
	X ₁	X ₂	X ₃	Exp.	Pred.	Error %	Exp.	Pred.	Error %	Exp.	Pred.	Error %
1	90	300	200	0.93	0.93	0.23	0.99	0.98	0.41	1.02	1.02	−0.19
2	90	400	250	0.86	0.86	0.26	0.92	0.92	0.84	0.98	0.98	0.15
3	90	500	300	0.77	0.79	−2.30	0.83	0.85	−2.16	0.94	0.93	0.53
4	120	300	250	0.95	0.95	−0.60	1.00	1.00	0.16	1.04	1.04	0.78
5	120	400	300	0.90	0.88	1.74	0.94	0.93	1.33	0.96	0.99	−2.55
6	120	500	200	0.97	0.95	1.72	1.00	1.01	−0.20	1.05	1.04	0.70
7	150	300	300	0.98	0.98	0.34	1.01	1.02	−0.80	1.06	1.05	1.13
8	150	400	200	1.03	1.05	−1.70	1.08	1.09	−1.44	1.09	1.10	−1.21
9	150	500	250	0.98	0.98	0.09	1.04	1.02	1.68	1.06	1.05	0.54

Table 14.
Predicted KTA values of regression model for t = 4 mm.

Exp. no.	Independent variables			KTA1 (°)			KTA2 (°)			KTA3 (°)		
	X ₁	X ₂	X ₃	Exp.	Pred.	Error %	Exp.	Pred.	Error %	Exp.	Pred.	Error %
1	90	300	200	1.38	1.38	0.04	1.40	1.38	1.42	1.43	1.46	−1.83
2	90	400	250	1.22	1.22	−0.12	1.27	1.26	0.76	1.34	1.33	0.91
3	90	500	300	1.04	1.07	−2.65	1.13	1.14	−0.94	1.21	1.20	0.87
4	120	300	250	1.48	1.46	1.50	1.43	1.42	0.43	1.54	1.49	3.07
5	120	400	300	1.35	1.30	3.42	1.30	1.30	−0.07	1.35	1.36	−1.07
6	120	500	200	1.44	1.46	−0.81	1.34	1.38	−3.20	1.49	1.52	−1.75
7	150	300	300	1.50	1.54	−2.67	1.44	1.46	−1.67	1.50	1.53	−1.96
8	150	400	200	1.68	1.69	−0.61	1.53	1.54	−0.81	1.70	1.68	1.11
9	150	500	250	1.56	1.54	1.41	1.48	1.42	3.74	1.56	1.55	0.46

Table 15.
Predicted KTA values of regression model for t = 8 mm.

illustrating the distribution or frequency of the residuals for all observations. The results show that the frequency of KTA for 4, 8 and 12 mm material thicknesses range from −0.002 to 0.015, −0.05 to 0.05 for 8 mm and − 0.02 to 0.03, respectively. These graphs reveal a minimal interval or inequalities of the experimental data indicating that the KTA regression models are highly fitted to concrete prediction [46].

Tables A7-A9 in the Appendix section detail the results of ANOVA, where it can be observed that the impacts of parameters for all profiles and three levels of material thicknesses demonstrate a similar trend, denoting traverse speed and waterjet pressure to be significant factors for acquiring *p*-Values lower than 0.05. Thus, the abrasive mass flow rate was found insignificant for achieving *p*-Values >0.05, ranging from 0.002 to 0.245 for all profiles and material thicknesses.

Exp. no.	Independent variables			KTA1 (°)			KTA2 (°)			KTA3 (°)		
	X ₁	X ₂	X ₃	Exp.	Pred.	Error %	Exp.	Pred.	Error %	Exp.	Pred.	Error %
1	90	300	200	1.70	1.69	0.39	1.80	1.80	0.18	1.85	1.84	0.49
2	90	400	250	1.57	1.57	0.07	1.63	1.64	−0.48	1.67	1.68	−0.26
3	90	500	300	1.43	1.44	−0.70	1.45	1.49	−2.20	1.49	1.52	−2.08
4	120	300	250	1.79	1.77	0.87	1.83	1.82	0.92	1.88	1.86	0.88
5	120	400	300	1.65	1.65	0.14	1.67	1.66	0.60	1.71	1.71	0.43
6	120	500	200	1.86	1.87	−0.72	1.90	1.85	2.43	1.92	1.89	1.51
7	150	300	300	1.84	1.86	−0.85	1.85	1.84	0.52	1.89	1.89	0.13
8	150	400	200	2.06	2.08	−0.81	1.97	2.03	−3.14	2.02	2.08	−2.93
9	150	500	250	1.98	1.95	1.51	1.89	1.87	0.82	1.95	1.92	1.55

Table 16.
Predicted KTA values of regression model for $t = 12\text{ mm}$.

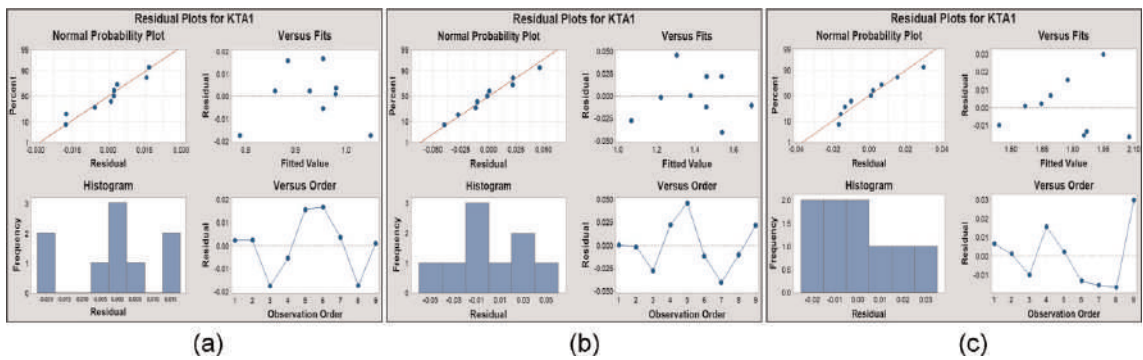


Figure 8.
Residual plots for kerf taper angle. (a) KTA1 (°) for $t = 4\text{ mm}$ (b) KTA1 (°) for $t = 8\text{ mm}$ (c) KTA1 (°) for $t = 12\text{ mm}$.

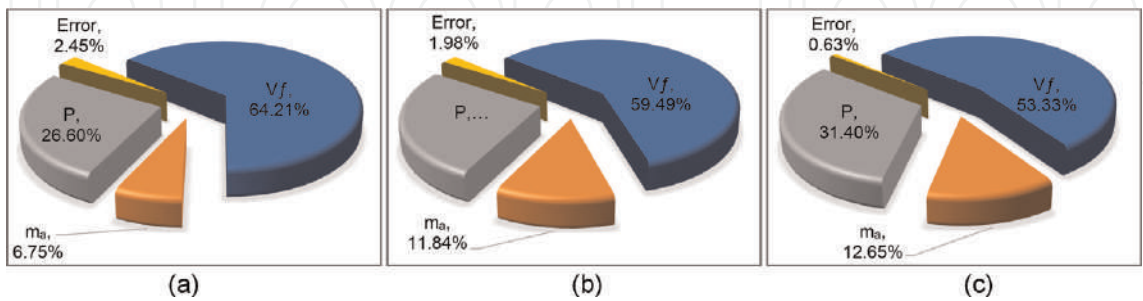


Figure 9.
Percentage contribution of variables for kerf taper angle. (a) $t = 4\text{ mm}$ (b) $t = 8\text{ mm}$ (c) $t = 12\text{ mm}$.

Figure 9 exhibits the percentage contribution of variables for KTA for the most fitted regression models for 4, 8 and 12 mm material thickness. Traverse speed was the most influencing parameter, followed by waterjet pressure and abrasive mass flow rate, in agreement with previous studies [14, 37]. The obtained

results have shown that the influence of traverse speed decreases in range from 64.21 to 53.33% as the material thickness increases. An increasing value traverse speed results in the loss of a large number of abrasive particles, continuously dropping as the material thickness also increases, leading to a higher angle of kerf taper [50]. **Figure 9** shows increases of material thickness, the percentage contribution of waterjet pressure and abrasive mass flow rate, ranging from 26.60 to 33.40% and 6.75 to 12.65%, respectively. This increasing value of waterjet pressure resulted in higher energy, generating a larger amount of abrasive particles that result in a lower kerf taper [51]. Moreover, a rising rate of abrasive mass flow breaks down abrasive particles into a smaller scale, generating more sharp points that results in reduction of kerf taper angle [51].

4. Response surface methodology multi-objective optimisation

In this research, multi-objective optimisation was performed using RSM to determine the optimum process parameters of abrasive waterjet contour cutting of AISI 304L with varied thicknesses using MINITAB 19 software. The following optimisation objectives were stated as follows:

$$f_1 = \text{Min} (R_a) \quad (8)$$

$$f_2 = \text{Min} (KTA) \quad (9)$$

$$f_3 = \text{Max} (MRR) \quad (10)$$

RSM optimisation was performed using the models with the highest determination of coefficients, i.e., R^2 , R^2_{adj} and R^2_{pred} . Accordingly, the regression models utilised to minimise surface roughness were R_{a3} for 4 and 8 mm and R_{a2} for 12 mm. MRR_1 and KTA_1 models were used for all material thicknesses.

The Regression models utilised in multi-objective optimisation for varied thicknesses of AISI 304L were expressed by Eqs. (8)-(16).

$$Ra_{4\text{mm}} = 1.4256 + 0.003222 X_1 - 0.000217 X_2 - 0.001133 X_3 \quad (11)$$

$$KTA_{4\text{mm}} = 0.9674 + 0.002414 X_1 - 0.000235 X_2 - 0.000932 X_3 \quad (12)$$

$$MRR_{4\text{mm}} = -84.2 + 1.752 X_1 + 0.126 X_2 + 0.5103 X_3 \quad (13)$$

$$Ra_{8\text{mm}} = 1.76 + 0.008869 X_1 - 0.000577 X_2 - 0.001920 X_3 \quad (14)$$

$$KTA_{8\text{mm}} = 1.386 + 0.006143 X_1 - 0.000520 X_2 - 0.002039 X_3 \quad (15)$$

$$MRR_{8\text{mm}} = -119 + 2.941X_1 + 0.2723 X_2 + 0.777X_3 \quad (16)$$

$$Ra_{4\text{mm}} = 2.3854 + 0.004276 X_1 - 0.000446 X_2 - 0.001924 X_3 \quad (17)$$

$$KTA_{4\text{mm}} = 1.5981 + 0.006568 X_1 - 0.000107 X_2 - 0.002319 X_3 \quad (18)$$

$$MRR_{8\text{mm}} = -158.8 + 3.867X_1 + 0.396 X_2 + 0.917 X_3 \quad (19)$$

In simultaneous optimisation, goals and boundaries must be defined for each process parameter. Targets are based on the experimental data obtained, referring to the set highest value of responses for maximising MRR and lowest value of responses for minimising R_a and KTA. In this optimisation, process parameters and defined objectives were assigned to be equally significant. Therefore, the equal weights

(wt. = 1) were assigned in order to achieve an equal importance to the process parameters and objectives. The constraints referring to range and limits of the process parameters are detailed below.

Constraints:

$$90 \leq V_f \leq 150 \text{ mm/min}$$

$$300 \leq m_a \leq 500 \text{ g/min}$$

$$200 \leq P \leq 300 \text{ g/min}$$

Limits:

$$KTA_{4\text{mm}} \leq 1.03^\circ, KTA_{8\text{mm}} \leq 1.68^\circ, KTA_{12\text{mm}} \leq 2.06^\circ$$

$$Ra_{4\text{mm}} \text{ mm}1.58 \mu\text{m}, Ra_{8\text{mm}} \text{ mm}2.45 \mu\text{m}, Ra_{12\text{mm}} \text{ mm}2.46 \mu\text{m}$$

$$MRR_{4\text{mm}} \geq 216.20 \text{ mm}^3/\text{min}, MRR_{8\text{mm}} \geq 367.90 \text{ mm}^3/\text{min},$$

$$MRR_{12\text{mm}} \geq 472.00 \text{ mm}^3/\text{min}$$

Table 17 shows the solutions for multi-objective optimisation performed for 4, 8 and 12 mm thickness of AISI 304L. The solution that provides the value of composite desirability nearest to 1 can be considered as the best solution [40]. **Table 17** reveals that solution 1 is the best for 4, 8 and 12 mm material thicknesses, achieving composite desirability values of 0.748448, 0.780587 and 0.786800, respectively. There are three solutions generated from MINITAB application, providing the settings of input variables, achieved values of responses and composite desirability. Solution 1 provides the optimum settings of input parameters i.e., V_f for 4, 8 and 12 mm material thicknesses, at the speeds of 95, 90 and 91 mm/min, respectively. The obtained optimum setting for m_a and P were found to be the same value for all material thicknesses, at 500 g/min and 200 MPa, respectively. **Table 17** presents the minimum achieved values of KTA and R_a and maximum MRR for 4, 8 and 12 mm material thicknesses, featuring at 0.799° , $1.283 \mu\text{m}$ and $297.98 \text{ mm}^3/\text{min}$; 1.068° , $1.694 \mu\text{m}$ and $514.97 \text{ mm}^3/\text{min}$ and 1.448° , $1.975 \mu\text{m}$ and $667.07 \text{ mm}^3/\text{min}$, respectively.

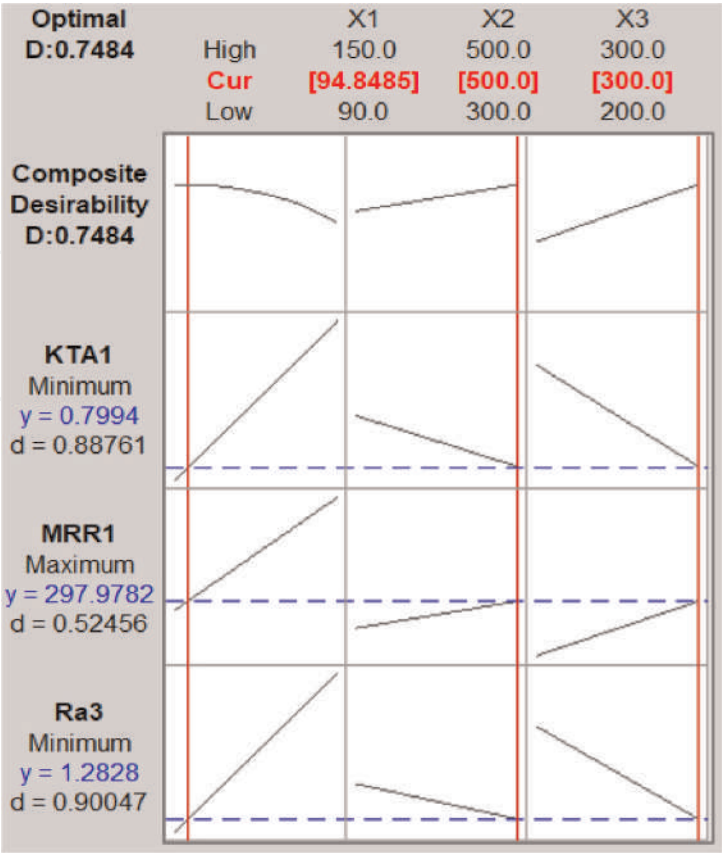
An optimisation plot presenting how the variables affected the predicted responses is shown in **Figure 10**, detailing the composite desirability for multi-objective (D) and single-objective optimisation (d). Current variable settings for the input parameters are presented in the figure, alongside with lower and upper limits. **Figure 10** shows a three-sectioned line graph representing the correlation of KTA, R_a and MRR against traverse speed (X_1), abrasive mass flow rate (X_2) and waterjet pressure (X_3).

From the figure, it can be observed that abrasive waterjet contour cutting responses demonstrate a comparable behaviour against input parameters for all material thicknesses. The highest rate of material removal and lowest value of surface roughness and Kerf taper angle were achieved by employing a rate of 150 mm/min speed, 500 g/min abrasive mass flow rate, and 300 MPa of waterjet pressure. Increasing water pressure, alongside high velocity abrasive mass flow rate, produces a greater collision of abrasive particles, generating higher rate of material removal and reducing surface roughness and kerf taper angle [52].

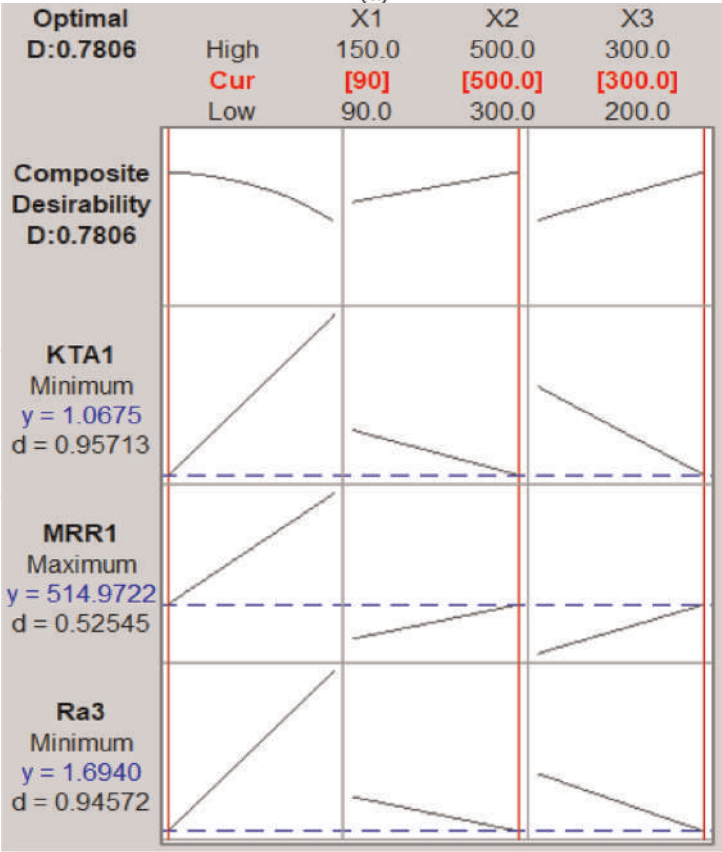
The surface roughness displayed an incrementing value that ranged from 4–13% as the rate of traverse speed increased from 90 to 150 mm/min. As the speed increases per unit of area over time, the kinetic energy containing abrasives gradually decreases, resulting in greater evidences of rough surfaces [52]. Consequently, RSM optimisation

Parameters	4 mm			8 mm			12 mm		
	Solutions								
	1	2	3	1	2	3	1	2	3
$X_1 = V_f$ (mm/min)	95	97	97	90	90	116	91	90	90
$X_2 = m_a$ (g/min)	500	500	500	500	500	301.737	500	500	500
$X_3 = P$ (MPa)	300	300	300	300	300	300	300	300	300
KTA (°)	0.799	0.805	0.805	1.068	1.068	1.330	1.448	1.441	1.441
MRR (mm ³ /min)	297.98	302.17	302.17	514.97	514.97	537.49	667.07	662.78	662.78
R _a (µm)	1.283	1.291	1.291	1.694	1.694	2.039	1.975	1.970	1.970
Composite Desirability	0.748448	0.748075	0.748075	0.780587	0.780587	0.556566	0.786800	0.786677	0.786677

Table 17.
Solutions for RSM multi-objective optimisation.



(a)



(b)

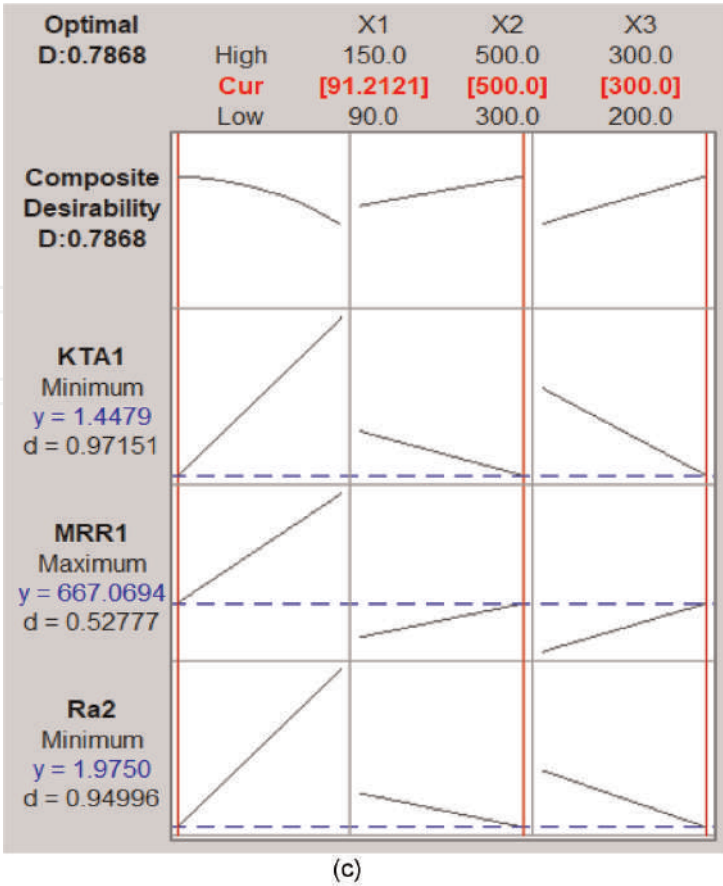


Figure 10. Response optimisation plot. (a) $t = 4\text{ mm}$ (b) $t = 8\text{ mm}$ (c) $t = 12\text{ mm}$.

has shown that a lower level of traverse speed can produce a better quality of cut surface. Additionally, surface roughness in this study shows an increasing value ranging 2–5%, as the waterjet pressure increases and the abrasive mass flow rate from 200 to 300 MPa and 300 to 500 g/min, respectively. In this study, it is confirmed that augmenting abrasive flow rate and waterjet pressure, up to a specific range, lowers the value of surface roughness. When higher values of traverse speed are employed, the material removal exhibits an increasing rate that ranges from 16–20%. In addition, increasing rate of material removal was achieved with a range of 5–9%, as the rate of abrasive mass flow and waterjet pressure increased from 200 to 300 MPa and 300 to 500 g/min, respectively. AWJM produces a high level of kinetic energy, driving a higher level of speed and waterjet pressure alongside with abrasive mass flow rate, which in turn generates higher cutting area per unit of time and generates a larger amount of eroded material [53]. Therefore, the rate of material removal is directly proportional to traverse speed, abrasive mass flow rate and waterjet pressure. **Figure 10** shows that kerf taper angle values increase as the rate of traverse speed increases from 90 to 150 mm/min. With continuous reduction in the number of abrasive particles, as the traverse speed increases, the cohesion on metal material decreases, generating a higher tapering angle [52]. The kerf taper angle in this study was reduced by 2–7%, as the abrasive mass flow and waterjet pressure were increased from 200 to 300 MPa and 300 to 500 g/min, respectively. A higher waterjet pressure alongside with abrasive mass flow rate reinforces the collision of abrasive particles on the target material, causing the reduction of kerf taper angle [51].

5. Conclusions

This study focuses on modelling and establishing optimum abrasive waterjet contour cutting parameters that lead to minimum surface roughness, kerf taper angle and maximum productivity (material removal rate). On the basis of the results achieved and discussed, the following conclusions are accomplished:

1. The experimental results indicate that abrasive waterjet contour cutting responses demonstrate similar behaviour against input parameters for straight-line and curvature profiles. The correlation coefficients of the predictive models of R^2 , R^2_{adj} and R^2_{pred} for surface roughness, kerf taper angle and material removal rate were found to be in the range of 88.66–99.08%, 82.3–98.86% and 82.3–98.86% respectively. Therefore, the developed multi-linear regression models are reliable and effective for predicting output responses, where the percentage errors are at minimum values ranging from –6.59 to 6.71%
2. The results of the ANOVA for R_a , MRR and KTA demonstrate that traverse speed is the most influencing factor, with percentage contributions ranging from 55.67 to 78.94%. Surface roughness and kerf taper angle decrease as waterjet pressure and abrasive mass flow rate increase, resulting in reductions ranging from 2–5% and 2–7%, respectively. Increasing values of traverse speed, waterjet pressure and abrasive mass flow rate lead to increased rates of material removal, ranging from 16–20% and 5–9%, respectively.
3. The multi-objective optimization was performed using RSM for optimising abrasive waterjet contour cutting process parameters applied for 4, 8 and 12 mm material thicknesses, achieving the highest composite desirability values of 0.748448, 0.780587 and 0.786800, respectively. The optimum settings of input parameters i.e., V_f for 4, 8 and 12 mm material thickness are 95, 90 and 91 mm/min, respectively. The obtained optimum settings for m_a and P were found to be the same value for all material thicknesses, at 500 g/min and 200 MPa, respectively. The minimum achieved values of KTA and R_a and maximum MRR for 4, 8 and 12 mm material thickness were 0.799^0 , $1.283\ \mu\text{m}$ and $297.98\ \text{mm}^3/\text{min}$; 1.068^0 , $1.694\ \mu\text{m}$ and $514.97\ \text{mm}^3/\text{min}$; and 1.448^0 , $1.975\ \mu\text{m}$ and $667.07\ \text{mm}^3/\text{min}$, respectively.

Abbreviations and nomenclature

ht	depth of cut (mm)
m_a	abrasive mass flow rate (g/min)
P	water pressure (MPa)
R_a	surface roughness (μm)
V_f	traverse speed (mm/min)
W	kerf width (mm)
W_t	kerf top width (mm)
W_b	kerf bottom width (mm)
t	thickness of the material (mm)
AISI	austenitic stainless steel

ANOVA analysis of variance
AWJM abrasive waterjet machining
KTA kerf taper angle (⁰)
MRR material removal rate (mm³/min)

A. Appendix

Source	R _a 1		R _a 2		R _a 3	
	Contribution %	<i>p</i> -Value	Contribution %	<i>p</i> -Value	Contribution %	<i>p</i> -Value
<i>X</i> ₁	59.90	0.001	69.43	0.000	69.39	0.000
<i>X</i> ₂	5.16	0.067	3.49	0.068	3.77	0.017
<i>X</i> ₃	30.19	0.002	23.86	0.002	24.09	0.001
Error	4.74		3.23		2.74	
Total	100.00		100		100	

Table A1.
ANOVA of R_a for t = 4 mm.

Source	R _a 1		R _a 2		R _a 3	
	Contribution %	<i>p</i> -Value	Contribution %	<i>p</i> -Value	Contribution %	<i>p</i> -Value
<i>X</i> ₁	72.21	0.000	71.07	0.000	64.06	0.000
<i>X</i> ₂	7.96	0.007	11.57	0.003	3.94	0.013
<i>X</i> ₃	17.84	0.001	15.52	0.001	30.64	0.001
Error	1.99		1.84		1.36	
Total	100.00		100.00		100.00	

Table A2.
ANOVA of R_a for t = 8 mm.

Source	R _a 1		R _a 2		R _a 3	
	Contribution %	<i>p</i> -Value	Contribution %	<i>p</i> -Value	Contribution %	<i>p</i> -Value
<i>X</i> ₁	57.23	0.000	58.85	0.000	57.21	0.001
<i>X</i> ₂	3.44	0.026	5.31	0.002	17.66	0.011
<i>X</i> ₃	34.59	0.000	33.1	0.000	19.47	0.009
Error	4.74		2.74		3.23	3.23
Total	100.00		100.00		100.00	

Table A3.
ANOVA of R_a for t = 12 mm.

Source	MRR 1		MRR 2		MRR 3	
	Contribution %	<i>p</i> -Value	Contribution %	<i>p</i> -Value	Contribution %	<i>p</i> -Value
X_1	71.14	0.000	70.98	0	75.503	0
X_2	4.35	0.023	2.65	0.067	3.345	0.048
X_3	22.42	0.002	23.93	0.001	18.688	0.002
Error	2.08		2.44		2.464	
Total	100.00		100.00		100.00	

Table A4.
 ANOVA of MRR for t = 4 mm.

Source	MRR 1		MRR 2		MRR 3	
	Contribution %	<i>p</i> -Value	Contribution %	<i>p</i> -Value	Contribution %	<i>p</i> -Value
X_1	76.69	0.000	76.12	0.000	70.51	0.000
X_2	7.13	0.002	3.62	0.038	0.12	0.751
X_3	15.05	0.000	17.98	0.002	24.09	0.005
Error	1.14		2.29		5.27	
Total	100.00		100.00		100.00	

Table A5.
 ANOVA of MRR for t = 8 mm.

Source	MRR 1		MRR 2		MRR 3	
	Contribution %	<i>p</i> -Value	Contribution %	<i>p</i> -Value	Contribution %	<i>p</i> -Value
X_1	77.55	0.000	78.94	0.000	73.29	0.000
X_2	9.03	0.002	4.13	0.04	4.15	0.028
X_3	12.11	0.001	13.3	0.001	20.35	0.001
Error	1.31		3.63		2.21	
Total	100.00		100.00		100.00	

Table A6.
 ANOVA of MRR for t = 12 mm.

Source	KTA 1		KTA 2		KTA 3	
	Contribution %	<i>p</i> -Value	Contribution %	<i>p</i> -Value	Contribution %	<i>p</i> -Value
X_1	64.21	0.000	58.7	0.000	56.74	0.000
X_2	6.75	0.014	6.77	0.017	5.27	0.075
X_3	26.6	0.001	31.78	0.001	32.74	0.001
Error	2.45		2.74		5.26	
Total	100.00		100.00		100.00	

Table A7.
 ANOVA of KTA for t = 4 mm.

Source	KTA 1		KTA 2		KTA 3	
	Contribution %	<i>p</i> -Value	Contribution %	<i>p</i> -Value	Contribution %	<i>p</i> -Value
X_1	59.49	0.001	67.49	0.000	60.95	0.000
X_2	11.84	0.015	5.63	0.013	4.42	0.047
X_3	26.69	0.002	21.65	0.001	31.42	0.001
Error	1.98		5.24		3.21	
Total	100.00		100.00		100.00	

Table A8.
ANOVA of KTA for t = 8 mm.

Source	KTA 1		KTA 2		KTA 3	
	Contribution %	<i>p</i> -Value	Contribution %	<i>p</i> -Value	Contribution %	<i>p</i> -Value
X_1	53.33	0.000	70.59	0.000	55.67	0.000
X_2	12.65	0.055	0.22	0.245	5.24	0.033
X_3	31.40	0.001	25.50	0.000	36.04	0.001
Error	0.63		3.70		3.05	
Total	100.00		100.00		100.00	


Table A9.
ANOVA of KTA for t = 12 mm.

Author details

Jennifer Milaor Llanto, Ana Vafadar and Majid Tolouei-Rad*
School of Engineering, Edith Cowan University, Joondalup, Australia

*Address all correspondence to: m.rad@ecu.edu.au

IntechOpen

© 2022 The Author(s). Licensee IntechOpen. This chapter is distributed under the terms of the Creative Commons Attribution License (<http://creativecommons.org/licenses/by/3.0>), which permits unrestricted use, distribution, and reproduction in any medium, provided the original work is properly cited. 

References

- [1] Radovanović M. Multi-objective optimization of process performances when cutting carbon steel with abrasive water jet. *Tribology in Industry*. 2016;**38**(4):1741-1759
- [2] Liu X et al. Waterjet machining and research developments: A review. *The International Journal of Advanced Manufacturing Technology*. 2019; **102**(5):1257-1335
- [3] Rajurkar K et al. Review of sustainability issues in non-traditional machining processes. *Procedia Manufacturing*. 2017;**7**:714-720
- [4] Natarajan Y et al. Abrasive water jet machining process: A state of art of review. *Journal of Manufacturing Processes*. 2020;**49**:271-322
- [5] Singh P et al. Developments of non-conventional drilling methods—a review. *The International Journal of Advanced Manufacturing Technology*. 2020;**106**(5):2133-2166
- [6] Sureban R, Kulkarni VN, Gaitonde V. Modern optimization techniques for advanced machining processes—a review. *Materials Today: Proceedings*. 2019;**18**:3034-3042
- [7] Rao RV, Rai DP, Balic J. Optimization of abrasive waterjet machining process using multi-objective jaya algorithm. *Materials Today-Proceedings*. 2018;**5**(2): 4930-4938
- [8] Nair A, Kumanan S. Multi-performance optimization of abrasive water jet machining of Inconel 617 using WPCA. *Materials and Manufacturing Processes*. 2017;**32**(6):693-699
- [9] Chakraborty S, Mitra A. Parametric optimization of abrasive water-jet machining processes using grey wolf optimizer. *Materials and Manufacturing Processes*. 2018;**33**(13):1471-1482
- [10] Trivedi P, Dhanawade A, Kumar S. An experimental investigation on cutting performance of abrasive water jet machining of austenite steel (AISI 316L). *Advances in Materials and Processing Technologies*. 2015;**1**(3–4):263-274
- [11] Gnanavelbabu A et al. Experimental investigations on multiple responses in abrasive waterjet machining of Ti-6Al-4V alloy. *Materials Today: Proceedings*. 2018;**5**(5):13413-13421
- [12] Jeykrishnan J et al. Optimization of process parameters in abrasive water jet machining/cutting (AWJM) of nickel alloy using traditional analysis to minimize kerf taper angle. *Materials Today: Proceedings*. 2019;**16**:392-397
- [13] Singh D, Shukla RS. Investigation of kerf characteristics in abrasive water jet machining of inconel 600 using response surface methodology. *Defence Science Journal*. 2020;**70**(3):313-322
- [14] Madankar A et al. Estimation and control of surface quality and traverse speed in abrasive water jet machining of AISI 1030 steel using different work-piece thicknesses by RSM. *Australian Journal of Mechanical Engineering*. 2021; **1**:1-8
- [15] Llanto JM et al. Recent progress trend on abrasive waterjet cutting of metallic materials: A review. *Applied Sciences*. 2021;**11**(8):3344
- [16] Pérez L, Carmelo J. On the application of a design of experiments along with an anfis and a desirability function to model response variables. *Symmetry*. 2021;**13**(5):897

- [17] Luis Pérez C. A proposal of an adaptive neuro-fuzzy inference system for modeling experimental data in manufacturing engineering. *Mathematics*. 2020;**8**(9):1390
- [18] Jiang W et al. Effects of nanostructural hierarchy on the hardness and thermal stability of an austenitic stainless steel. *Journal of Materials Research and Technology*. 2021;**12**: 376-384
- [19] Ramana MV et al. Optimization and influence of process parameters of dissimilar SS304L–SS430 joints produced by Robotic TIG welding. *Materials Today: Proceedings*. 2020;**23**: 479-482
- [20] Doreswamy D et al. Machining of d2 heat treated steel using abrasive water jet: The effect of standoff distance and feed rate on kerf width and surface roughness. *International Journal of Research in Engineering and Technology*. 2014;**3**(8):417-421
- [21] Shibin R et al. Investigation on the abrasive water jet machinability of AA2014 using SiC as abrasive. *Materials Today: Proceedings*. 2020;**21**:519-522
- [22] Radovanovic M, Herghelegiu E. Perpendicularity deviation and surface roughness in abrasive water jet cutting of carbon steel. *Revista de Tehnologii Neconventionale*. 2016;**20**(2):39
- [23] Maneiah D et al. Optimization of machining parameters for surface roughness during abrasive water jet machining of aluminium/magnesium hybrid metal matrix composites. *Materials Today: Proceedings*. 2020;**27**: 1293-1298
- [24] Rajamanickam S et al. Comparative analysis of MRR on abrasive water jet machining parameters over aerospace alloys: Inconel 825 & Ti-6Al-4V. *International Journal of Pure and Applied Mathematics*. 2018;**118**:727-733
- [25] Kaladhar M, Subbaiah KV, Rao CS. Machining of austenitic stainless steels—a review. *International Journal of Machining and Machinability of Materials*. 2012;**12**(1):178-192
- [26] Hlaváč LM et al. Investigation of the taper of kerfs cut in steels by AWJ. *The International Journal of Advanced Manufacturing Technology*. 2015; **77**(9–12):1811-1818
- [27] Pawar PJ, Vidhate US, Khalkar MY. Improving the quality characteristics of abrasive water jet machining of marble material using multi-objective artificial bee colony algorithm. *Journal of Computational Design and Engineering*. 2018;**5**(3):319-328
- [28] Hlaváč LM et al. Shape distortion reduction method for abrasive water jet (AWJ) cutting. *Precision Engineering*. 2018;**53**:194-202
- [29] Aamir M et al. Optimization and modeling of process parameters in multi-hole simultaneous drilling using taguchi method and fuzzy logic approach. *Materials*. 2020;**13**(3):680
- [30] Msomi V, Mabuwa S. Analysis of material positioning towards microstructure of the friction stir processed AA1050/AA6082 dissimilar joint. *Advances in Industrial and Manufacturing Engineering*. 2020;**1**: 100002
- [31] Lin C. Use of the Taguchi method and grey relational analysis to optimize turning operations with multiple performance characteristics. *Materials and Manufacturing Processes*. 2004; **19**(2):209-220

- [32] Aamir M et al. Feasibility of tool configuration and the effect of tool material, and tool geometry in multi-hole simultaneous drilling of Al2024. *The International Journal of Advanced Manufacturing Technology*. 2020;**111**(3): 861-879
- [33] Nagaraj Y et al. Prediction of material removal rate and surface roughness in hot air assisted hybrid machining on soda-lime-silica glass using regression analysis and artificial neural network. *Silicon*. 2020;**13**(11):1-13
- [34] Aydin G, Karakurt I, Hamzacebi C. Artificial neural network and regression models for performance prediction of abrasive waterjet in rock cutting. *The International Journal of Advanced Manufacturing Technology*. 2014;**75**(9–12):1321-1330
- [35] Cetin MH et al. Evaluation of vegetable based cutting fluids with extreme pressure and cutting parameters in turning of AISI 304L by Taguchi method. *Journal of Cleaner Production*. 2011;**19**(17–18):2049-2056
- [36] Llanto JM et al. Analysis and optimization of process parameters in abrasive waterjet contour cutting of AISI 304L. *Metals*. 2021;**11**(9):1362
- [37] Llanto JM et al. Impacts of traverse speed and material thickness on abrasive waterjet contour cutting of austenitic stainless steel AISI 304L. *Applied Sciences*. 2021;**11**(11):4925
- [38] Aamir M et al. Machinability of Al2024, Al6061, and Al5083 alloys using multi-hole simultaneous drilling approach. *Journal of Materials Research and Technology*. 2020;**9**(5):10991-11002
- [39] Koli Y, Yuvaraj N, Aravindan S. Multi-response mathematical model for optimization of process parameters in CMT welding of dissimilar thickness AA6061-T6 and AA6082-T6 alloys using RSM-GRA coupled with PCA. *Advances in Industrial and Manufacturing Engineering*. 2021;**2**:100050
- [40] Kumar KR, Sreebalaji V, Pridhar T. Characterization and optimization of abrasive water jet machining parameters of aluminium/tungsten carbide composites. *Measurement*. 2018;**117**: 57-66
- [41] Chabbi A et al. Predictive modeling and multi-response optimization of technological parameters in turning of polyoxymethylene polymer (POM C) using RSM and desirability function. *Measurement*. 2017;**95**:99-115
- [42] Chate GR et al. Study of the effect of nano-silica particles on resin-bonded moulding sand properties and quality of casting. *Silicon*. 2018;**10**(5):1921-1936
- [43] Javed SA et al. A critical review: Shape optimization of welded plate heat exchangers based on grey correlation theory. *Applied Thermal Engineering*. 2018;**144**:593-599
- [44] Ratner B. The correlation coefficient: Its values range between+ 1/ – 1, or do they? *Journal of Targeting, Measurement and Analysis for Marketing*. 2009;**17**(2):139-142
- [45] Deshpande Y, Andhare A, Sahu NK. Estimation of surface roughness using cutting parameters, force, sound, and vibration in turning of Inconel 718. *Journal of the Brazilian Society of Mechanical Sciences and Engineering*. 2017;**39**(12):5087-5096
- [46] Galpin JS, Hawkins DM. The use of recursive residuals in checking model fit in linear regression. *The American Statistician*. 1984;**38**(2):94-105

[47] Sasikumar K et al. A study on kerf characteristics of hybrid aluminium 7075 metal matrix composites machined using abrasive water jet machining technology. *Proceedings of the Institution of Mechanical Engineers, Part B: Journal of Engineering Manufacture*. 2018;**232**(4): 690-704

[48] Kechagias J, Petropoulos G, Vaxevanidis N. Application of Taguchi design for quality characterization of abrasive water jet machining of TRIP sheet steels. *The International Journal of Advanced Manufacturing Technology*. 2012;**62**(5–8):635-643

[49] Andrzej P. Experimental research into alternative abrasive material for the abrasive water-jet cutting of titanium. *The International Journal of Advanced Manufacturing Technology*. 2018;**97** (1–4):1529-1540

[50] Uthayakumar M et al. Machinability of nickel-based superalloy by abrasive water jet machining. *Materials and Manufacturing Processes*. 2016;**31**(13): 1733-1739

[51] Babu MN, Muthukrishnan N. Exploration on Kerf-angle and surface roughness in abrasive waterjet machining using response surface method. *Journal of The Institution of Engineers (India): Series C*. 2018;**99**(6): 645-656

[52] Ishfaq K et al. Abrasive waterjet cutting of clad material: Kerf taper and MRR analysis. *Materials and Manufacturing Processes*. 2019;**34**(5): 544-553

[53] Kmec J et al. The predictive model of surface texture generated by abrasive water jet for austenitic steels. *Applied Sciences*. 2020;**10**(9):3159

We are IntechOpen, the world's leading publisher of Open Access books Built by scientists, for scientists

6,300

Open access books available

171,000

International authors and editors

190M

Downloads

Our authors are among the

154

Countries delivered to

TOP 1%

most cited scientists

12.2%

Contributors from top 500 universities



WEB OF SCIENCE™

Selection of our books indexed in the Book Citation Index
in Web of Science™ Core Collection (BKCI)

Interested in publishing with us?
Contact book.department@intechopen.com

Numbers displayed above are based on latest data collected.
For more information visit www.intechopen.com



Multi-objective Optimisation in Abrasive Waterjet Contour Cutting of AISI 304L

Jennifer Milaor Llanto, Ana Vafadar and Majid Tolouei-Rad

Abstract

The optimum waterjet machining parameters were found for maximising material removal rate and minimising surface roughness and kerf taper angle where three levels of traverse speed, abrasive flow rate, and waterjet pressure are used. The multi-linear regression equations were obtained to investigate the relationships between variables and responses, and the statistical significance of contour cutting parameters was analysed using the analysis of variance (ANOVA). Further, the response surface methodology (desirability function approach) was utilised for multi-objective optimisation. The optimum traverse speeds were 95 mm/min for 4 mm thickness and 90 mm/min for both 8 and 12 mm thicknesses. For all material thicknesses, the abrasive mass flow rate and waterjet pressure were 500 g/min and 200 MPa, respectively. The minimum values of surface roughness, kerf taper angle, and maximum material removal rate for 4-, 8- and 12-mm material thicknesses were respectively 0.799°, 1.283 μm and 297.98 mm^3/min ; 1.068°, 1.694 μm and 514.97 mm^3/min ; and 1.448°, 1.975 μm and 667.07 mm^3/min . In this study, surface roughness and kerf taper angle decreased as the waterjet pressure and abrasive mass flow rate increased; and this is showing a direct proportional relationship with traverse speed, abrasive mass flow rate and waterjet pressure.

Keywords: abrasive water jet, contour cutting, surface roughness, kerf taper angle, material removal rate, response surface methodology, multi-objective optimisation

1. Introduction

Contour cutting is one of the processes applied in metal fabrication industries. There are several non-traditional technologies employed for contour cutting, such as electro discharge machining, laser beam machining and electrochemical discharge machining, that have been noted to provide exemplary performance [1]. Accordingly, Abrasive Water Jet Machining (AWJM) is an advanced manufacturing techniques that demonstrated advantages to non-traditional machining technology owing to: its capability in cutting complex geometries, its absence of tool wear, its absence of thermal distortion, and it being environmentally friendly [2, 3]. The cutting process in AWJM is based on removing materials from a target workpiece via erosion [4]. Within this process, contour profiles in various types of programs are downloaded in a

computer-based controller, where subsequently a high-pressure pump releases pressurised water in the nozzle system. The pressurised water, moving with a high velocity, is released from the orifice in a very thin stream structure [5]. The high-speed water jet that contains abrasive particles is then accelerated to generate an abrasive waterjet. Finally, the focusing tube drives the abrasive waterjet to its target point for cutting the material [4, 6]. The compounded granular abrasive and high-pressure waterjet stream makes the abrasive waterjet capable of machining various workpieces, such as metals.

The performance of AWJM is influenced by several process parameters, which can be varied constantly within a period. In general, the primary goal of the metal fabrication industry is to manufacture high quality products in a shortened period. To attain productivity and economy objectives, it is imperative to select an optimum combination of process parameters within the abrasive waterjet cutting processes. Conventionally, the identification of the most suitable values of process parameters is accomplished by the execution of many experiments. Hence, to establish the optimum combination of process parameters in the absence of extensive experimental exertion, researchers have utilised advanced modelling techniques and optimisation in progressing the performance of abrasive waterjet cutting. For instance, Rao et al. [7] have investigated the impacts of traverse speed, standoff distance and abrasive mass flow rate in AWJM of AA631-T6. They have considered single-objective and multi-objective optimisation attributes to achieve optimum solutions by utilising Jaya and MO-Jaya algorithms, which were a posterior optimisation used to solve constrained and unconstrained conditions. The objectives of maximising material removal and minimising kerf taper angle and surface roughness were achieved by lower traverse speed and standoff distance and higher abrasive mass flow rate. Moreover, they determined that multi-objective Jaya algorithm achieved better results as compared with other algorithms, such as simulated annealing (SA), particle swarm optimization (PSO), firefly algorithm (FA), cuckoo search (CS) algorithm, blackhole (BH) algorithm, bio-geography-based optimization (BBO) algorithm, non-dominated sorting genetic algorithm (NSGA), non-dominated sorting teaching-learning-based optimization (NSTLBO) algorithm and sequential approximation optimization (SAQ). Nair and Kumanan [8] have similarly applied weighted principal components analysis (WPCA) for optimising AWJM process parameters in machining Inconel 617. These authors evaluated the impacts of abrasive mass flow rate, standoff distance, table feed and waterjet pressure against material removal rate and geometric accuracy. The WPCA method uses internal tests and training samples to calculate the 'weighted' covariance matrix, establishing that an increase in standoff distance enhances the abrasive flow volume, leading to less geometric errors and a higher rate of material removal. Equivalently, Chakraborty and Mitra [9] have applied the grey wolf optimiser (GWO) technique for AWJM cutting of AL6061 to maximise material removal rate and minimise surface roughness, simultaneously considering the constrained values of input parameters i.e., nozzle diameter and titled angle, jet feed speed, surface speed, waterjet pressure and abrasive mass flow rate. This algorithm demonstrated a faster hunting of prey (discovering the optimum parameter settings), due to the existence of a social hierarchy of grey wolves. They achieved maximum MRR via higher rate of nozzle titled angle, surface speed, waterjet pressure and abrasive mass flow rate. In the case of surface roughness, it attained its minimum value at lower rate of waterjet pressure, jet feed and surface speed and higher rate of abrasive mass flow. Trivedi et al. [10] have examined the impacts of process parameters such as pressure, traverse rate and standoff distance on surface integrity in AWJM

of AISI 316 L. Analysis of variance was employed to develop an empirical model by regression analysis for surface roughness. These authors concluded traverse speed to be the most significant parameter influencing surface roughness, whereby increasing pressure improved the surface quality of the target workpiece. Additionally, they established standoff distances, as the least contributing parameter. Research focused on optimisation of cutting operations is being continuously undertaken by researchers, where varied methods have been employed to solve different single and multi-objective optimisation problems [11–14]. Whereas single-objective optimisation problems have conventionally been applied, the performance of AWJM has mainly been measured based on multiple responses. In accordance, a multi-objective approach is required in order to optimise several categories of objective functions simultaneously. Several methods have been developed to date, and are continuously being progressed, in order to solve single-objective problems. Advances in optimisation techniques, such as: genetic algorithms (GA), simulated annealing (SA), artificial bee colony (ABC), ant colony optimization (ACO), particle swarm optimization (PSO) and teaching-learning-based optimization (TLBO), and others, have been demonstrated to be remarkably efficient in defining the optimum value of AWJM process parameters [15].

In abrasive waterjet contour-cutting, it has been realised that the impacts of most influencing factors, such as waterjet pressure, abrasive mass flow rate, standoff distance and traverse speed in straight-slit cutting, are similar with contour cutting. These research studies have shown the application of computational approaches for optimising process parameters in abrasive waterjet contour cutting requires further investigation. Therefore, this research considers the optimisation of relevant process parameters, including traverse speed, abrasive mass flow rate, and waterjet pressure on surface roughness, material removal rate and kerf taper angle in abrasive waterjet contour cutting of AISI 304L of varied thicknesses.

In this work, the experiment was designed using Taguchi orthogonal array, where a regression model has been developed to formulate the optimisation fitness function. This modelling technique has been applied to predict the response and determine optimum process parameters. In addition, response surface methodology (RSM) has been employed for multi-objective optimization, in order to obtain optimum values of input process parameters and to investigate the impacts and interactions against response parameters.

2. Methodology

In this study, three major steps were employed, consisting of abrasive waterjet contour cutting experiments, regression modelling and optimisation. The experiment, modelling and optimisation procedures are presented in **Figure 1**. The experiment was conducted using the Taguchi L₉ orthogonal array to analyse the impacts of input parameters, i.e., traverse speed, abrasive mass flow rate and waterjet pressure. Desirability analysis using response surface methodology is employed for the experimental results of material AISI 304L. In this desirability analysis, multi-responses are considered. It establishes the optimum set of the selected process parameters on the performance characteristics.

A regression model was developed using the machining process parameters from the experimental execution to extract mathematical models. A linear stepwise regression analysis was performed to predict the surface roughness, material removal rate

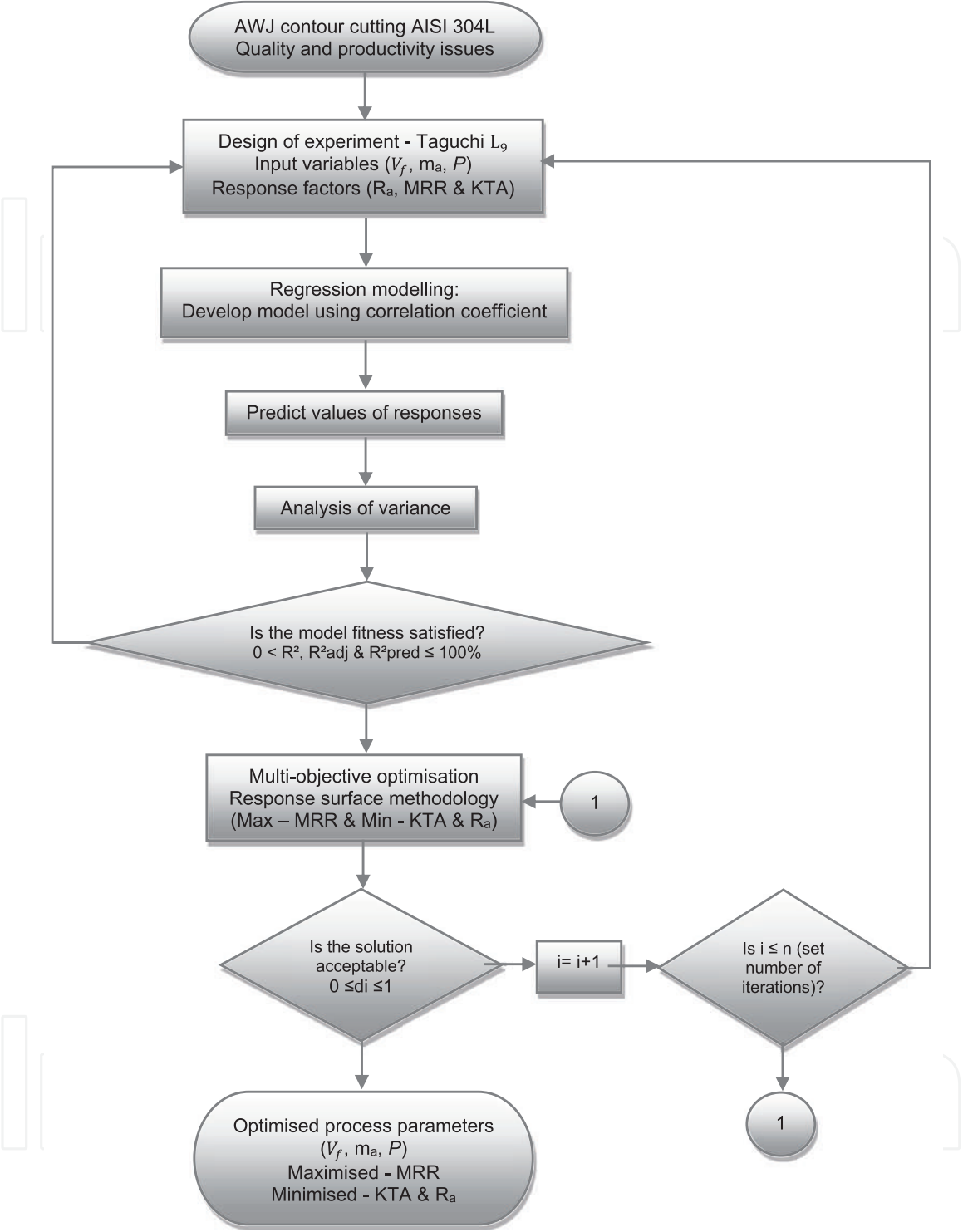


Figure 1.
Multi-objective optimisation process flow chart.

and kerf taper angle value. The reliability of the models generated was assessed based on coefficient of determination (R^2 , R^2_{adj} & R^2_{pred}). However, supposing that regression models are not within the acceptable range or do not provide preferable values of coefficients of determination set by the decision-maker, it is anticipated that these models will not provide precise prediction. Therefore, the selected parameter setting conflicts with the response variables, denoting the necessity for modification of independent variables or experimental design [16].

Referring to **Figure 1**, after achieving the fittest models, a multi-objective optimisation was performed by using response surface methodology with the objectives of maximising material removal, whilst minimising surface roughness and kerf taper angle. The number of solutions and iterations ($i = 1$ to n) may vary, depending on the machining process requirements to establish the best alternative or solution. Hence, if the composite desirability is not within the tolerable array, several iterations repeating the response surface optimisation were executed. Subsequently, if these repetitions reached the maximum number of iterations and the composite desirability is not attaining adequate values, modifying the design of experiments and the corresponding independent variables or its values is necessary [16]. Moreover, in some cases, other soft computing techniques should be considered [17].

2.1 Material and experimental design

In this work, the material machined in the experiments was AISI 304L with varied thicknesses of 4, 8 and 12 mm. The assigned material thicknesses with differing uniform gaps were used to gain a better yield of variations in AWJM cutting behaviour. Stainless steel, such as AISI 304L, is widely used in fabrication industries, where it is recognised for its high strength and corrosion and heat resistance. This results from its high alloying content of Cr and Ni [18]. The chemical and mechanical composition of this material is detailed in **Table 1**.

The setup consisted of an OMAX MAXIEM 1515 abrasive waterjet machine, possessing a direct drive pump and dynamic cutting head with maximum pressure of 413.7 MPa and cutting area of 2235 mm length and 1727 mm width. The cutting head is comprised of a mixing chamber for abrasive and waterjet, along with a nozzle diameter of 0.56 mm and a jet impact angle of 90°. An abrasive garnet with a mesh size of #80 was utilised for abrasive waterjet cutting experiments. The unit is inclusive of IntelliMax software, where the experiment setup conditions were uploaded and entered. The cutting head can move in the Z-axis over a distance of 305 mm, with a maximum traverse speed of 12,700 mm/min. Standoff distance was designated to 1.5 mm in agreement with recommended range for abrasive waterjet machining in previous works [20, 21]. The AWJM setup and process parameters are demonstrated in **Figure 2**.

Chemical composition in wt.%		Mechanical properties	
C	0.03	Hardness, Rockwell B	82
Mn	2	Tensile Strength, Ultimate, MPa	564
Si	0.75	Tensile Strength, Yield, MPa	210
Cr	18.00–20.00	Elongation at Break	58%
Ni	8.00–12.00	Modulus of Elasticity, GPa	193–200
P	0.045		
S	0.03		
Ni	0.1		
Fe	Remaining		

Table 1.
Chemical and mechanical composition of AISI 304L [19].

Upon completion of the experiments, the roughness of the machined surfaces was quantified by a surface roughness tester (TR200 model). **Figure 2** presents the cut surface captured by LEICA M80, which indicates the measurement area for the roughness. The kerf top and bottom width were measured using a LEICA M80 optical microscope model. Moreover, rate of material removal and kerf taper angle were calculated using Eqs. (1) and (2), respectively [11]. The roughness of the cut surface determined according to the ISO/TC 44 N 1770 standard, (μm); W_t is width of the cut surface at the jet inlet, (mm); W_b is the width of the cut surface at the jet outlet, (mm); u is the angularity or perpendicular deviation, (mm); α° - inclination angle of the cut surface, ($^\circ$); MRR is the Material Removal Rate, (mm^3/min); t is the thickness of the material (mm) [22].

$$MRR = ht \left(\frac{W_t + W_b}{2} \right) V_f \quad (1)$$

$$KTA = \text{Arctan} \left(\frac{W_t + W_b}{2ht} \right) \quad (2)$$

The input parameters considered in abrasive waterjet contour cutting in this experiment included traverse rate (V_f), abrasive flow rate (m_a) and water pressure (P), as these parameters have been demonstrated in previous studies as having significant impacts in AWJM applications [10, 12, 23, 24]. Surface integrity, kerf geometries

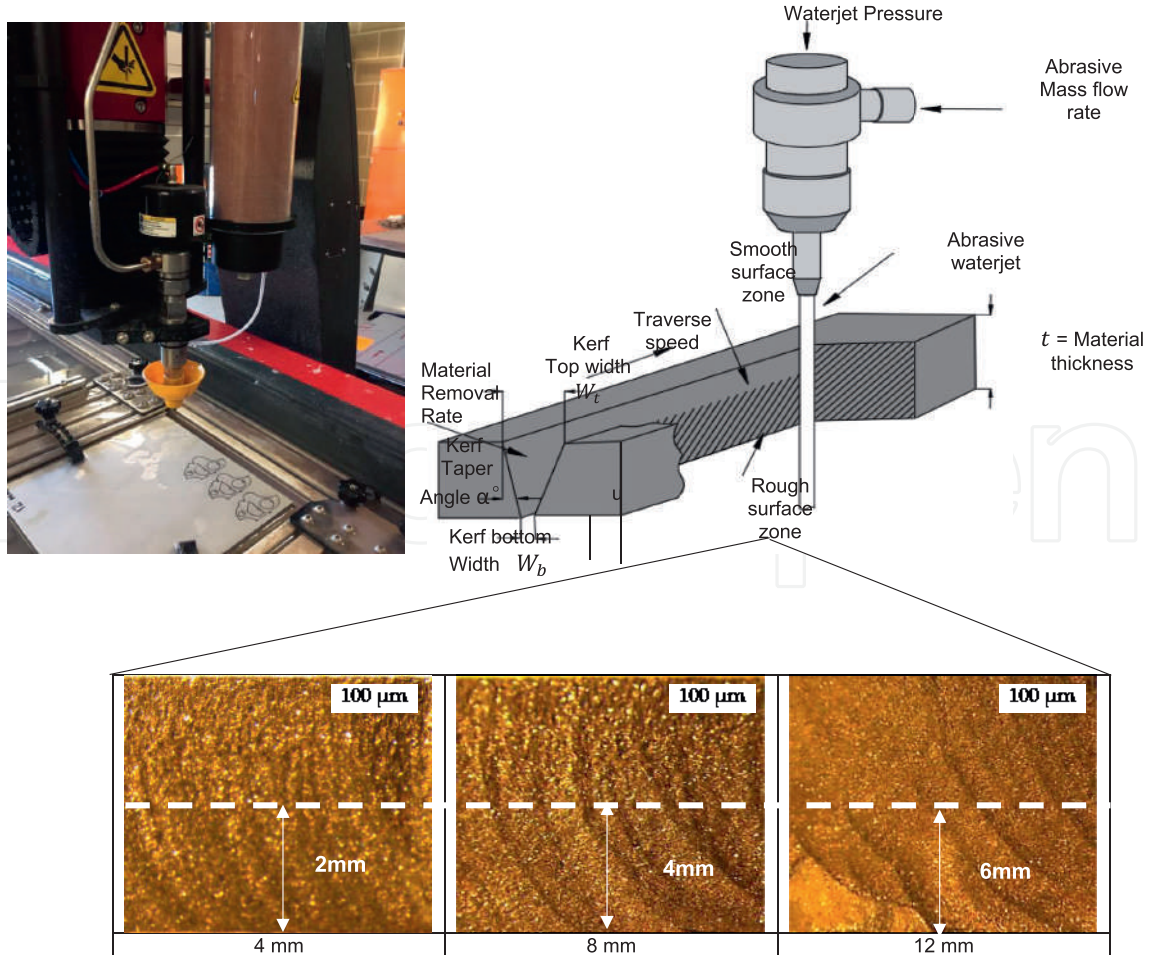


Figure 2.
AWJM setup and process parameters.

and low material removal rate evidence has been reported in machining of AISI 304L, requiring further improvement [4, 25]. Furthermore, taper angles formed in AWJM demonstrate different inclinations as contour curvature radius differs [26]. Hence, quality and productivity are an intensified demand in various manufacturing fields and are significant performance indicators for machining processes. Therefore, in this study, material removal rates (MRR), surface roughness (R_a) and kerf taper angle (KTA) have been chosen as process parameter characteristics for abrasive waterjet contour cutting investigations, due to their influence against the selected input parameters. The levels of the considered independent variables, responses and coding assignment have been detailed in **Tables 2** and **3**.

Abrasive waterjet cutting was executed for three different profiles, representing straight-line, inner arcs and outer arcs, as part of the completed twelve profiles, as demonstrated in **Figure 2**. The abovementioned profiles were selected to confirm a broad array of complicated machining profiling applications. The levels of profiles employed showed occurrences of surface roughness, low machining rate and inaccuracies of cut geometries in regard to previous works [27, 28], recommending further studies, predominantly for difficult-to-cut materials, such as AISI 304L (**Figure 3**).

The design of experimentation (DOE) was carried out using the Taguchi approach in MINITAB 19 software. The Taguchi method is useful in determining the best combination of factors under desired experimental conditions, reducing the large number of experiments which would be required in traditional experiments as the number of process parameter increases [29, 30].

In Taguchi's approach, selection of the appropriate orthogonal array depends on aspects such as: the number of input and response factors along with the interactions that are of key significance; number of levels of data for input factors; and required resolution of experiment and limitations cited on cost and performance [29, 31]. With this specific advantage, this method is suitable in conducting experiments with an appropriate number of tests to determine the optimal combination and significance of the selected factors [32]. The relevant variation in thicknesses dictates different material responses. Therefore, Taguchi L_9 orthogonal array was executed for three

Independent variables	Codes	Levels		
		1	2	3
Traverse speed, V_f = mm/min	X_1	90	120	150
Abrasive mass flow rate, m_a = g/min	X_2	300	400	500
Waterjet pressure, P = MPa	X_3	200	250	300

Table 2.
Levels of input process parameters.

Profiles	Surface roughness, μm	Material removal rate, mm^3/min	Kerf taper angle, $^\circ$
Straight-line, 20 mm	R_{a1}	MRR1	KTA1
Inner arc, R10	R_{a2}	MRR2	KTA2
Outer arc, R20	R_{a3}	MRR3	KTA3

Table 3.
Output parameters for varied profiles.

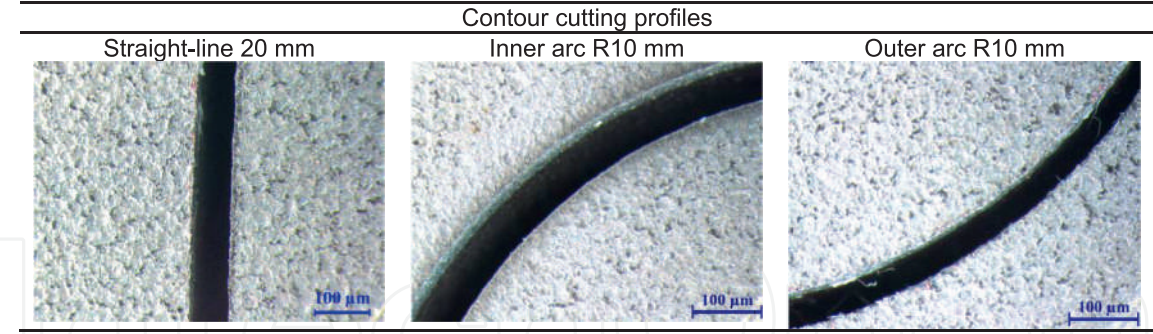


Figure 3.
Abrasive waterjet contour cutting profiles.

Exp. No.	Input Parameters		
	V_f	m_a	P
	(mm/min)	(g/min)	(MPa)
1	90	300	200
2	90	400	250
3	90	500	300
4	120	300	250
5	120	400	300
6	120	500	200
7	150	300	300
8	150	400	200
9	150	500	250

Table 4.
Taguchi L_9 orthogonal array.

levels of material thicknesses (t), i.e., 4, 8 and 12 mm, as presented in **Table 4**. The AWJM performances were analysed accordingly by the applied material thickness.

2.2 Modelling and multi-objective optimisation

A mathematical model was developed to associate the input process parameters to the response’s characteristics. To achieve this, a linear regression was employed to develop models for the prediction of responses. The empirical model for the prediction of the responses in regard to controlling parameters was established by linear regression analysis. Regression analysis was then applied to obtain the interactions between independent and dependent variables [33]. Multi-linear regression involves regression analysis of dependent and independent variables exhibiting a linear relationship [34]. It stipulates the relationship between two or more variables and a response variable by fitting a linear equation to examine data. The value of the independent variable x or process parameter is correlated with a value of the dependent variable, y , which is the output parameter. In general, this analysis is applied to investigate the degree of relationship between multiple variables fitted by a straight line [33].

In general, regression model is expressed by Eq. (3) [33].

$$y = \alpha + \beta_1 x_1 + e \quad (3)$$

$$\text{Wherein : } e = y_1 - \hat{y}_1 \quad (4)$$

where, y = dependent variable, α = constant, x_1 = Independent variable, β_1 = coefficient of independent variable x_1 , e = error, y_1 = regression line values and \hat{y}_1 = actual observation.

If this involves more than one variables, then it is categorised as multi-regression as shown in Eq. (5) [33].

$$y = \alpha + \beta_1 x_1 + \beta_2 x_2 + \beta_3 x_3 + \dots \dots \dots \beta_n x_n + e_n \quad (5)$$

A multi-linear regression analysis can be employed to fit a predictive model to an observed data set of values of output and input variables. The obtained results of surface roughness, material removal rate and kerf taper angle were expressed in terms of the input parameters such as traverse speed (X_1) abrasive mass flow rate (X_2) and waterjet pressure (X_3).

The predicted values are functional for optimising the parameters by providing an adequate comprehension of the significant parameters. The percentage of error between the experimental data and acquired predicted values has been calculated based on Eq. (6) [33]. The relative percentage of error was acceptable at <20% [35].

$$\text{Error} = \frac{1}{n} \sum_n \left[\frac{\text{Response}_{(\text{experiment})} - \text{Response}_{(\text{predicted})}}{\text{Response}_{(\text{experiment})}} \right] \% \quad (6)$$

The performance of the established regression model was assessed by statistical approaches to confirm the goodness-of-fit of the model and the impact of the predicted variables. Following this, the significance and effectiveness of the developed models were validated by *analysis of variance*. *Analysis of variance (ANOVA)* is a statistical method that facilitates the evaluation of comparative influences for each control parameter [36, 37]. The significance of input parameters including traverse speed, abrasive mass flow rate and waterjet pressure were investigated using p - values and determination of coefficient (R^2). In this work, a confidence interval of 95% ($p < 0.05$) has been applied that is in alignment with previous works [29, 38, 39]. A 95% confidence interval means that there is only a 5% chance of being the wrong estimation; therefore, the influence of each process parameter or other interactions on the responses is considered insignificant if their p -values were estimated at more than 0.05 [37].

The determination of coefficient (R^2 , R^2_{adj} and R^2_{pred}) refers to the percentage variation of responses ranging from 0–100%. These indicators determine the adequacy of the model against obtained experimental data and predicted observation. This R^2 , R^2_{adj} and R^2_{pred} value of $\geq 80\%$, proved a better model fits of the obtained data [35].

Response surface methodology (RSM) can be utilised for multi-objective optimisation. This multi-desirability is based on multi-response optimisation using an objective function $D(X)$, denoted as desirability function [40]. This method translates each response (y_i) into a desirability function (d_i), differing in the array of $0 \leq d_i \leq 1$,

where desirability function =0 indicates an undesirable response and desirability function =1 represents a fully desired response [41]. The objective function D is specified by Eq. (7) [40].

$$D = (d_1 \times d_2 \times \dots \times d_n)^{1/n} = \left(\prod_{i=1}^n d_i \right)^{1/n} \quad (7)$$

The effectiveness of multi-objective optimisation is anticipated based on the method used for establishing priority weights for each response characteristics [42]. Generally, equal importance is set for selected responses; hence, weights may differ depending on the machining process requirements in order to establish the most suitable solution [43].

A simultaneous optimisation process was employed to determine the levels of resulting to the maximum overall desirability. The responses namely R_a , MRR and KTA were optimised concurrently to assess the set of input process parameters with the objectives of maximising MRR and minimising R_a and KTA.

3. Results and discussion

3.1 Regression models and analysis for surface roughness

The multi-linear regression coefficients are summarised in **Table 5**, exhibiting the correlation between the input parameters and the output surface roughness for straight-line, inner and outer arc profiles for material thicknesses of 4, 8 and 12 mm. The values of coefficients for all profiles and thicknesses demonstrate a similar trend, showing that constant and variable X_1 is positive and variables X_2 and X_3 are negative. The coefficient indicates the change in the mean response relating in the variation of the specific term, whilst the other term in the model remains constant. The relationship between a term and response is denoted by the sign of the coefficient [44]. The negative correlation coefficient denotes an inverse relationship between variables and responses; and therefore, if it is positive as the coefficient increases, the response mean value also increases. Therefore, an increasing rate of traverse speed (X_1) results in an incremental value of surface roughness. Moreover, an increasing rate of abrasive mass flow and waterjet pressure indicates/obtains a decreasing value of surface roughness. The values of R^2 , R^2_{adj} and R^2_{pred} for 4, 8 and 12 mm ranged from 94.33–99.08%, 90.94–98.52% and 88.66–96.17%, respectively. This indicates that regression models denote an acceptable confirmation of the relationship between the independent variables and R_a response, which denotes a high significance of the model. Therefore, the multi-linear model is reliable and can be utilised in the optimisation of process parameters. It can be observed that the R^2 , R^2_{adj} and R^2_{pred} obtained from straight-line, inner and outer arcs profiles have a uniform gap of at least 2%, which is comparable for all material thicknesses. Hence, this minimal gap denotes an insignificant difference between the surface roughness achieved from straight and curvature profiles [36].

The results detailed in **Table 5** show that the highest value of R^2 , R^2_{adj} and R^2_{pred} for 4 and 8 mm material thickness are achieved in R_{a3} with the values of 97.26, 94.84 and 92.45%; 98.64, 97.82 and 95.06%; 99.08, 98.52 and 96.17% respectively. Thus, R_{a2} achieved the highest percentage of R^2 , R^2_{adj} and R^2_{pred} for 12 mm material thickness

Term	<i>t</i> = 4 mm			<i>t</i> = 8 mm			<i>t</i> = 12 mm		
	R _{a1}	R _{a2}	R _{a3}	R _{a1}	R _{a2}	R _{a3}	R _{a1}	R _{a2}	R _{a3}
	Coef	Coef	Coef	Coef	Coef	Coef	Coef	Coef	Coef
	1.418	1.5394	1.4256	2.097	1.8107	1.76	2.542	2.3854	2.272
β_1	0.003522	0.002944	0.003222	0.009814	0.003483	0.008869	0.005389	0.004276	0.003090
β_2	- 0.000310	- 0.000300	- 0.000217	- 0.001464	- 0.000422	- 0.000577	- 0.000450	- 0.000446	- 0.000515
β_3	- 0.001500	- 0.001300	- 0.001133	- 0.001955	- 0.000977	- 0.001920	- 0.002567	- 0.001924	- 0.001081
Model Summary									
R ²	95.26%	96.77%	97.26%	98.01%	98.16%	98.64%	97.73%	99.08%	94.33%
R ² (adj)	92.41%	92.41%	94.84%	96.82%	97.05%	97.82%	96.37%	98.52%	90.94%
R ² (pred)	90.58%	90.58%	92.45%	93.84%	93.77%	95.06%	93.33%	96.17%	88.66%

Table 5.
Summary of multi-linear regression coefficients for R_a.

with the values of 99.08%, 98.52% and 96.17% accordingly. Therefore, the most fitted and predominant models were R_{a3} for both 4 and 8 mm, and R_{a2} for 12 mm material thickness. The predicted R_a values of regression models applied for straight-line, inner and outer arcs profiles of three levels of material thicknesses are detailed in **Tables 6-8**. The percentage error obtained for 4, 8 and 12 mm AISI 304L thicknesses ranged from -4.22 to 3.44% , 3.30 to 6.71% and -5.75 to 2.49% , respectively. The errors determined for R_a between the predicted value and experimental results are less than 20%, denoting that these models are reliable for predicting R_a values.

Figure 4 presents the residual plot for R_a , consisting of normal probability plot, residual versus fits, histogram for residuals and residuals versus experimental values for the most fitted regression models for 4, 8 and 12 mm, at R_{a3} , R_{a3} and R_{a2} , respectively. Similarly, the normal probability plots for all the material thicknesses demonstrated a close fit to a line in a normal probability graph. The points forming an

Exp. no.	Independent variables			R_{a1} (μm)			R_{a2} (μm)			R_{a3} (μm)		
	X_1	X_2	X_3	Exp.	Pred.	Error %	Exp.	Pred.	Error %	Exp.	Pred.	Error %
1	90	300	200	1.35	1.34	0.81	1.43	1.42	0.61	1.46	1.45	0.56
2	90	400	250	1.25	1.24	1.41	1.33	1.35	-1.56	1.37	1.36	1.06
3	90	500	300	1.09	1.13	-3.99	1.25	1.27	-1.72	1.24	1.26	-2.44
4	120	300	250	1.36	1.37	-1.26	1.46	1.46	-0.39	1.48	1.48	0.22
5	120	400	300	1.29	1.27	2.35	1.42	1.39	3.44	1.40	1.38	1.72
6	120	500	200	1.41	1.39	2.45	1.50	1.48	2.28	1.48	1.48	-0.28
7	150	300	300	1.41	1.40	0.68	1.50	1.50	-0.39	1.49	1.50	-1.11
8	150	400	200	1.48	1.52	-4.22	1.58	1.60	-1.56	1.58	1.60	-2.11
9	150	500	250	1.43	1.42	1.77	1.51	1.52	-0.72	1.53	1.51	2.39

Table 6.
Predicted R_a values of regression models for $t = 4$ mm.

Exp. no.	Independent variables			R_{a1} (μm)			R_{a2} (μm)			R_{a3} (μm)		
	X_1	X_2	X_3	Exp.	Pred.	Error %	Exp.	Pred.	Error %	Exp.	Pred.	Error %
1	90	300	200	2.12	2.15	-3.30	1.81	1.80	1.06	2.01	2.00	0.47
2	90	400	250	1.88	1.91	-2.73	1.72	1.71	0.86	1.86	1.85	0.98
3	90	500	300	1.64	1.66	-2.16	1.60	1.62	-2.04	1.65	1.69	-4.40
4	120	300	250	2.41	2.35	6.71	1.84	1.86	-1.81	2.16	2.17	-1.14
5	120	400	300	2.14	2.10	3.38	1.78	1.77	1.29	2.08	2.02	6.23
6	120	500	200	2.22	2.15	6.30	1.83	1.82	0.74	2.16	2.15	0.79
7	150	300	300	2.52	2.54	-1.89	1.92	1.91	0.63	2.32	2.34	-2.15
8	150	400	200	2.56	2.59	-3.68	1.95	1.97	-1.92	2.46	2.48	-1.58
9	150	500	250	2.32	2.35	-2.62	1.89	1.88	1.18	2.33	2.32	0.79

Table 7.
Predicted R_a values of regression models for $t = 8$ mm.

Exp. no.	Independent variables			R _{a1} (μm)			R _{a2} (μm)			R _{a3} (μm)		
	X ₁	X ₂	X ₃	Exp.	Pred.	Error %	Exp.	Pred.	Error %	Exp.	Pred.	Error %
1	90	300	200	2.39	2.38	1.17	2.26	2.25	0.42	2.18	2.18	−0.09
2	90	400	250	2.20	2.21	−0.50	2.12	2.11	0.60	2.09	2.07	1.20
3	90	500	300	2.00	2.03	−3.17	1.95	1.97	−1.98	1.99	1.97	2.49
4	120	300	250	2.42	2.41	0.83	2.29	2.28	0.30	2.22	2.22	0.69
5	120	400	300	2.25	2.24	1.17	2.16	2.14	2.03	2.05	2.11	−5.75
6	120	500	200	2.48	2.45	3.00	2.29	2.29	−0.39	2.15	2.17	−2.15
7	150	300	300	2.45	2.45	0.50	2.30	2.32	−1.36	2.27	2.26	1.46
8	150	400	200	2.60	2.66	−5.67	2.45	2.46	−1.34	2.32	2.31	0.43
9	150	500	250	2.51	2.48	2.67	2.34	2.32	1.74	2.22	2.21	1.72

Table 8.
Predicted *R_a* values of regression models for *t* = 12 mm.

approximately straight-line and falling along the fitted line denotes that the data is normally distributed and there is a good relation between measured and estimated response values [45]. In general, the residuals versus fits and observation graph for each material thickness display that the points are distributed randomly and near both sides of 0, with no distinguished pattern denoting a minimal deviation within residuals and estimated values. This graph plots the difference between the experimental data as predicted on the y-axis and the fitted or predicted values on the x-axis, to validate the assumption that the residuals have constant variance [46].

Figure 4 also exhibits the histogram graph for *R_a*, illustrating the distribution or frequency of the residuals for all observations. The data shows the frequency of *R_a* for 4, 8 and 12 mm material thicknesses to range from −0.02 to 0.03, −0.05 to 0.05 and −0.02 to 0.02, respectively. The histogram presents distribution of the surface roughness obtained from varying material thicknesses. Figure 4 histogram of residuals denotes that the residuals are normally distributed. These results reveal a minimal interval of inequalities of the experimental data, indicating that the *R_a* models meet their assumptions and are well fitted for the accuracy of prediction [46]. The effects of process parameters were established by ANOVA, where surface roughness results are given in Tables A1-A3 in the Appendix section.

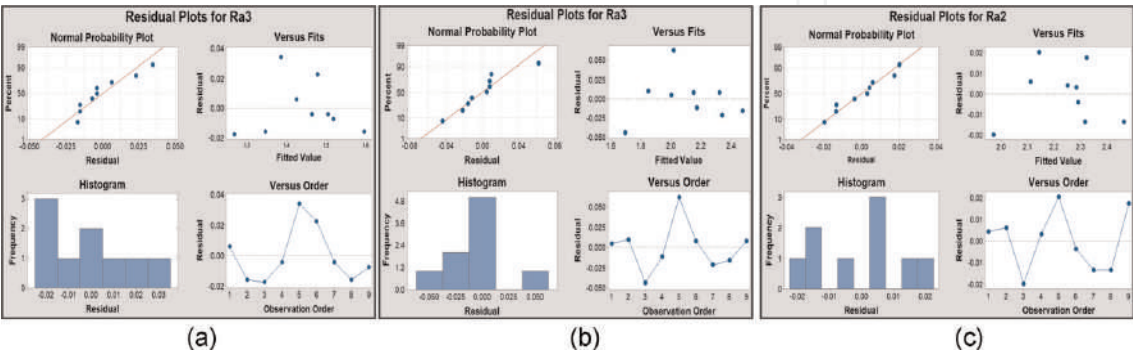


Figure 4.
Residual plots for surface roughness. (a) *R_{a3}* (μm) for *t* = 4 mm (b) *R_{a3}* (μm) for *t* = 8 mm (c) *R_{a2}* (μm) for *t* = 12 mm.

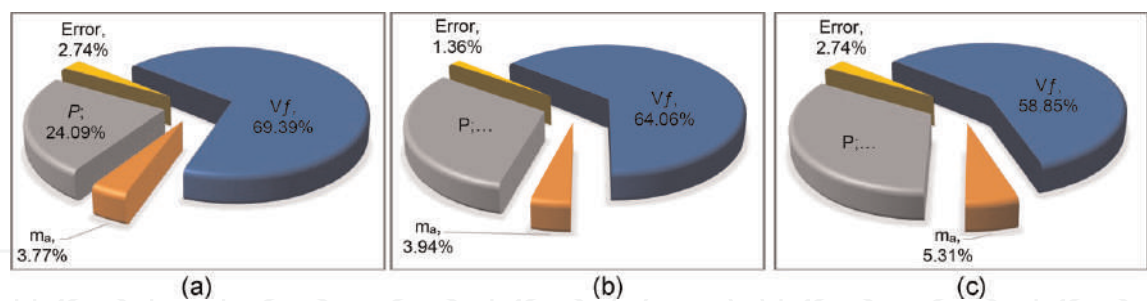


Figure 5. Percentage contribution of variables for surface roughness. (a) R_{a3} (μm) for $t = 4$ mm (b) R_{a3} (μm) for $t = 8$ mm (c) R_{a2} (μm) for $t = 12$ mm.

The impacts of the parameters for all profiles across the three levels of material thicknesses demonstrated a similar trend, denoting traverse speed and waterjet pressure to be significant factors for acquiring p-Values lower than 0.05, as detailed in **Tables A1-A3**. Accordingly, this work has established that abrasive mass flow rate is an insignificant input parameter for obtaining p-Values >0.05 , ranging from 0.002 to 0.067. **Figure 5** represents the percentage contribution of variables for R_a of the most fitted regression models for 4, 8 and 12 mm material thickness. Overall, traverse speed features as the most influencing parameter, followed by waterjet pressure and abrasive mass flow rate. It can be observed here that the influence of traverse speed decreases, ranging from 69.39 to 58.85%, as the material thickness increases. In AWJM, an increasing traverse speed reduces the number of abrasive particles, leading to higher occurrences of surface roughness [47]. **Figure 5** shows that as the material thickness increases, the percentage contribution of waterjet pressure and abrasive mass flow rate also increases, ranging from 24.09 to 33.1% and 3.77 to 5.31%, respectively. The increasing value of waterjet pressure denotes higher energy, reinforcing a larger amount of abrasive particles obtaining lower surface roughness [48]. Further, an increasing rate of abrasive mass flow breaks down abrasive particles into smaller sizes, resulting in more sharp edges that reduce surface roughness [15]. The percentage errors obtained were less than 20%, indicating acceptable reliability of the models, as described in Eq. (6).

3.2 Regression model and analysis for material removal rate

Table 9 displays multi-linear regression coefficients of models developed for material removal rate against input parameters i.e., traverse speed (X_1), abrasive mass flow rate (X_2) and waterjet pressure (X_3) for 4, 8 and 12 mm material thicknesses of AISI 304L. Regardless of material thickness and cutting profile category, the input parameter coefficients acquired a positive sign whilst the constant coefficients had a negative sign. The sign of the coefficient denotes the trend of relationship between variables and response [44]. As a result, an increasing rate of traverse speed, abrasive mass flow rate and waterjet pressure, generates a higher rate of material removal. Overall, the coefficient of determination R^2 ranged from 97.79 to 97.92%, with R^2_{adj} ranging from 96.46 to 96.67% and R^2_{pred} ranging from 92.53 to 94.35%, confirming that all generated regression models were significant. The models were established to be sufficient for accurate forecasting of material removal rate within the assigned levels of input parameters for AWJM of straight and arcs profiles. Furthermore, **Table 9** demonstrated that MRR1 (straight-line), MRR2 (inner

Term	<i>t</i> = 4 mm			<i>t</i> = 8 mm			<i>t</i> = 12 mm		
	MRR1	MRR2	MRR3	MRR1	MRR2	MRR3	MRR1	MRR2	MRR3
	Coef	Coef	Coef	Coef	Coef	Coef	Coef	Coef	Coef
	−84.2	−33	−22.8	−119	−45	−60.6	−158.8	−43.3	−73.5
β_1	1.752	1.562	1.440	2.941	2.658	2.708	3.867	4.476	3.416
β_2	0.1260	0.0833	0.0901	0.2723	0.1738	0.0333	0.3960	0.205	0.2437
β_3	0.5103	0.3430	0.4101	0.7770	0.775	0.950	0.917	0.511	1.080
Model Summary									
R^2	97.92%	97.56%	97.54%	98.86%	97.71%	94.73%	98.70%	96.37%	97.79%
R^2 (adj)	96.67%	96.09%	96.06%	98.18%	96.33%	91.56%	97.92%	94.20%	96.46%
R^2 (pred)	94.35%	90.74%	91.12%	95.73%	91.90%	82.30%	95.19%	89.41%	92.53%

Table 9.
Summary of linear regression coefficients for MRR.

arcs) and MRR3 (outer arcs) attained a uniform gap of at least 2% for R^2 , R^2_{adj} and R^2_{pred} values. This nominal disparity of the coefficient of determination indicates that AWJM performance for straight and curvature profiles are not significantly different from one another [36]. The results detailed in **Table 9** confirm that the highest values of R^2 , R^2_{adj} and R^2_{pred} for all material thicknesses was attained in MRR1 (straight-line profile) with values of 97.92, 96.67 and 94.35%; 98.86, 98.18 and 95.73%; 98.70, 97.92 and 95.19% respectively. This statistical measurement evaluates the relationship between the model and response variables, indicating that a value nearest to 100% denotes a more reliable model [49]. Therefore, MRR1 regression models are considered as the most fitted model for 4, 8 and 12 mm material thicknesses.

Tables 10-12 present the predicted MRR values using the generated regression models of 4, 8 and 12 mm thickness of AISI 304L for three varied contour profiles. The percentage error acquired for 4, 8 and 12 mm AISI 304L thicknesses ranged from −5.35 to 5.15%, −6.59 to 4.77% and − 5.05 to 6.62%, respectively. The errors determined for R_a between the predicted value and experimental results were less than 20%, indicating models to be well fitted for predicting MRR values.

Plots of all residuals of the best material removal rate (MRR1) for all material thicknesses are represented in **Figure 6**. Overall, the normal probability plots for all the material thicknesses illustrate that the adjacency of the points are linear indicating there is no deviation from the assumptions, because they are normally and independently distributed [46]. Residuals versus fits and observation for MRR1 of straight-line, inner and outer arc profiles confirm that there is no skewness or outlier pattern, revealing that individual deviated assumptions have no conflicts or contradictions. **Figure 6** also presents the histogram graph for MRR1, obtaining frequency ranging from −10 to 15 for 4 mm, −15 to 15 for 8 mm and − 18 to 20 for 12 mm material thicknesses. These results signify that the distribution or frequency of residuals for all observations fell in minimal interval or inequalities of the experimental data, justifying the adequacy of the suggested MRR1 models [46].

According to the results presented in **Tables A4-A6** in the Appendix section, detailing ANOVA for material removal rate, the effects of the input parameters for

Exp. no.	Independent variables			MRR 1 (mm ³ /min)			MRR 2 (mm ³ /min)			MRR 3 (mm ³ /min)		
	X ₁	X ₂	X ₃	Exp.	Pred.	Error %	Exp.	Pred.	Error %	Exp.	Pred.	Error %
1	90	300	200	216.2	213.3	1.36	212.1	201.2	5.15	217.7	215.9	0.83
2	90	400	250	248.6	251.4	−1.10	223.1	226.7	−1.60	242.4	245.5	−1.27
3	90	500	300	284.2	289.5	−1.86	250.6	252.1	−0.62	267.8	275.0	−2.68
4	120	300	250	280.6	291.3	−3.82	251.7	265.2	−5.35	283.0	279.6	1.19
5	120	400	300	342.5	329.4	3.82	293.7	290.7	1.03	313.7	309.2	1.44
6	120	500	200	298.8	291.0	2.61	263.5	264.7	−0.45	286.2	277.2	3.14
7	150	300	300	372.1	369.4	0.73	333.8	329.2	1.38	343.9	343.4	0.16
8	150	400	200	330.7	330.9	−0.07	299.6	303.2	−1.21	298.5	311.4	−4.32
9	150	500	250	361.5	369.1	−2.09	333.5	328.7	1.44	344.8	340.9	1.14

Table 10.
Predicted MRR values of regression model for t = 4 mm.

Exp. no.	Independent variables			MRR 1 (mm ³ /min)			MRR 2 (mm ³ /min)			MRR 3 (mm ³ /min)		
	X ₁	X ₂	X ₃	Exp.	Pred.	Error %	Exp.	Pred.	Error %	Exp.	Pred.	Error %
1	90	300	200	367.9	382.8	−4.05	405.0	401.4	0.88	399.0	383.0	4.00
2	90	400	250	456.9	448.9	1.75	450.8	457.6	−1.50	427.2	433.8	−1.56
3	90	500	300	511.2	515.0	−0.74	501.8	513.7	−2.37	493.1	484.7	1.71
4	120	300	250	526.9	509.9	3.23	526.4	519.9	1.23	488.1	511.7	−4.84
5	120	400	300	572.9	576.0	−0.54	583.5	576.1	1.27	579.8	562.6	2.97
6	120	500	200	532.9	525.5	1.39	532.2	515.9	3.06	441.8	470.9	−6.59
7	150	300	300	633.7	637.0	−0.52	639.7	638.4	0.19	629.1	640.5	−1.81
8	150	400	200	583.9	586.5	−0.45	555.1	578.3	−4.17	576.3	548.8	4.77
9	150	500	250	647.8	652.6	−0.74	641.3	634.5	1.07	601.3	599.6	0.28

Table 11.
Predicted MRR values of regression model for t = 8 mm.

straight and arc profiles at 4, 8 and 12 mm AISI 304L thicknesses display comparable results. Further, the results reveal that traverse speed and waterjet pressure are statistically and physically significant factors for obtaining p -Values<0.05. Hence, the abrasive mass flow rate features as a low impacting input parameter for obtaining p -Values greater than the acceptable value of 0.05, ranging from 0.002 to 0.751.

The percentage contribution of variables for the most fitted regression models MRR for 4, 8 and 12 mm material thicknesses are illustrated in **Figure 6**. In general, traverse speed is indicated as the most impacting variable, followed by waterjet pressure and abrasive mass flow rate, with a percent contribution ranging from 71.14–78.94%, 12.11–24.09% and 2.65–9.03% respectively for all profiles and material thicknesses. It is apparent here that the percentage contribution of traverse speed increases

Exp. no.	Independent variables			MRR 1 (mm ³ /min)			MRR 2 (mm ³ /min)			MRR 3 (mm ³ /min)		
	X ₁	X ₂	X ₃	Exp.	Pred.	Error %	Exp.	Pred.	Error %	Exp.	Pred.	Error %
1	90	300	200	472.0	491.5	−4.13	506.3	523.4	−3.37	528.9	523.1	1.10
2	90	400	250	586.2	576.9	1.58	542.1	569.5	−5.05	588.7	601.5	−2.17
3	90	500	300	655.9	662.4	−0.99	625.7	615.6	1.62	665.4	679.9	−2.18
4	120	300	250	676.0	653.4	3.35	731.7	683.2	6.62	687.5	679.6	1.15
5	120	400	300	735.0	738.8	−0.51	735.8	729.3	0.88	772.3	758.0	1.85
6	120	500	200	701.2	686.7	2.07	712.3	698.7	1.90	695.1	674.4	2.98
7	150	300	300	813.0	815.2	−0.27	822.4	843.1	−2.51	835.4	836.1	−0.09
8	150	400	200	755.6	763.1	−1.00	811.9	812.5	−0.07	725.0	752.5	−3.79
9	150	500	250	841.6	848.6	−0.83	845.6	858.6	−1.54	837.6	830.9	0.80

Table 12.
Predicted MRR values of regression model for t = 12 mm.

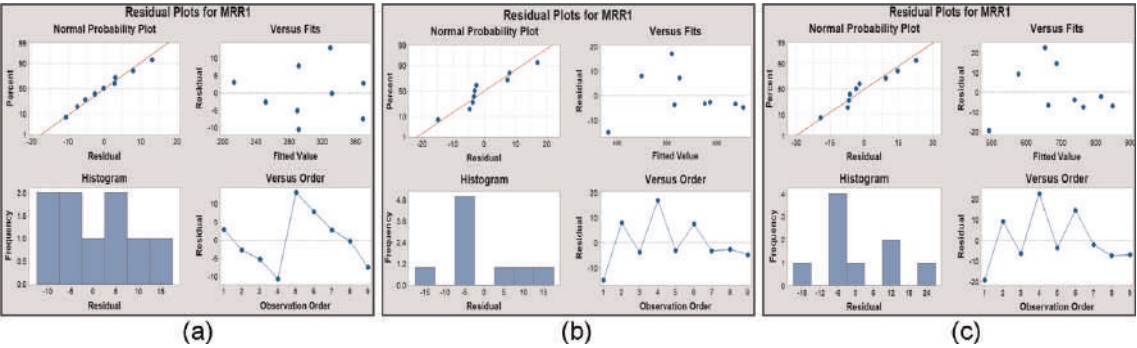


Figure 6.
Residual plots for material removal rate. (a) MRR 1 (mm³/min) for t = 4 mm (b) MRR 1 (mm³/min) for t = 8 mm (c) MRR (mm³/min) for t = 12 mm.

in range from 71.4 to 77.55% as the material thickness increases. An increasing traverse speed reinforces the contact time of the waterjet with the abrasive on the material, producing a higher volume rate of material to the machine [9]. Contrastingly, the percentage contribution of waterjet pressure and abrasive mass flow rate decreased as the material thickness and traverse speed increased, ranging from 22.42–12.11% and 4.35–9.03%, respectively. The increasing traverse speed and depth or thickness of the material to cut, results in a more prolonged machining process, which gradually leads to subsiding kinetic energy and loss of large of abrasive particles, resulting in reduced effectiveness of abrasive mass flow rate and waterjet pressure during the erosion process (**Figure 7**) [9, 47].

3.3 Regression model and analysis for kerf taper angle

The summary of the multi-linear regression coefficients for kerf taper angle of straight-line, inner and outer arc profiles using 4, 8 and 12 mm material thicknesses are detailed in **Table 13**. The results provide a similar trend, showing the constant sign

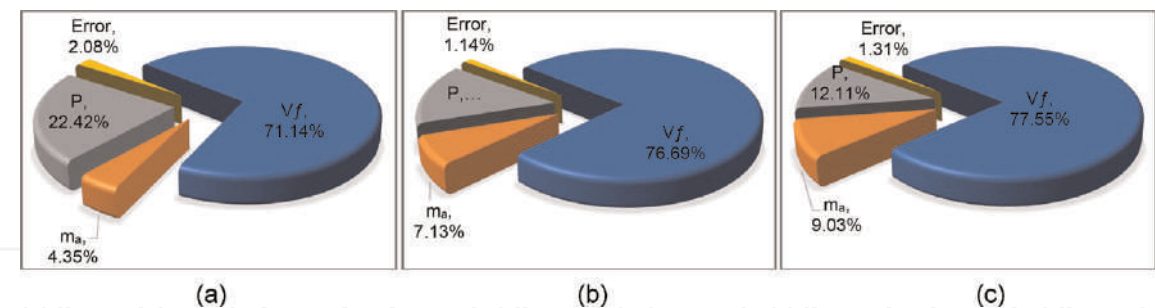


Figure 7. Percentage contribution of variables for material removal rate. (a) MRR 1 (mm^3/min) for $t = 4 \text{ mm}$ (b) MRR 1 (mm^3/min) for $t = 8 \text{ mm}$ (c) MRR (mm^3/min) for $t = 12 \text{ mm}$.

as positive, with variables X_1 , X_2 and X_3 as negative for all profiles and thicknesses. If the coefficient sign is negative, as the variable increases, the response decreases, whereas if the coefficient is positive, the relationship between variables and responses is directly proportional [44]. Therefore, an increasing rate of traverse speed (X_1) results in an increasing angle of the kerf taper. Thus, an increasing rate of abrasive mass flow and waterjet pressure reduces the value of kerf taper angle. The values of R^2 , R^2_{adj} and R^2_{pred} for 4, 8 and 12 mm ranged from 94.74–99.37%, 91.59–98.99% and 80.11–97.66%, respectively. This confirms that regression models are reliable in representing correlation between variables and responses and can be used in the optimisation of process parameters.

The coefficient of determination (R^2 , R^2_{adj} and R^2_{pred}) obtained from straight-line, inner and outer arc profiles for all material thicknesses had a similar and consistent gap of at least 2%. The AWJM provides comparable behaviour in processing both straight and curvature profiles [36]. The highest values of R^2 , R^2_{adj} and R^2_{pred} for 4 and 8 mm material thicknesses were attained in KTA1 with values of 97.56, 96.09 and 90.57%; 98.02, 96.82 and 92.01%; 99.37, 98.99 and 97.66%, respectively. These are the most fitted model, to be utilised in the optimisation of the process parameters of this study.

The predicted KTA values using the regression models applied for straight-line, inner and outer arc profiles of the three levels of material thicknesses are detailed in **Tables 14-16**. The percentage error obtained for 4, 8 and 12 mm AISI 304L thicknesses ranged between -2.55 to 1.72% , -2.67 to 3.74% and -3.14 to 2.43% , respectively. The errors calculated for KTA between the predicted value and experimental results were less than the acceptable maximum limit of 20%, indicating the reliability of the models in predicting KTA values.

Figure 8 illustrates the residual plot for KTA including normal probability plot, residual versus fits, histogram for residuals and residuals versus experimental values. The results showed that the most fitted regression model is achieved from KTA1 for all material thicknesses. Correspondingly, the normal probability plots for all material thicknesses present a near fit to a line in a normal probability graph. The points constructing an approximate straight-line and plotted along the fitted line signifies that the data is normally distributed and there is a good relation between experimental data and predicted values [45]. Predominantly, the residuals versus fits and observation graph for each material thickness exhibit that the points are plotted randomly and near both sides of 0 with no identified pattern denoting a minimal deviation within residuals and estimated values. **Figure 8** also presents the histogram graph for KTA

Term	<i>t</i> = 4 mm			<i>t</i> = 8 mm			<i>t</i> = 12 mm		
	KTA1	KTA2	KTA3	KTA1	KTA2	KTA3	KTA1	KTA2	KTA3
	Coef	Coef	Coef	Coef	Coef	Coef	Coef	Coef	Coef
	0.9674	1.0469	1.064	1.386	1.483	1.544	1.5981	1.971	1.998
β_1	0.002414	0.002155	0.001501	0.006143	0.003594	0.004333	0.006568	0.004556	0.004736
β_2	- 0.000235	- 0.000220	- 0.000136	−0.00052	−0.000525	−0.00035	- 0.000107	- 0.000400	- 0.000436
β_3	- 0.000932	- 0.000952	- 0.000668	−0.002039	−0.001346	- 0.001867	- 0.002319	- 0.002320	- 0.002286
Model Summary									
R ²	97.56%	97.26%	94.74%	98.02%	94.76%	96.79%	99.37%	96.30%	96.95%
R ² (adj)	96.09%	95.61%	91.59%	96.82%	91.61%	94.87%	98.99%	94.08%	95.12%
R ² (pred)	90.57%	88.61%	84.48%	92.01%	80.11%	88.29%	97.66%	86.50%	88.70%

Table 13.
Summary of linear regression coefficients for KTA.

Exp. no.	Independent variables			KTA1 (°)			KTA2 (°)			KTA3 (°)		
	X ₁	X ₂	X ₃	Exp.	Pred.	Error %	Exp.	Pred.	Error %	Exp.	Pred.	Error %
1	90	300	200	0.93	0.93	0.23	0.99	0.98	0.41	1.02	1.02	−0.19
2	90	400	250	0.86	0.86	0.26	0.92	0.92	0.84	0.98	0.98	0.15
3	90	500	300	0.77	0.79	−2.30	0.83	0.85	−2.16	0.94	0.93	0.53
4	120	300	250	0.95	0.95	−0.60	1.00	1.00	0.16	1.04	1.04	0.78
5	120	400	300	0.90	0.88	1.74	0.94	0.93	1.33	0.96	0.99	−2.55
6	120	500	200	0.97	0.95	1.72	1.00	1.01	−0.20	1.05	1.04	0.70
7	150	300	300	0.98	0.98	0.34	1.01	1.02	−0.80	1.06	1.05	1.13
8	150	400	200	1.03	1.05	−1.70	1.08	1.09	−1.44	1.09	1.10	−1.21
9	150	500	250	0.98	0.98	0.09	1.04	1.02	1.68	1.06	1.05	0.54

Table 14.
Predicted KTA values of regression model for t = 4 mm.

Exp. no.	Independent variables			KTA1 (°)			KTA2 (°)			KTA3 (°)		
	X ₁	X ₂	X ₃	Exp.	Pred.	Error %	Exp.	Pred.	Error %	Exp.	Pred.	Error %
1	90	300	200	1.38	1.38	0.04	1.40	1.38	1.42	1.43	1.46	−1.83
2	90	400	250	1.22	1.22	−0.12	1.27	1.26	0.76	1.34	1.33	0.91
3	90	500	300	1.04	1.07	−2.65	1.13	1.14	−0.94	1.21	1.20	0.87
4	120	300	250	1.48	1.46	1.50	1.43	1.42	0.43	1.54	1.49	3.07
5	120	400	300	1.35	1.30	3.42	1.30	1.30	−0.07	1.35	1.36	−1.07
6	120	500	200	1.44	1.46	−0.81	1.34	1.38	−3.20	1.49	1.52	−1.75
7	150	300	300	1.50	1.54	−2.67	1.44	1.46	−1.67	1.50	1.53	−1.96
8	150	400	200	1.68	1.69	−0.61	1.53	1.54	−0.81	1.70	1.68	1.11
9	150	500	250	1.56	1.54	1.41	1.48	1.42	3.74	1.56	1.55	0.46

Table 15.
Predicted KTA values of regression model for t = 8 mm.

illustrating the distribution or frequency of the residuals for all observations. The results show that the frequency of KTA for 4, 8 and 12 mm material thicknesses range from −0.002 to 0.015, −0.05 to 0.05 for 8 mm and − 0.02 to 0.03, respectively. These graphs reveal a minimal interval or inequalities of the experimental data indicating that the KTA regression models are highly fitted to concrete prediction [46].

Tables A7-A9 in the Appendix section detail the results of ANOVA, where it can be observed that the impacts of parameters for all profiles and three levels of material thicknesses demonstrate a similar trend, denoting traverse speed and waterjet pressure to be significant factors for acquiring *p*-Values lower than 0.05. Thus, the abrasive mass flow rate was found insignificant for achieving *p*-Values >0.05, ranging from 0.002 to 0.245 for all profiles and material thicknesses.

Exp. no.	Independent variables			KTA1 (°)			KTA2 (°)			KTA3 (°)		
	X ₁	X ₂	X ₃	Exp.	Pred.	Error %	Exp.	Pred.	Error %	Exp.	Pred.	Error %
1	90	300	200	1.70	1.69	0.39	1.80	1.80	0.18	1.85	1.84	0.49
2	90	400	250	1.57	1.57	0.07	1.63	1.64	−0.48	1.67	1.68	−0.26
3	90	500	300	1.43	1.44	−0.70	1.45	1.49	−2.20	1.49	1.52	−2.08
4	120	300	250	1.79	1.77	0.87	1.83	1.82	0.92	1.88	1.86	0.88
5	120	400	300	1.65	1.65	0.14	1.67	1.66	0.60	1.71	1.71	0.43
6	120	500	200	1.86	1.87	−0.72	1.90	1.85	2.43	1.92	1.89	1.51
7	150	300	300	1.84	1.86	−0.85	1.85	1.84	0.52	1.89	1.89	0.13
8	150	400	200	2.06	2.08	−0.81	1.97	2.03	−3.14	2.02	2.08	−2.93
9	150	500	250	1.98	1.95	1.51	1.89	1.87	0.82	1.95	1.92	1.55

Table 16.
Predicted KTA values of regression model for $t = 12\text{ mm}$.

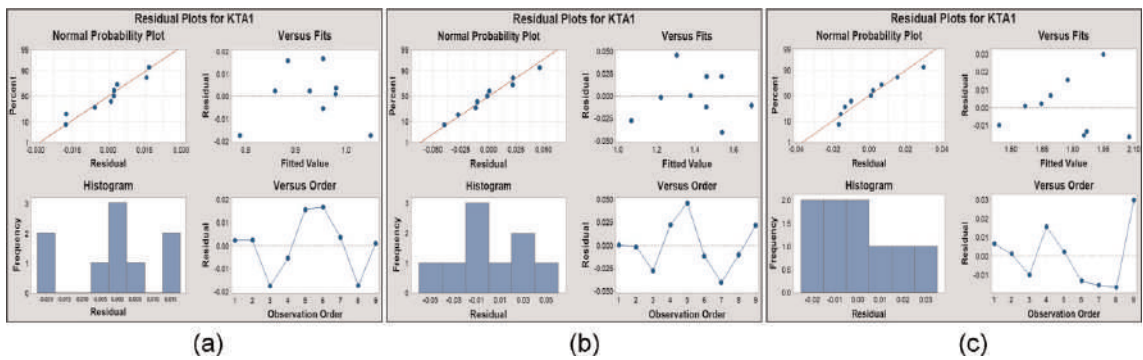


Figure 8.
Residual plots for kerf taper angle. (a) KTA1 (°) for $t = 4\text{ mm}$ (b) KTA1 (°) for $t = 8\text{ mm}$ (c) KTA1 (°) for $t = 12\text{ mm}$.

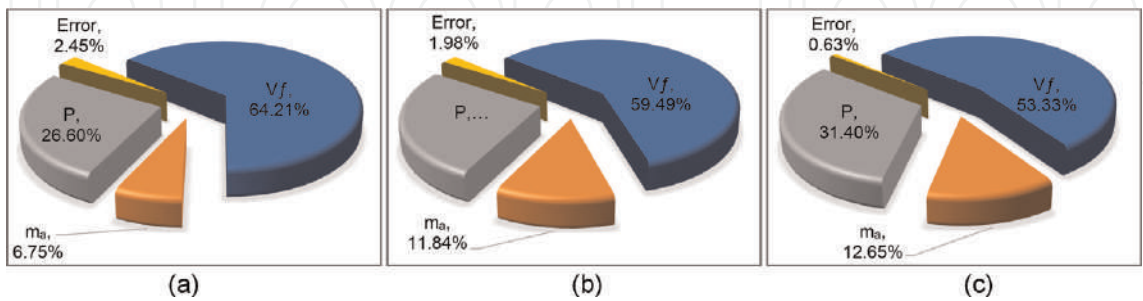


Figure 9.
Percentage contribution of variables for kerf taper angle. (a) $t = 4\text{ mm}$ (b) $t = 8\text{ mm}$ (c) $t = 12\text{ mm}$.

Figure 9 exhibits the percentage contribution of variables for KTA for the most fitted regression models for 4, 8 and 12 mm material thickness. Traverse speed was the most influencing parameter, followed by waterjet pressure and abrasive mass flow rate, in agreement with previous studies [14, 37]. The obtained

results have shown that the influence of traverse speed decreases in range from 64.21 to 53.33% as the material thickness increases. An increasing value traverse speed results in the loss of a large number of abrasive particles, continuously dropping as the material thickness also increases, leading to a higher angle of kerf taper [50]. **Figure 9** shows increases of material thickness, the percentage contribution of waterjet pressure and abrasive mass flow rate, ranging from 26.60 to 33.40% and 6.75 to 12.65%, respectively. This increasing value of waterjet pressure resulted in higher energy, generating a larger amount of abrasive particles that result in a lower kerf taper [51]. Moreover, a rising rate of abrasive mass flow breaks down abrasive particles into a smaller scale, generating more sharp points that results in reduction of kerf taper angle [51].

4. Response surface methodology multi-objective optimisation

In this research, multi-objective optimisation was performed using RSM to determine the optimum process parameters of abrasive waterjet contour cutting of AISI 304L with varied thicknesses using MINITAB 19 software. The following optimisation objectives were stated as follows:

$$f_1 = \text{Min} (R_a) \quad (8)$$

$$f_2 = \text{Min} (KTA) \quad (9)$$

$$f_3 = \text{Max} (MRR) \quad (10)$$

RSM optimisation was performed using the models with the highest determination of coefficients, i.e., R^2 , R^2_{adj} and R^2_{pred} . Accordingly, the regression models utilised to minimise surface roughness were R_{a3} for 4 and 8 mm and R_{a2} for 12 mm. MRR1 and KTA 1 models were used for all material thicknesses.

The Regression models utilised in multi-objective optimisation for varied thicknesses of AISI 304L were expressed by Eqs. (8)-(16).

$$Ra_{4\text{mm}} = 1.4256 + 0.003222 X_1 - 0.000217 X_2 - 0.001133 X_3 \quad (11)$$

$$KTA_{4\text{mm}} = 0.9674 + 0.002414 X_1 - 0.000235 X_2 - 0.000932 X_3 \quad (12)$$

$$MRR_{4\text{mm}} = -84.2 + 1.752 X_1 + 0.126 X_2 + 0.5103 X_3 \quad (13)$$

$$Ra_{8\text{mm}} = 1.76 + 0.008869 X_1 - 0.000577 X_2 - 0.001920 X_3 \quad (14)$$

$$KTA_{8\text{mm}} = 1.386 + 0.006143 X_1 - 0.000520 X_2 - 0.002039 X_3 \quad (15)$$

$$MRR_{8\text{mm}} = -119 + 2.941X_1 + 0.2723 X_2 + 0.777X_3 \quad (16)$$

$$Ra_{4\text{mm}} = 2.3854 + 0.004276 X_1 - 0.000446 X_2 - 0.001924 X_3 \quad (17)$$

$$KTA_{4\text{mm}} = 1.5981 + 0.006568 X_1 - 0.000107 X_2 - 0.002319 X_3 \quad (18)$$

$$MRR_{8\text{mm}} = -158.8 + 3.867X_1 + 0.396 X_2 + 0.917 X_3 \quad (19)$$

In simultaneous optimisation, goals and boundaries must be defined for each process parameter. Targets are based on the experimental data obtained, referring to the set highest value of responses for maximising MRR and lowest value of responses for minimising R_a and KTA. In this optimisation, process parameters and defined objectives were assigned to be equally significant. Therefore, the equal weights

(wt. = 1) were assigned in order to achieve an equal importance to the process parameters and objectives. The constraints referring to range and limits of the process parameters are detailed below.

Constraints:

$$90 \leq V_f \leq 150 \text{ mm/min}$$

$$300 \leq m_a \leq 500 \text{ g/min}$$

$$200 \leq P \leq 300 \text{ g/min}$$

Limits:

$$KTA_{4\text{mm}} \leq 1.03^\circ, KTA_{8\text{mm}} \leq 1.68^\circ, KTA_{12\text{mm}} \leq 2.06^\circ$$

$$Ra_{4\text{mm}} \text{ mm} 1.58 \mu\text{m}, Ra_{8\text{mm}} \text{ mm} 2.45 \mu\text{m}, Ra_{12\text{mm}} \text{ mm} 2.46 \mu\text{m}$$

$$MRR_{4\text{mm}} \geq 216.20 \text{ mm}^3/\text{min}, MRR_{8\text{mm}} \geq 367.90 \text{ mm}^3/\text{min},$$

$$MRR_{12\text{mm}} \geq 472.00 \text{ mm}^3/\text{min}$$

Table 17 shows the solutions for multi-objective optimisation performed for 4, 8 and 12 mm thickness of AISI 304L. The solution that provides the value of composite desirability nearest to 1 can be considered as the best solution [40]. **Table 17** reveals that solution 1 is the best for 4, 8 and 12 mm material thicknesses, achieving composite desirability values of 0.748448, 0.780587 and 0.786800, respectively. There are three solutions generated from MINITAB application, providing the settings of input variables, achieved values of responses and composite desirability. Solution 1 provides the optimum settings of input parameters i.e., V_f for 4, 8 and 12 mm material thicknesses, at the speeds of 95, 90 and 91 mm/min, respectively. The obtained optimum setting for m_a and P were found to be the same value for all material thicknesses, at 500 g/min and 200 MPa, respectively. **Table 17** presents the minimum achieved values of KTA and R_a and maximum MRR for 4, 8 and 12 mm material thicknesses, featuring at 0.799° , $1.283 \mu\text{m}$ and $297.98 \text{ mm}^3/\text{min}$; 1.068° , $1.694 \mu\text{m}$ and $514.97 \text{ mm}^3/\text{min}$ and 1.448° , $1.975 \mu\text{m}$ and $667.07 \text{ mm}^3/\text{min}$, respectively.

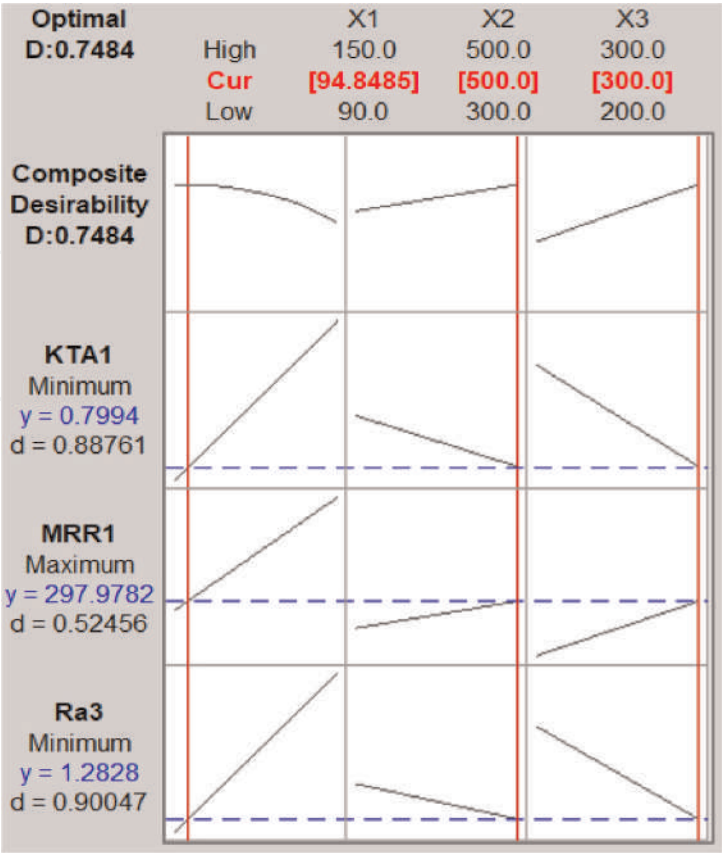
An optimisation plot presenting how the variables affected the predicted responses is shown in **Figure 10**, detailing the composite desirability for multi-objective (D) and single-objective optimisation (d). Current variable settings for the input parameters are presented in the figure, alongside with lower and upper limits. **Figure 10** shows a three-sectioned line graph representing the correlation of KTA, R_a and MRR against traverse speed (X_1), abrasive mass flow rate (X_2) and waterjet pressure (X_3).

From the figure, it can be observed that abrasive waterjet contour cutting responses demonstrate a comparable behaviour against input parameters for all material thicknesses. The highest rate of material removal and lowest value of surface roughness and Kerf taper angle were achieved by employing a rate of 150 mm/min speed, 500 g/min abrasive mass flow rate, and 300 MPa of waterjet pressure. Increasing water pressure, alongside high velocity abrasive mass flow rate, produces a greater collision of abrasive particles, generating higher rate of material removal and reducing surface roughness and kerf taper angle [52].

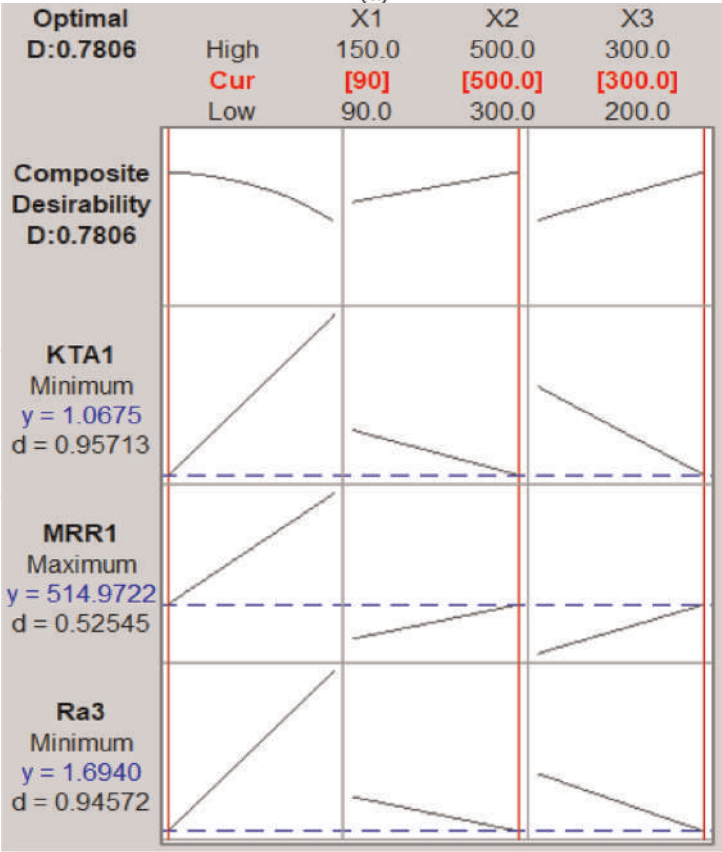
The surface roughness displayed an incrementing value that ranged from 4–13% as the rate of traverse speed increased from 90 to 150 mm/min. As the speed increases per unit of area over time, the kinetic energy containing abrasives gradually decreases, resulting in greater evidences of rough surfaces [52]. Consequently, RSM optimisation

Parameters	4 mm			8 mm			12 mm		
	Solutions								
	1	2	3	1	2	3	1	2	3
$X_1 = V_f$ (mm/min)	95	97	97	90	90	116	91	90	90
$X_2 = m_a$ (g/min)	500	500	500	500	500	301.737	500	500	500
$X_3 = P$ (MPa)	300	300	300	300	300	300	300	300	300
KTA (°)	0.799	0.805	0.805	1.068	1.068	1.330	1.448	1.441	1.441
MRR (mm ³ /min)	297.98	302.17	302.17	514.97	514.97	537.49	667.07	662.78	662.78
R _a (µm)	1.283	1.291	1.291	1.694	1.694	2.039	1.975	1.970	1.970
Composite Desirability	0.748448	0.748075	0.748075	0.780587	0.780587	0.556566	0.786800	0.786677	0.786677

Table 17.
Solutions for RSM multi-objective optimisation.



(a)



(b)

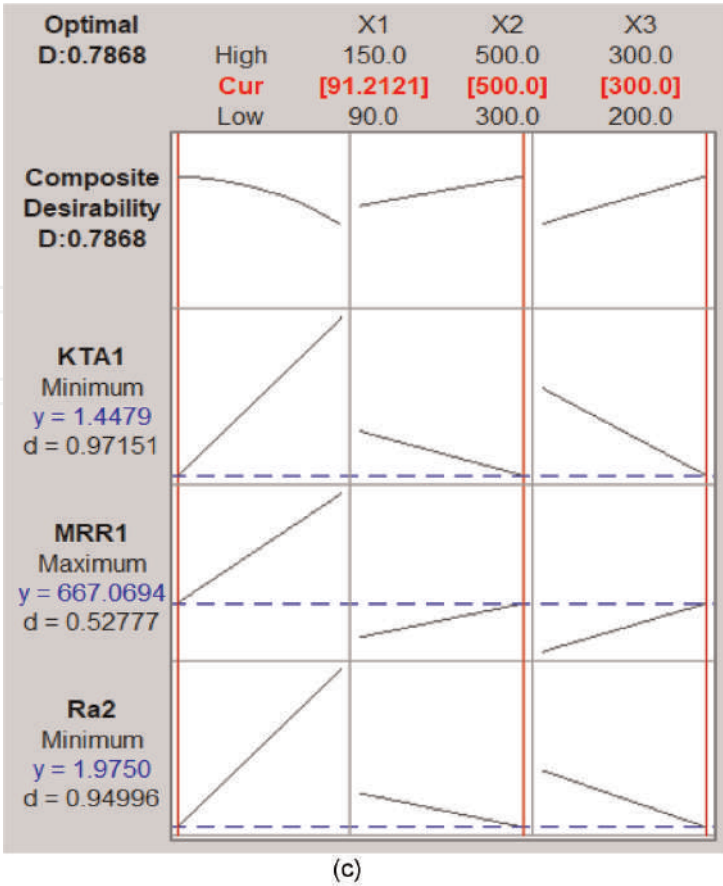


Figure 10.
Response optimisation plot. (a) $t = 4\text{ mm}$ (b) $t = 8\text{ mm}$ (c) $t = 12\text{ mm}$.

has shown that a lower level of traverse speed can produce a better quality of cut surface. Additionally, surface roughness in this study shows an increasing value ranging 2–5%, as the waterjet pressure increases and the abrasive mass flow rate from 200 to 300 MPa and 300 to 500 g/min, respectively. In this study, it is confirmed that augmenting abrasive flow rate and waterjet pressure, up to a specific range, lowers the value of surface roughness. When higher values of traverse speed are employed, the material removal exhibits an increasing rate that ranges from 16–20%. In addition, increasing rate of material removal was achieved with a range of 5–9%, as the rate of abrasive mass flow and waterjet pressure increased from 200 to 300 MPa and 300 to 500 g/min, respectively. AWJM produces a high level of kinetic energy, driving a higher level of speed and waterjet pressure alongside with abrasive mass flow rate, which in turn generates higher cutting area per unit of time and generates a larger amount of eroded material [53]. Therefore, the rate of material removal is directly proportional to traverse speed, abrasive mass flow rate and waterjet pressure. **Figure 10** shows that kerf taper angle values increase as the rate of traverse speed increases from 90 to 150 mm/min. With continuous reduction in the number of abrasive particles, as the traverse speed increases, the cohesion on metal material decreases, generating a higher tapering angle [52]. The kerf taper angle in this study was reduced by 2–7%, as the abrasive mass flow and waterjet pressure were increased from 200 to 300 MPa and 300 to 500 g/min, respectively. A higher waterjet pressure alongside with abrasive mass flow rate reinforces the collision of abrasive particles on the target material, causing the reduction of kerf taper angle [51].

5. Conclusions

This study focuses on modelling and establishing optimum abrasive waterjet contour cutting parameters that lead to minimum surface roughness, kerf taper angle and maximum productivity (material removal rate). On the basis of the results achieved and discussed, the following conclusions are accomplished:

1. The experimental results indicate that abrasive waterjet contour cutting responses demonstrate similar behaviour against input parameters for straight-line and curvature profiles. The correlation coefficients of the predictive models of R^2 , R^2_{adj} and R^2_{pred} for surface roughness, kerf taper angle and material removal rate were found to be in the range of 88.66–99.08%, 82.3–98.86% and 82.3–98.86% respectively. Therefore, the developed multi-linear regression models are reliable and effective for predicting output responses, where the percentage errors are at minimum values ranging from –6.59 to 6.71%
2. The results of the ANOVA for R_a , MRR and KTA demonstrate that traverse speed is the most influencing factor, with percentage contributions ranging from 55.67 to 78.94%. Surface roughness and kerf taper angle decrease as waterjet pressure and abrasive mass flow rate increase, resulting in reductions ranging from 2–5% and 2–7%, respectively. Increasing values of traverse speed, waterjet pressure and abrasive mass flow rate lead to increased rates of material removal, ranging from 16–20% and 5–9%, respectively.
3. The multi-objective optimization was performed using RSM for optimising abrasive waterjet contour cutting process parameters applied for 4, 8 and 12 mm material thicknesses, achieving the highest composite desirability values of 0.748448, 0.780587 and 0.786800, respectively. The optimum settings of input parameters i.e., V_f for 4, 8 and 12 mm material thickness are 95, 90 and 91 mm/min, respectively. The obtained optimum settings for m_a and P were found to be the same value for all material thicknesses, at 500 g/min and 200 MPa, respectively. The minimum achieved values of KTA and R_a and maximum MRR for 4, 8 and 12 mm material thickness were 0.799^0 , $1.283\ \mu\text{m}$ and $297.98\ \text{mm}^3/\text{min}$; 1.068^0 , $1.694\ \mu\text{m}$ and $514.97\ \text{mm}^3/\text{min}$; and 1.448^0 , $1.975\ \mu\text{m}$ and $667.07\ \text{mm}^3/\text{min}$, respectively.

Abbreviations and nomenclature

ht	depth of cut (mm)
m_a	abrasive mass flow rate (g/min)
P	water pressure (MPa)
R_a	surface roughness (μm)
V_f	traverse speed (mm/min)
W	kerf width (mm)
W_t	kerf top width (mm)
W_b	kerf bottom width (mm)
t	thickness of the material (mm)
AISI	austenitic stainless steel

ANOVA	analysis of variance
AWJM	abrasive waterjet machining
KTA	kerf taper angle (⁰)
MRR	material removal rate (mm ³ /min)

A. Appendix

Source	R _a 1		R _a 2		R _a 3	
	Contribution %	<i>p</i> -Value	Contribution %	<i>p</i> -Value	Contribution %	<i>p</i> -Value
<i>X</i> ₁	59.90	0.001	69.43	0.000	69.39	0.000
<i>X</i> ₂	5.16	0.067	3.49	0.068	3.77	0.017
<i>X</i> ₃	30.19	0.002	23.86	0.002	24.09	0.001
Error	4.74		3.23		2.74	
Total	100.00		100		100	

Table A1.
ANOVA of *R_a* for t = 4 mm.

Source	R _a 1		R _a 2		R _a 3	
	Contribution %	<i>p</i> -Value	Contribution %	<i>p</i> -Value	Contribution %	<i>p</i> -Value
<i>X</i> ₁	72.21	0.000	71.07	0.000	64.06	0.000
<i>X</i> ₂	7.96	0.007	11.57	0.003	3.94	0.013
<i>X</i> ₃	17.84	0.001	15.52	0.001	30.64	0.001
Error	1.99		1.84		1.36	
Total	100.00		100.00		100.00	

Table A2.
ANOVA of *R_a* for t = 8 mm.

Source	R _a 1		R _a 2		R _a 3	
	Contribution %	<i>p</i> -Value	Contribution %	<i>p</i> -Value	Contribution %	<i>p</i> -Value
<i>X</i> ₁	57.23	0.000	58.85	0.000	57.21	0.001
<i>X</i> ₂	3.44	0.026	5.31	0.002	17.66	0.011
<i>X</i> ₃	34.59	0.000	33.1	0.000	19.47	0.009
Error	4.74		2.74		3.23	3.23
Total	100.00		100.00		100.00	

Table A3.
ANOVA of *R_a* for t = 12 mm.

Source	MRR 1		MRR 2		MRR 3	
	Contribution %	p-Value	Contribution %	p-Value	Contribution %	p-Value
X ₁	71.14	0.000	70.98	0	75.503	0
X ₂	4.35	0.023	2.65	0.067	3.345	0.048
X ₃	22.42	0.002	23.93	0.001	18.688	0.002
Error	2.08		2.44		2.464	
Total	100.00		100.00		100.00	

Table A4.
ANOVA of MRR for t = 4 mm.

Source	MRR 1		MRR 2		MRR 3	
	Contribution %	p-Value	Contribution %	p-Value	Contribution %	p-Value
X ₁	76.69	0.000	76.12	0.000	70.51	0.000
X ₂	7.13	0.002	3.62	0.038	0.12	0.751
X ₃	15.05	0.000	17.98	0.002	24.09	0.005
Error	1.14		2.29		5.27	
Total	100.00		100.00		100.00	

Table A5.
ANOVA of MRR for t = 8 mm.

Source	MRR 1		MRR 2		MRR 3	
	Contribution %	p-Value	Contribution %	p-Value	Contribution %	p-Value
X ₁	77.55	0.000	78.94	0.000	73.29	0.000
X ₂	9.03	0.002	4.13	0.04	4.15	0.028
X ₃	12.11	0.001	13.3	0.001	20.35	0.001
Error	1.31		3.63		2.21	
Total	100.00		100.00		100.00	

Table A6.
ANOVA of MRR for t = 12 mm.

Source	KTA 1		KTA 2		KTA 3	
	Contribution %	p-Value	Contribution %	p-Value	Contribution %	p-Value
X ₁	64.21	0.000	58.7	0.000	56.74	0.000
X ₂	6.75	0.014	6.77	0.017	5.27	0.075
X ₃	26.6	0.001	31.78	0.001	32.74	0.001
Error	2.45		2.74		5.26	
Total	100.00		100.00		100.00	

Table A7.
ANOVA of KTA for t = 4 mm.

Source	KTA 1		KTA 2		KTA 3	
	Contribution %	<i>p</i> -Value	Contribution %	<i>p</i> -Value	Contribution %	<i>p</i> -Value
X_1	59.49	0.001	67.49	0.000	60.95	0.000
X_2	11.84	0.015	5.63	0.013	4.42	0.047
X_3	26.69	0.002	21.65	0.001	31.42	0.001
Error	1.98		5.24		3.21	
Total	100.00		100.00		100.00	

Table A8.
ANOVA of KTA for t = 8 mm.

Source	KTA 1		KTA 2		KTA 3	
	Contribution %	<i>p</i> -Value	Contribution %	<i>p</i> -Value	Contribution %	<i>p</i> -Value
X_1	53.33	0.000	70.59	0.000	55.67	0.000
X_2	12.65	0.055	0.22	0.245	5.24	0.033
X_3	31.40	0.001	25.50	0.000	36.04	0.001
Error	0.63		3.70		3.05	
Total	100.00		100.00		100.00	


Table A9.
ANOVA of KTA for t = 12 mm.

Author details

Jennifer Milaor Llanto, Ana Vafadar and Majid Tolouei-Rad*
School of Engineering, Edith Cowan University, Joondalup, Australia

*Address all correspondence to: m.rad@ecu.edu.au

IntechOpen

© 2022 The Author(s). Licensee IntechOpen. This chapter is distributed under the terms of the Creative Commons Attribution License (<http://creativecommons.org/licenses/by/3.0>), which permits unrestricted use, distribution, and reproduction in any medium, provided the original work is properly cited. 

References

- [1] Radovanović M. Multi-objective optimization of process performances when cutting carbon steel with abrasive water jet. *Tribology in Industry*. 2016;**38**(4):1741-1759
- [2] Liu X et al. Waterjet machining and research developments: A review. *The International Journal of Advanced Manufacturing Technology*. 2019; **102**(5):1257-1335
- [3] Rajurkar K et al. Review of sustainability issues in non-traditional machining processes. *Procedia Manufacturing*. 2017;**7**:714-720
- [4] Natarajan Y et al. Abrasive water jet machining process: A state of art of review. *Journal of Manufacturing Processes*. 2020;**49**:271-322
- [5] Singh P et al. Developments of non-conventional drilling methods—a review. *The International Journal of Advanced Manufacturing Technology*. 2020;**106**(5):2133-2166
- [6] Sureban R, Kulkarni VN, Gaitonde V. Modern optimization techniques for advanced machining processes—a review. *Materials Today: Proceedings*. 2019;**18**:3034-3042
- [7] Rao RV, Rai DP, Balic J. Optimization of abrasive waterjet machining process using multi-objective jaya algorithm. *Materials Today-Proceedings*. 2018;**5**(2): 4930-4938
- [8] Nair A, Kumanan S. Multi-performance optimization of abrasive water jet machining of Inconel 617 using WPCA. *Materials and Manufacturing Processes*. 2017;**32**(6):693-699
- [9] Chakraborty S, Mitra A. Parametric optimization of abrasive water-jet machining processes using grey wolf optimizer. *Materials and Manufacturing Processes*. 2018;**33**(13):1471-1482
- [10] Trivedi P, Dhanawade A, Kumar S. An experimental investigation on cutting performance of abrasive water jet machining of austenite steel (AISI 316L). *Advances in Materials and Processing Technologies*. 2015;**1**(3–4):263-274
- [11] Gnanavelbabu A et al. Experimental investigations on multiple responses in abrasive waterjet machining of Ti-6Al-4V alloy. *Materials Today: Proceedings*. 2018;**5**(5):13413-13421
- [12] Jeykrishnan J et al. Optimization of process parameters in abrasive water jet machining/cutting (AWJM) of nickel alloy using traditional analysis to minimize kerf taper angle. *Materials Today: Proceedings*. 2019;**16**:392-397
- [13] Singh D, Shukla RS. Investigation of kerf characteristics in abrasive water jet machining of inconel 600 using response surface methodology. *Defence Science Journal*. 2020;**70**(3):313-322
- [14] Madankar A et al. Estimation and control of surface quality and traverse speed in abrasive water jet machining of AISI 1030 steel using different work-piece thicknesses by RSM. *Australian Journal of Mechanical Engineering*. 2021; **1**:1-8
- [15] Llanto JM et al. Recent progress trend on abrasive waterjet cutting of metallic materials: A review. *Applied Sciences*. 2021;**11**(8):3344
- [16] Pérez L, Carmelo J. On the application of a design of experiments along with an anfis and a desirability function to model response variables. *Symmetry*. 2021;**13**(5):897

- [17] Luis Pérez C. A proposal of an adaptive neuro-fuzzy inference system for modeling experimental data in manufacturing engineering. *Mathematics*. 2020;**8**(9):1390
- [18] Jiang W et al. Effects of nanostructural hierarchy on the hardness and thermal stability of an austenitic stainless steel. *Journal of Materials Research and Technology*. 2021;**12**: 376-384
- [19] Ramana MV et al. Optimization and influence of process parameters of dissimilar SS304L–SS430 joints produced by Robotic TIG welding. *Materials Today: Proceedings*. 2020;**23**: 479-482
- [20] Doreswamy D et al. Machining of d2 heat treated steel using abrasive water jet: The effect of standoff distance and feed rate on kerf width and surface roughness. *International Journal of Research in Engineering and Technology*. 2014;**3**(8):417-421
- [21] Shibin R et al. Investigation on the abrasive water jet machinability of AA2014 using SiC as abrasive. *Materials Today: Proceedings*. 2020;**21**:519-522
- [22] Radovanovic M, Herghelegiu E. Perpendicularity deviation and surface roughness in abrasive water jet cutting of carbon steel. *Revista de Tehnologii Neconventionale*. 2016;**20**(2):39
- [23] Maneiah D et al. Optimization of machining parameters for surface roughness during abrasive water jet machining of aluminium/magnesium hybrid metal matrix composites. *Materials Today: Proceedings*. 2020;**27**: 1293-1298
- [24] Rajamanickam S et al. Comparative analysis of MRR on abrasive water jet machining parameters over aerospace alloys: Inconel 825 & Ti-6Al-4V. *International Journal of Pure and Applied Mathematics*. 2018;**118**:727-733
- [25] Kaladhar M, Subbaiah KV, Rao CS. Machining of austenitic stainless steels—a review. *International Journal of Machining and Machinability of Materials*. 2012;**12**(1):178-192
- [26] Hlaváč LM et al. Investigation of the taper of kerfs cut in steels by AWJ. *The International Journal of Advanced Manufacturing Technology*. 2015; **77**(9–12):1811-1818
- [27] Pawar PJ, Vidhate US, Khalkar MY. Improving the quality characteristics of abrasive water jet machining of marble material using multi-objective artificial bee colony algorithm. *Journal of Computational Design and Engineering*. 2018;**5**(3):319-328
- [28] Hlaváč LM et al. Shape distortion reduction method for abrasive water jet (AWJ) cutting. *Precision Engineering*. 2018;**53**:194-202
- [29] Aamir M et al. Optimization and modeling of process parameters in multi-hole simultaneous drilling using taguchi method and fuzzy logic approach. *Materials*. 2020;**13**(3):680
- [30] Msomi V, Mabuwa S. Analysis of material positioning towards microstructure of the friction stir processed AA1050/AA6082 dissimilar joint. *Advances in Industrial and Manufacturing Engineering*. 2020;**1**: 100002
- [31] Lin C. Use of the Taguchi method and grey relational analysis to optimize turning operations with multiple performance characteristics. *Materials and Manufacturing Processes*. 2004; **19**(2):209-220

- [32] Aamir M et al. Feasibility of tool configuration and the effect of tool material, and tool geometry in multi-hole simultaneous drilling of Al2024. *The International Journal of Advanced Manufacturing Technology*. 2020;**111**(3): 861-879
- [33] Nagaraj Y et al. Prediction of material removal rate and surface roughness in hot air assisted hybrid machining on soda-lime-silica glass using regression analysis and artificial neural network. *Silicon*. 2020;**13**(11):1-13
- [34] Aydin G, Karakurt I, Hamzacebi C. Artificial neural network and regression models for performance prediction of abrasive waterjet in rock cutting. *The International Journal of Advanced Manufacturing Technology*. 2014;**75**(9–12):1321-1330
- [35] Cetin MH et al. Evaluation of vegetable based cutting fluids with extreme pressure and cutting parameters in turning of AISI 304L by Taguchi method. *Journal of Cleaner Production*. 2011;**19**(17–18):2049-2056
- [36] Llanto JM et al. Analysis and optimization of process parameters in abrasive waterjet contour cutting of AISI 304L. *Metals*. 2021;**11**(9):1362
- [37] Llanto JM et al. Impacts of traverse speed and material thickness on abrasive waterjet contour cutting of austenitic stainless steel AISI 304L. *Applied Sciences*. 2021;**11**(11):4925
- [38] Aamir M et al. Machinability of Al2024, Al6061, and Al5083 alloys using multi-hole simultaneous drilling approach. *Journal of Materials Research and Technology*. 2020;**9**(5):10991-11002
- [39] Koli Y, Yuvaraj N, Aravindan S. Multi-response mathematical model for optimization of process parameters in CMT welding of dissimilar thickness AA6061-T6 and AA6082-T6 alloys using RSM-GRA coupled with PCA. *Advances in Industrial and Manufacturing Engineering*. 2021;**2**:100050
- [40] Kumar KR, Sreebalaji V, Pridhar T. Characterization and optimization of abrasive water jet machining parameters of aluminium/tungsten carbide composites. *Measurement*. 2018;**117**: 57-66
- [41] Chabbi A et al. Predictive modeling and multi-response optimization of technological parameters in turning of polyoxymethylene polymer (POM C) using RSM and desirability function. *Measurement*. 2017;**95**:99-115
- [42] Chate GR et al. Study of the effect of nano-silica particles on resin-bonded moulding sand properties and quality of casting. *Silicon*. 2018;**10**(5):1921-1936
- [43] Javed SA et al. A critical review: Shape optimization of welded plate heat exchangers based on grey correlation theory. *Applied Thermal Engineering*. 2018;**144**:593-599
- [44] Ratner B. The correlation coefficient: Its values range between+ 1/ – 1, or do they? *Journal of Targeting, Measurement and Analysis for Marketing*. 2009;**17**(2):139-142
- [45] Deshpande Y, Andhare A, Sahu NK. Estimation of surface roughness using cutting parameters, force, sound, and vibration in turning of Inconel 718. *Journal of the Brazilian Society of Mechanical Sciences and Engineering*. 2017;**39**(12):5087-5096
- [46] Galpin JS, Hawkins DM. The use of recursive residuals in checking model fit in linear regression. *The American Statistician*. 1984;**38**(2):94-105

[47] Sasikumar K et al. A study on kerf characteristics of hybrid aluminium 7075 metal matrix composites machined using abrasive water jet machining technology. *Proceedings of the Institution of Mechanical Engineers, Part B: Journal of Engineering Manufacture*. 2018;**232**(4): 690-704

[48] Kechagias J, Petropoulos G, Vaxevanidis N. Application of Taguchi design for quality characterization of abrasive water jet machining of TRIP sheet steels. *The International Journal of Advanced Manufacturing Technology*. 2012;**62**(5–8):635-643

[49] Andrzej P. Experimental research into alternative abrasive material for the abrasive water-jet cutting of titanium. *The International Journal of Advanced Manufacturing Technology*. 2018;**97** (1–4):1529-1540

[50] Uthayakumar M et al. Machinability of nickel-based superalloy by abrasive water jet machining. *Materials and Manufacturing Processes*. 2016;**31**(13): 1733-1739

[51] Babu MN, Muthukrishnan N. Exploration on Kerf-angle and surface roughness in abrasive waterjet machining using response surface method. *Journal of The Institution of Engineers (India): Series C*. 2018;**99**(6): 645-656

[52] Ishfaq K et al. Abrasive waterjet cutting of clad material: Kerf taper and MRR analysis. *Materials and Manufacturing Processes*. 2019;**34**(5): 544-553

[53] Kmec J et al. The predictive model of surface texture generated by abrasive water jet for austenitic steels. *Applied Sciences*. 2020;**10**(9):3159

We are IntechOpen, the world's leading publisher of Open Access books Built by scientists, for scientists

6,300

Open access books available

171,000

International authors and editors

190M

Downloads

Our authors are among the

154

Countries delivered to

TOP 1%

most cited scientists

12.2%

Contributors from top 500 universities



WEB OF SCIENCE™

Selection of our books indexed in the Book Citation Index
in Web of Science™ Core Collection (BKCI)

Interested in publishing with us?
Contact book.department@intechopen.com

Numbers displayed above are based on latest data collected.
For more information visit www.intechopen.com



Inkjet Printing of Functional Inks for Smart Products

Cláudia Buga and Júlio C. Viana

Abstract

Inkjet printing is a recent promising technology for direct patterning of solution-based materials over different substrates. It is particularly interesting for applications in the flexible electronics field and smart products manufacturing, as it allows for rapid prototyping, design freedom, and is compatible with conductive, semiconductive, and dielectric inks that can be cured at low temperatures over several types of substrates. Moreover, the inkjet process allows for ink economization, since great electrical conductivity can be achieved despite the deposition of small volumes of ink. This chapter describes the overall process, the main inks and their features, the critical process variables, and its limitations. Applications related to inkjet printing of functional materials and smart products are highlighted. New technology advancements and trends are finally addressed.

Keywords: inkjet printing, functional inks, process parameters, printing process optimization, inkjet printed devices, smart products

1. Introduction

Inkjet printing (IJP) is a widespread technology used in personal and industrial printers. Recently, it has started to gain traction as a new promising technology for the direct patterning of solution-based functional materials. IJP relies on a non-impact dot-matrix printing technology in which droplets of ink are flown from small openings, called nozzles, directly to a designated position on a media to produce an image. The printed patterns are digitally defined and directly transferred to the printer. The nozzles or the substrate holder move accordingly to a pre-programmed pattern, which allows the printing of virtually any pattern [1, 2].

IJP technique is particularly interesting for applications in the printed electronics field as it allows for rapid prototyping and is compatible with various substrates, and conductive, semiconductive, and dielectric inks that can be cured at low temperatures. As a result, several application examples of this technology have already been advanced in the literature [3–9]. IJP methods are widely employed in the manufacture of sensors and actuators, and many electrically conductive inks are already commercially available and optimized according to specific characteristics that make them suitable for IJP [10]. Since IJP relies on the use of computer software, it allows for rapid prototyping and freedom of design combined with tunable resolution [11]. Throughout the literature,

some examples include IJP temperature sensors [12–14], humidity sensors [15–17], and pressure and strain sensors, that can be capacitive [18, 19], piezoresistive [20, 21], and piezoelectric [22–24]. These sensors and actuators can be integrated into novel smart products.

According to recent technical reports, printed electronics (PE), particularly IJP and its enabling technologies (functional printing and inks) show an increased market interest and growth. **Table 1** presents the market expectations related to these technologies.

PE market will continue to expand over the coming years, with a strong emphasis on energy harvesting and storage for electronic cars, gadgets, equipment, components, and other industries that rely on PE to reduce total energy usage. The PE market will be driven by low production costs, environmentally friendly technologies, a diverse choice of substrates, and a rising demand for flexible electronics applications. PE has allowed printing of electronic and electrical components on lightweight, cost-efficient and flexible materials (like cloth, paper, or polymeric films) in conventional electrical circuits. This PE market will continue to expand mainly driven by [29]: (a) the increasing development of smart and connected devices, as demanded by Internet of Things (IoT); (b) the rising demand for energy-effective, thin, and flexible consumer electronics; (c) the substantial costs reduction provided by PE; and (d) the importance of environmentally sustainable technologies.

The increased demand for low-cost and high-volume production of electronics will boost the functional printing market. This is supported by the increased availability of a wide range of substrates, high-throughput manufacturing technologies (e.g., R2R for large-area electronics processing), and a reduced environmental impact (e.g., thin and flexible electronics) [30]. This will be fostered by the development of new products/applications, the introduction of added functionalities into multiple products, and the emergent widespread of digital manufacturing techniques.

After a huge pace of growth, the IJP market is becoming mature, and high-speed inkjet printing devices with enhanced quality and higher productivity are already available. Notwithstanding, the initial costs of equipment are still rather high. Major applications of IJP have been related to graphic communication and packaging labeling, but functional substrates and objects driven by PE and functional printing applications are fostering IJP market. Principal drivers for the adoption of IJP technologies

	Printed electronics [25]	Functional printing [26]	Inkjet Printing [27]	Functional inks [28]
2020 market value, B\$	79	8.9	40.8	0.87
2027 market value, B\$	22.7	23.9	49.2	1.3
CAGR, %	21.5	15.1	3.11	5.3
Typical applications	Batteries, sensors, sign boards, labels, PCB, touch panels, LED panels, solar cells	Sensors, displays, batteries, RFID tags, lighting, photovoltaic, electronic components	Flexible OLED displays, wearables, photovoltaic, sensors, PCB	PCB, MEMS, security printing, smart textiles, displays, smart packaging, RFID tags, photovoltaics, biochips

Table 1. Market values and growth rates for different related technologies: Printed electronics, functional printing, inkjet printing, functional inks, and smart products.

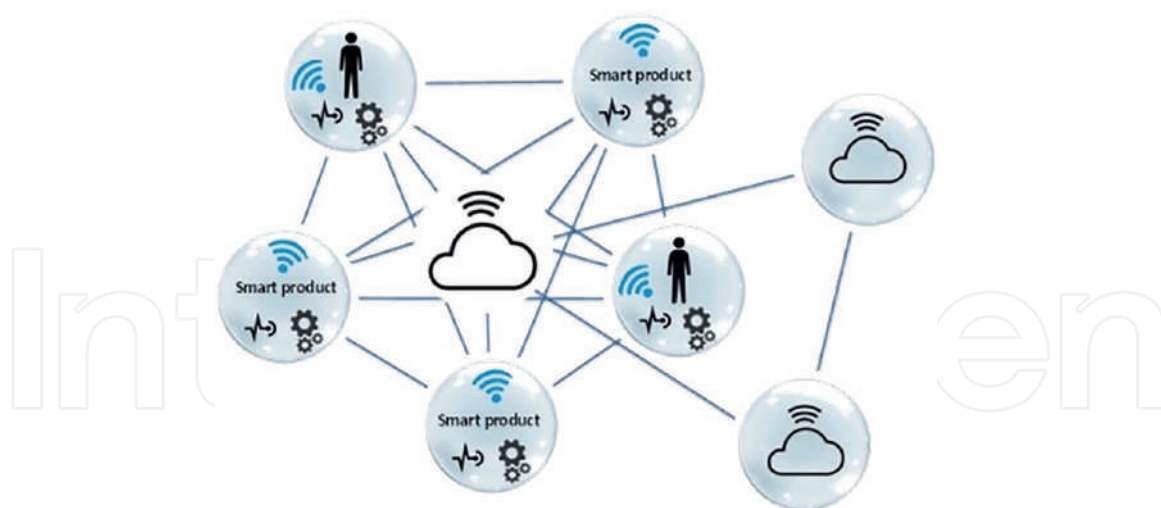


Figure 1.
System of smart products.

are OLED displays, products/processes digitalization, IoT, Cyber-physical systems (CPS), and Big Data.

Functional inks can be electrically conductive, resistive, dielectric, semi-conductive, or have other special functions, such as thermal conductivity, electroluminescence, light-diffusing, or piezoelectric. Functional inks are key enablers for PE applications. They must combine their functionality with being flexible, processable at low temperature, adhere to a wide range of substrates, in some cases transparent, and straightforward to manufacture. Novel functional inks include suspensions of organic or inorganic nanomaterials, or particle-free solutions of organic materials, which are inherently stretchable, and suitable for applications in e-textiles and in-mold electronics [31].

Smart products are physical objects equipped with sensors, embedded artificial intelligence, communication ability, and information technology. They bridge the physical and digital worlds, sharing information about themselves, their environment, and their use, being supported by emergent technologies of CPS, IoT, and artificial intelligence (AI). Furthermore, smart products are now connected and able of forming product eco-systems; they interact with the user, adding a social layer to these eco-systems. This allows a paradigm shift in the business world: from selling products to offering services, to the “servitization” of products (**Figure 1**). This transformation towards novel smart products is enabled by the development of emergent technologies simultaneously in both the physical (hardware) and digital (software) worlds, and their interfaces. This chapter focuses attention on product manufacturing (hardware) technologies for smart products, namely those based on PE and functional printing, and more specifically on inkjet printing of functional inks.

2. Inkjet printing of functional inks

2.1 Inkjet printing process

IPJ is an additive manufacturing technique that encompasses an ink reservoir that is connected to a print head device and responsible for jetting ink droplets over a pre-determined substrate. IJP allows for high-resolution 2D patterning, ink

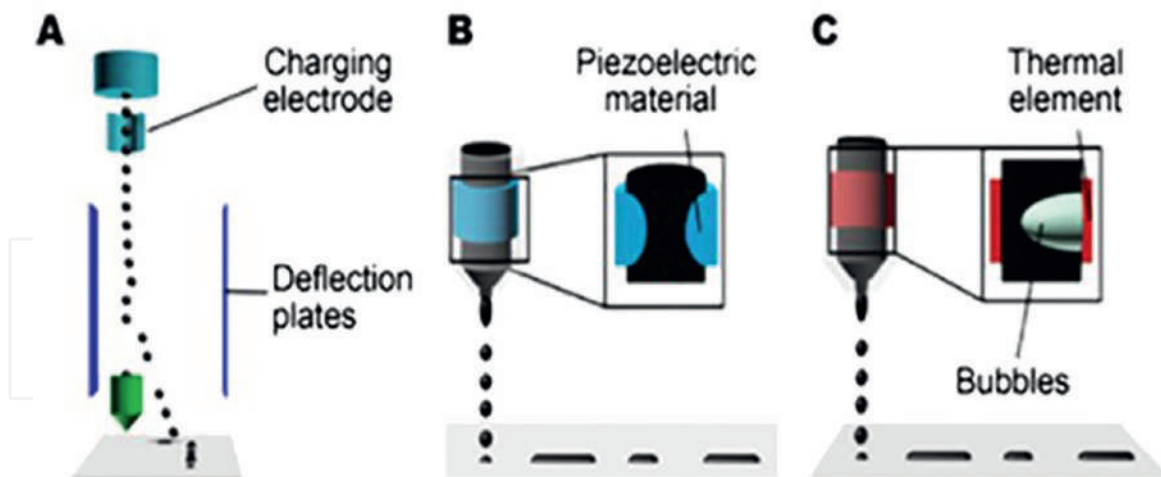


Figure 2.
IJP methods: (a) CIJ, and DOD inkjet printing with (b) piezoelectric and (c) thermal head [34].

economization, and non-contact deposition via a micrometer-sized inkjet nozzle head [32, 33]. Inkjet can be divided into two main distinct processes (**Figure 2**): Continuous inkjet (CIJ) printing and Drop-on-demand (DoD) printing technologies [35]. As the name suggests, in CIJ printing the droplets are continuously generated and deposited when subjected to an electrostatic field, caused by a charging electrode. DoD printing, on the other hand, relies on the selective activation of the print-head through impulses that can be acoustic, electrostatic, thermal, and piezoelectric (the latter two are the most reported cases) [35].

The CIJ process is mainly used in industrial printers, mostly for packaging and graphical applications. In this case, the ink droplets are continuously expelled due to the effect of an electric field that actuates the piezoelectric crystal of the print-head. Although this process can be used for PE it is majorly directed at continuously printing large volumes of nonfunctional inks [36]. Concerning DoD inkjet printing, several sub-methods can be identified. The most disseminated ones are piezoelectric and thermal inkjet printing, nonetheless, there are other methods whose popularity is increasing and can also grant high-quality printing of functional inks [36]. Among those, electrohydrodynamic (EHD)-IJP [37–39], aerosol jet printing [40], drop impact printing [41], and acoustic printing [42], can be highlighted.

In the piezoelectric IJP method, the ink reservoir is coupled with piezoelectric constrictors that load and expel the ink (print head). In this process, the dimensions of the ink droplet can be controlled, so the ink consumption is very low. To avoid clogging the nozzles, the functional inks must be produced taking into account specific properties, such as particle size, ink viscosity, surface tension, and density [35]. The nozzle is designed to be resistant to organic solvents and is therefore compatible with a wide range of solvents for ink formulation [2]. **Table 2** summarizes the main characteristics of the inks that are compatible with each one of the inkjet printing methods and sub-methods. Comparing the different printing sub-methods, it is clear that the thermal and the piezoelectric ones are much more limited in terms of suitable ink viscosity range. Nonetheless, they are still currently the most approachable methods in terms of affordability and widespread commercial availability of the equipment.

Except for the jetting method, the overall process of printing is common to all CIJ and DoD IJP techniques. The printed patterns are digitally generated (CAD software)

Printing Method	Sub-method	Particle size (nm)	Viscosity (cP)	Surface Tension (dynes/cm)	Resolution (μm)
CIJ	—	<1000	1–10	25–70	
DoD	Thermal	<1000	5–30	35–70	2–100
	Piezoelectric	<300	1–30	35–70	2–100
	EHD	3–300	1–4000	35–70	0.2–1
	Aerosol	10–30	0.5–2500	20–70	5–20
	Acoustic	<100	0.5–25,000	15–650	10–20
	Drop impact	<20,000	0.5–33	32–70	40–960

Table 2.
CIJ and DoD printing characteristics [2, 35, 37–43].

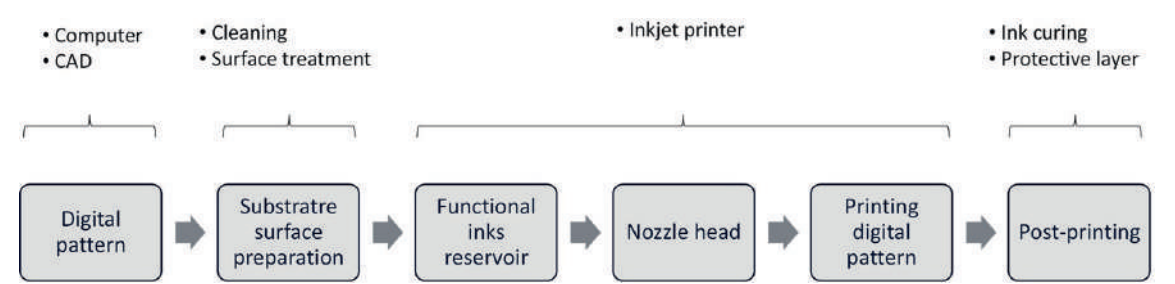


Figure 3.
Inkjet printing steps.

and can be easily changed, which makes this printing technique an ideal choice for prototyping and design optimization. **Figure 3** depicts the main stages in IJP:

1. Digital pattern—A CAD software (or other graphic software) is used to digitally generate the printed pattern.
2. Substrate surface preparation—the substrate surface is cleaned with an appropriate cleaning agent; a surface treatment can be selected for better ink adhesion.
3. Ink preparation—ink can be filtered to remove impurities; ink viscosity can be changed by using an adequate solvent; a surface treatment technique can be applied (e.g., plasma, corona discharge); the ink must be stirred for better particle suspension dispersion.
4. Inkjet printing—the file is uploaded in the printer software; the reservoir is filled with the ink; the ink can be preheated before printing; the printing parameters are defined, mainly for controlling the printing head (see next section); then, printing takes place.
5. Post printing—after printing the printed pattern must be sintered/cured (by temperature, photonic, UV light, plasma); a protective layer can be applied (e.g., by lamination, spray coating)

The IJP technology for PE applications and its technical-scientific developments have been reviewed over the last decades. Hue P. Le [44], 1999, reported the

developments in the various IJP technologies, noting the significant growth rate of inkjet printers market. New ink formulations and new printhead designs were recognized as relevant for new applications. In 2010, the state-of-the-art of IJP of functional materials was reviewed by Raje and Murmu [45]. Improvements in process throughput remained the major challenge. In the same year, Derby reviewed the current understanding of the mechanisms of drop formation and the interactions between drops and the substrate, with a focus on the fabrication of structures for structural or functional materials applications [46]. Two years later, in 2012, Cummins and Desmulliez conducted a review in IJP of conductive materials [47]. IJP process, substrate properties, and types of conductive inks are the various factors that affect the quality of inkjet-printed products and their increasing relevance to the fields of electronics manufacturing, packaging, and assembly. In 2019, Nayak et al. reviewed the IJP of electronic devices, mainly addressing the fluid dynamics of inks and main properties (e.g., viscosity, surface tension, Weber number, Reynolds number, and Ohnesorge number) and their effects on defects appearance (coffee ring formation) [48]. The use of functional inks in sensors, thin-film transistors, and energy storage devices is presented. Ke Yan et al. revised the state-of-the-art related IJP strategies and functional inks for wearable electronic devices (e.g., sensors, displays, transistors, and energy storage devices) [49]. They highlighted the need of having available more intrinsically flexible and stretchable inks for avoiding, cracking, and delamination on highly flexible/stretchable substrates. Also, IJP technology development shall solve nozzle clogging issues for a more stable printing process. Kye-Si Kwon et al. reviewed piezo-driven IJP for PE. Other printing methods for high viscosity ink are also considered and compared (e.g., electrohydrodynamic jet, aerosol jet, and micro-plotter printing) [50]. There is a high demand for high-resolution printing of high viscosity inks for PE. In this case, the functionality of the device is more important than graphism perception, and the development of suitable inks for IJP remains one of the key issues. More recently, Muhammad Ali Shah reviewed the classifications and applications (textile, displays, and wearable devices) of IJP with more attention paid to piezoelectric IJP due to its higher relevance [36]. Various driving-voltage waveforms approaches are compared. Recently published studies on applications of IJP are summarized. Again, high high-viscosity IJP technologies are revised. The performance of IJP shall be improved by the development of new printheads with ink-recirculation and new techniques for printing high viscosity inks.

2.2 Functional inks for IJP

The use of inks has been around for almost as long as there is human life. It empowered evolution and was responsible for cultural and sociological developments whose footprints can be traced from the Paleolithic to this day [51]. The methods to dispense inks have also evolved with them and the first inkjet-type apparatus was patented in 1858 by William Thomson and Abbe Nollet [52]. The concept of printing functional conductive inks emerged some years later, in the 20th century, and was patented by Albert Hanson [53]. Nonetheless, research in IJP of functional inks exploded only nearly 100 years later, at the turn of the 21st century, thanks to the breakthrough development of organic conducting polymers by Heeger, MacDiarmid, and Shirakawa, which rendered them the 2000 Chemistry Nobel Prize [54, 55]. This led to several advancements in the field of PE, including the development of the first high-resolution printed all-polymer transistor circuits [56–58]. The fact that polymeric inks are more stable, easier to formulate, manipulate, and print was mostly responsible for

this paradigm shift [43]. Nonetheless, with the technical developments experienced in this field, metallic-based inks started to be printed shortly after, thanks to the use of stable solvent systems and other additives that allowed to stabilize the metallic particles into homogeneously dispersed formulations with tunable surface tension and viscosity. Thereby, nowadays several base materials can be selected, depending on the final device desired functionality.

Functional inks for inkjet printing can be divided into, conductive, semi-conductive, and dielectric. Conductive inks are usually applied in the development of conductive tracks, vias, and electrodes. They generally rely on the dispersion of metallic nanoparticles, namely Ag [59], Cu [60], and Au [61], on organic or water-based solvents. To aid in the dispersion and grant long-term stability of these inks, surfactants, stabilizers, humectants, and other additive compounds are demanded [32]. To further tune the ink properties conductive nanofillers such as CNT can also be added. Although less conductive than metals, some polymers, metal-oxides, liquid-metal alloys, MXenes, perovskites, quantum-dots, and metal-organic-decomposition inks can also be used in the development of conductive inks. Currently, indium tin oxide (ITO) is still the most used material to produce transparent electrodes for thin-film devices (organic light-emitting diodes, OLED; field-effect transistors, OFET; photovoltaic devices, OPV) [62, 63]. However, the deposition of ITO is usually done by resorting to physical vapor deposition (PVD) which is much more expensive and energy-demanding than printing technologies. Moreover, its over-exploitation is damaging to the environment, and it is only recyclable through energy-consuming processes [64]. MXenes, quantum dots, and perovskites are examples of alternative base materials that can be used to develop inks for inkjet printing transparent electrodes for the above-mentioned applications. As a result, even though they have lower power conversion efficiency, their popularity is increasing [65, 66]. Despite being known for their higher electrical conductivity most inorganic inks are expensive, become brittle after curing, have limited flexibility, and might experience oxidation and loss of performance, if not properly encapsulated. As a result, organic conductive polymers such as poly(3, 4-ethylenedioxythiophene)-poly(styrenesulfonate) (PEDOT:PSS) [10, 67, 68], poly(3-hexylthiophene-2,5-diyl) (P3HT) [69, 70], and oxidized polyaniline (PANI) [71] are also being used as alternative materials for printing electrodes and conductive tracks. Other highly conductive inks can be developed using carbon allotropes, such as single-walled and multi-walled carbon nanotubes (SWCNT and MWCNT) [72–76], graphene [77, 78], and fullerenes [79].

Semiconductors have an electrical conductivity that can vary between the conductor and the dielectric. They can be n-type or p-type, depending on the doping atomic impurities added to the structure of the semiconductor. These impurities define the electrical properties, with highly doped semiconductors presenting conductivity values similar to metals. When the semiconducting material is less doped, its conductivity departs further from the conductive range. These semiconductors are crucial for the performance of the final device since their characteristics usually change with environmental physical, or chemical conditions [43, 72]. Less doped inorganic semiconductors include zinc-oxide (ZnO), zinc tin oxide (ZTO), and indium-zinc-oxide (IZO). Another interesting material for the development of semiconductor inkjet inks is the amorphous indium-gallium-zinc-oxide (a-IGZO), as it is processable at low temperatures, being vastly used in thin-film-transistors and solar cells [80]. On the other hand, organic semiconductors can be PEDOT:PSS, rubrene, pentacene, poly(diketopyrrolopyrrole-terthiophene) (PDPP3T), diphenylanthracene (DPA) [43]. PEDOT:PSS and CNT-based composites are vastly

Ink	Description	Examples
Conductive	Composed of highly conductive materials, mostly metals, metal-based composites, metal oxides, metallic alloys, highly doped conductive organic polymers in solvents, metal-oxide particles suspended in binders or organic-metallic blends	Metallic nanoparticle-based inks; Conductive polymers; Graphene inks; Perovskites; Mxenes; Quantum dots; Metal oxide-based inks; Eutectic liquid metals
Semi-conductive	Composed of semiconducting organic polymers in solvents, inorganic nanoparticles (Group III-V, II-VI and IV semiconductors and carbon nanotubes) suspended in carrier fluids, or organic-inorganic blends; Also composed of less doped polymers that can be reinforced with carbon nanotubes or wires.	Metal-oxide inks; Semi-conductive polymers; Carbon-based inks
Dielectric	Organic polymers in solvents, organic polymer thermosets or ceramic-filled organic polymers	Ceramics; Metal-organic materials; Dielectric polymers; Piezoelectric polymers

Table 3.
Summary of ink types, their description, and some examples.

used as pressure sensors (piezorresistive materials) [81, 82], and temperature sensors (thermoresistive materials) [83, 84].

Finally, dielectrics exist in the less conductive boundary of the conductivity spectrum. They are used in electrical applications that demand high capacitance and insulation. Some dielectrics inks can be made from metal-organic materials such as aluminum oxide (Al_2O_3), zirconium oxide (ZrO_2), hafnium oxide (HfO_2), and yttrium oxide (YO_2). Nevertheless, organic dielectric inks can also be formulated from polyvinylpyrrolidone (PVP), Polyvinyl alcohol (PVA), and Polymethyl methacrylate (PMMA), polydimethylsiloxane (PDMS), Polyvinylidene fluoride (PVDF) and its copolymer, polyvinylidene fluoride-trifluoroethylene (PVDF-TrFE). PVDF-based inks are of extreme importance since they are ferroelectric and enable piezoelectric applications. Another inkjet ink is the electrostrictive P(VDF-TrFE-CTFE) terpolymer, which can be used for energy harvesting applications [85–87]. **Table 3** summarizes the different types of printable inks.

2.3 Inkjet printing process variables

Both CIJ and DoD printing demand the use of inks with particle size under $1\text{ }\mu\text{m}$ (ideally $<300\text{ nm}$). In the particular case of the piezoelectric DoD method, their viscosity should be in the range of 1-20 cP, and their surface tension between 35 and 70 mN.m^{-1} [35]. IJP requires no mask, has a low ink waste rate, and typical linewidth resolution of 30-50 μm [88]. DoD has established itself as the main IJP technology, with piezoelectric method being the most widely employed when it comes to IJP printing of functional inks, as it allows less ink consumption [49]. Hence, inks are specifically formulated to meet the requirements of the printing process [49].

To achieve the best possible printing quality, several factors need to be taken into account and studied from an optimization-driven perspective. For instance, the rheological properties of the ink (viscosity, surface tension, and density) interplay with each other and cannot be individually assessed. Similarly, the parameters of the printing process themselves cannot be individually studied. Thus, the printing resolution, printhead speed, printhead height, waveform profile, droplet size, and printhead temperature also influence one another and, as a result, before high-quality printing

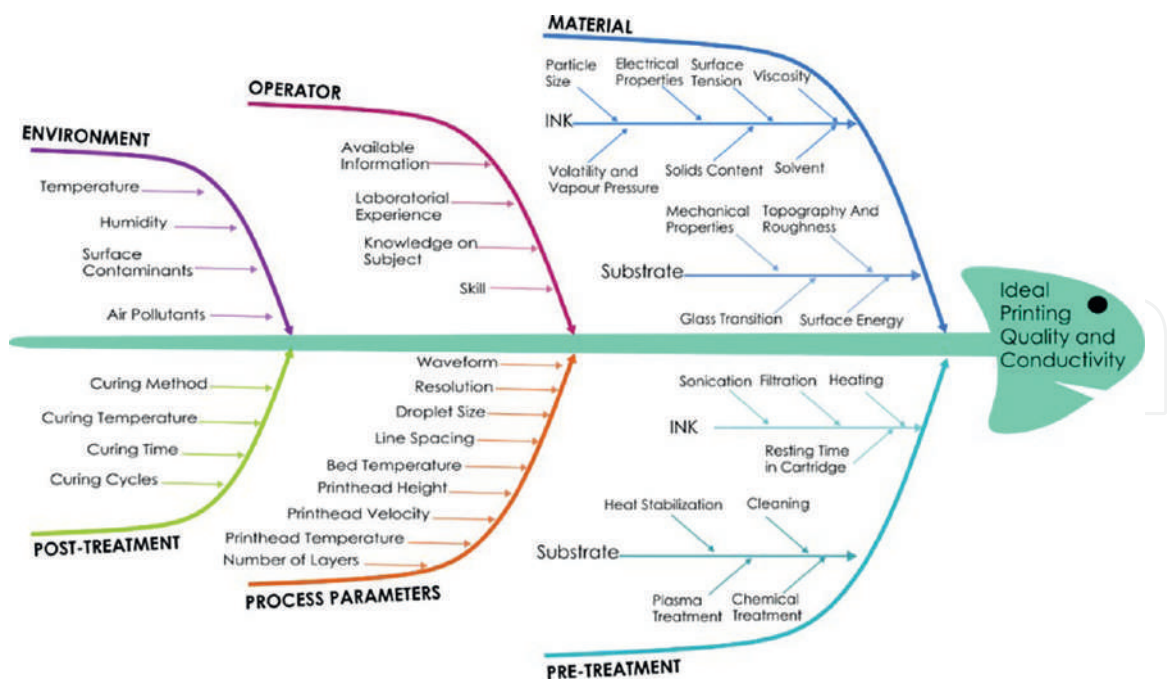


Figure 4.
Potential cause-effect factors influencing printing quality and conductivity.

can be attained, a series of optimization studies need to be conducted for each combination of ink/substrate. Other variables include the pre and post-treatment of the ink, substrate, and printed outputs. The operator experience and the environmental conditions will ultimately also influence the printing process. In **Figure 4**, the main print quality affecting parameters are summarized in a Fishbone diagram. Since several factors need to be simultaneously studied, a design of experiments approach is frequently performed by researchers aiming to rapidly optimize the process [59, 89–91].

Even after all parameters are optimized, some issues can still occur during the printing process namely nozzle clogging, printing deficiencies (coffee-ring effect, satellite drops, random electrical interference that causes droplet jetting oddness, missing droplets), loss of ink dispersibility, presence of dirt or dust particles in the ink system or substrate, among other issues [92]. As a result, to use IJP to develop electronic devices in industrial settings in-line quality control methods should be performed as a way of assuring functionality. To prevent the effect of environmental variables, which are often uncontrollable, the printing process should be performed in a controlled clean-room area.

2.3.1 Inks properties

Inks intended for inkjet printing should have linear Newtonian behavior and low viscosity, within a specific range. The drop formation and dynamics of the ink are ruled by three dimensionless numbers, that are related to the ink rheological and physical properties, namely the Reynolds number (R_e), the Weber number (W_e), and the Ohnesorge number (Oh) [49]:

$$R_e = \frac{\nu \rho d}{\zeta}; W_e = \frac{\tilde{\sigma}^2 \rho d}{\tilde{a}}; Oh = \frac{\sqrt{W_e}}{R_e} = \frac{\zeta}{\sqrt{\gamma \rho d}}; Z = \frac{1}{Oh} \quad (1)$$

where, v is the velocity, ρ is the density, η is the dynamic viscosity, γ the surface tension, and d the characteristic length. To assure the ink is printable, its characteristics must obey some critical parameters and fall within certain limits. Most reports indicate that the optimum range to print a stable droplet is $1 < Z < 10$, as represented in **Figure 5** [49]. Z values above 10 relate to fluids with insufficient energy for drop formation, whereas Z values below 1 generally belong to fluids that are too viscous for printing, because the capillary force at the nozzle prevents its ejection. Also, to avoid the formation of satellite drops, the Weber number should be in the range of $2 < We < 25$. Nonetheless, these boundaries are not universal laws, with some authors reporting slightly broader ranges for ink printability [93, 94]. When the overall properties of the ink do not fall within these boundaries, the jetted fluid will not be able to form stable and consistent drops with adequate velocity to overcome the surface tension barrier at the tip of the nozzle, caused by the fluid/air interface. In this case, several break-up regimes can be identified from the Rayleigh break-up (insufficient velocity to form jets of ink) to the complete atomization (disintegration of the ink jets due to exaggerated velocity) [95].

2.3.2 Adhesion between inks and substrates

Another parameter that demands the previous study when planning inkjet printing is the adhesion between ink and substrate. This may affect the final printing result and additional procedures might be needed to assure compatibility. For ink to adhere well to a substrate, it must present appropriate wettability and adhesive bondability [96], meaning the surface tension of the ink must be lower than the wetting tension of the substrate (surface energy). To test this parameter, the substrate must be completely dry and free of any contaminants to start with. If after cleaning the substrate it still presents low wettability, surface pre-treatments may be needed. Such treatments include surface modification resorting to chemical modification,

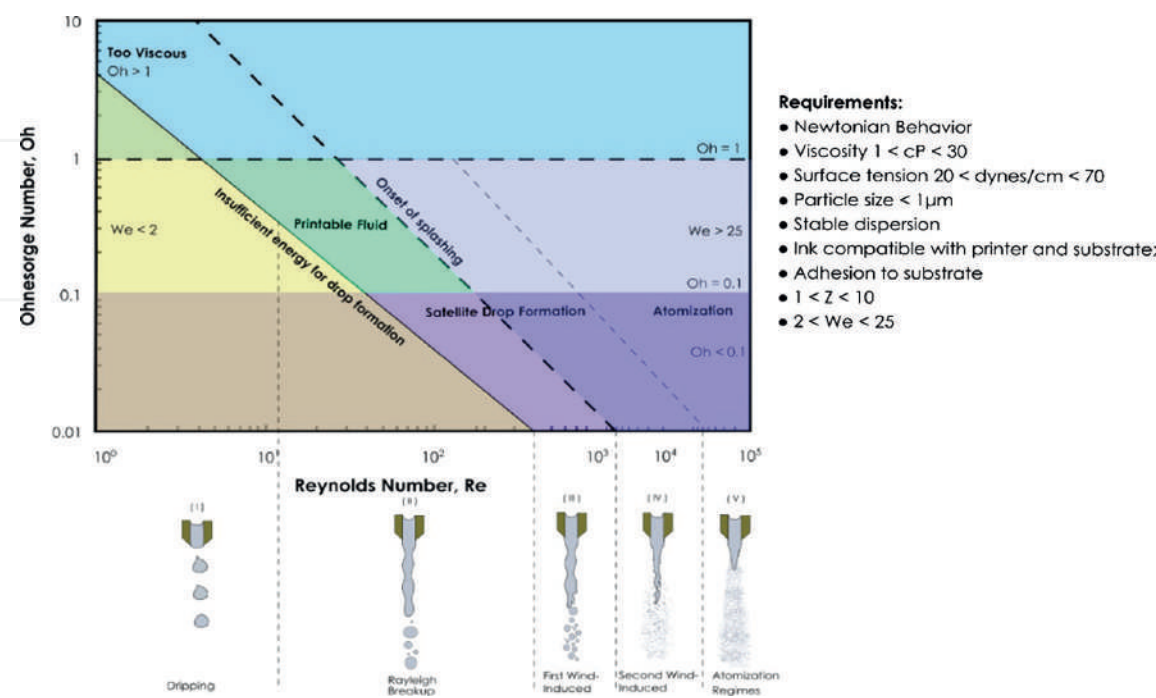


Figure 5. Ohnesorge diagram, evidencing the fundamental characteristics of the printable fluid and the different drop break-up regimes responsible for printing errors, and requirements summary for developing a printable fluid.

coating with hydrophilic moieties (such as PVP and PVA solutions) [97, 98], plasma activation [98–100], mechanical abrasion, or superficial integration of nanoparticles or nanoclays [101], which increase surface roughness. Plasma activation is usually done by resorting to corona discharge plasma treatment and relies on the production of a high voltage electrical discharge that ionizes the molecules of the treated surface, positively changing its polarity (or oxidizing it) [99, 102, 103].

2.3.3 Pre- and post-treatments

To improve the printability of the ink some actions can be taken. Re-dispersion followed by filtration of the ink before use is effective in removing impurities and potential particle agglomerates that could clog the microscopic nozzles. The presence of trapped air bubbles in the ink is also damaging to the printing process. To prevent trapped bubbles, the ink should be degassed after filtering and left to rest for at least 30 minutes after filling the cartridge with it.

After printing, the ink must dry to become functional. When printing over paper and textiles, the ink is easily absorbed, and drying is not usually necessary, however, when using polymeric substrates it is preferable to promote the drying of the ink by thermal or UV curing [104]. In the case of thermal curing, heat is applied to facilitate the evaporation of the liquid ink carrier, which can be water or organic solvent. To render high printing quality and good electrical conductivity the curing temperature needs to be carefully chosen to prevent deformation, melting, or degradation of the substrate, as well as preserve the ink properties and avoid cracking [89]. To assure the homogeneous heating of the final printed patterns, an oven or an environmental chamber is usually used. Alternatively, cross-linkable inks are instantaneously cured using UV irradiation.

Regarding the drying of the ink itself, residual tensions might cause the ink not to dry homogeneously, leading to a phenomenon known as the coffee ring effect, which impairs the quality of the final print and is pictured in **Figure 6**. The coffee ring effect

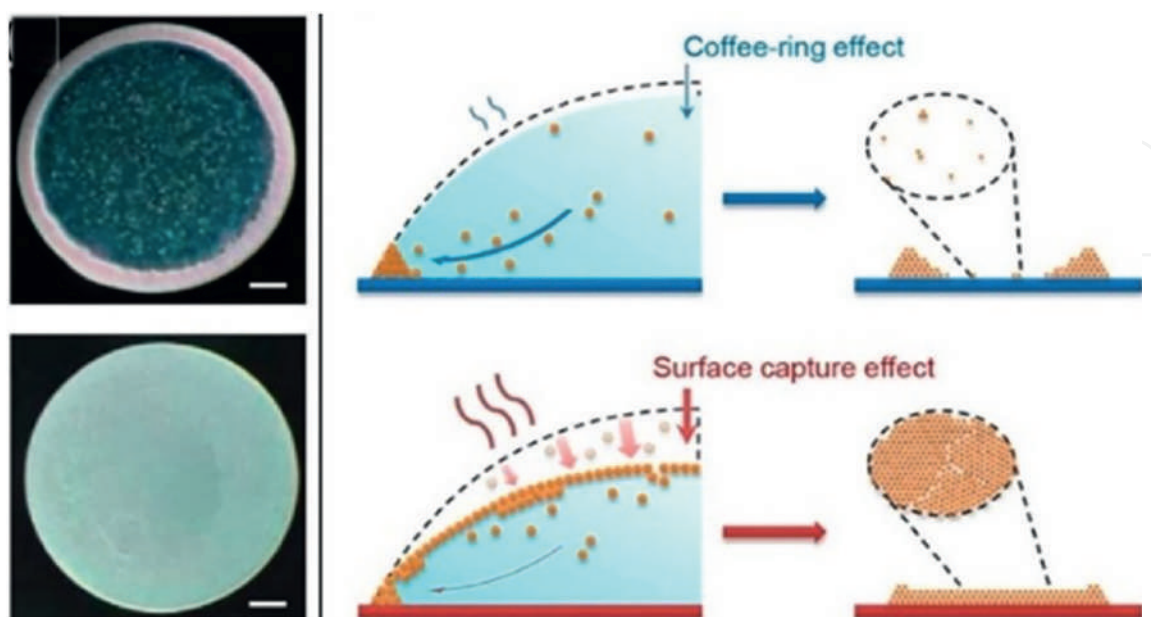


Figure 6.
 Ring formation in colloidal droplets dried at room temperature versus uniform particle deposition of evaporating the same colloidal system in an environmental chamber at an elevated temperature. Reproduced with permission from refs. [105, 106]. Copyright © 2019 ACS.

is characterized by a ring-like morphology formed during ink evaporation, resulting from the solute segregation and accumulation along the drop periphery due to capillary flow. This issue occurs frequently when using nanoparticle inks and is caused by the convective macroscopic flow (Marangoni flow) that occurs during the drying process and pushes the particles to the borders of the printed fluid [107], causing irregularities in thickness or coalescence between printed droplets.

Factors that influence the coffee ring effect are the evaporation rate and the particle concentration in the ink. A lower evaporation rate promotes ink homogeneity and can be reduced by lowering substrate temperature. Thus, the drying temperature and time also need to be optimized. Moreover, superficial cleaning, treatment, and heating must be performed homogeneously throughout the entire surface of interest. Since the ink starts its drying process as soon as it hits the substrate, the final curing step in the oven might not be sufficient to grant homogeneous drying. As a result, some printers encompass an integrated substrate heating feature, which can facilitate the bonding of the ink to the substrate and in between layers (when more than one layer of ink is printed). Using a solvent with a high boiling point, adding additives, reducing drop volume, and increasing the particle diameter can also help reduce the coffee ring effect.

2.3.4 Process and apparatus related parameters

Printhead model. Different inkjet printing systems demand different printhead models. The model of printhead also varies depending on the final application. Printheads for industrial IJP applications are more expensive, display a larger number of nozzles and allow for higher printing resolution. On the other hand, printheads intended for research and laboratory use are cheaper, have fewer nozzles, and print in lower resolution, as displayed in **Table 4** [50]. Regarding laboratory printing setups the most frequently used thorough the literature is the Dimatix Materials Printer, DMP series [50, 92, 108–112].

The general inkjet printer setup can be seen in **Figure 7a**. A 3-degree of freedom (DOF) system is the most frequently adopted and allows for efficient printing. Usually, the printhead only prints in one of the directions x-y directions (left-to-right).

In an inkjet printer the following parameters can be adjusted:

Resolution. The resolution should be chosen in accordance with the desired printed pattern, selected ink, and substrate material [109]. In multi-nozzle inkjet printers, the resolution is often controlled by the rotation of the printhead in predefined angles

System Type	Examples	Features				
		Max. Jetting Frequency (kHz)	Print Width (mm)	Droplet Volume (pL)	Resolution (dpi)	Number of nozzles
Printheads for industrial applications	Xaar, Hitachi Ricoh, Konica Minolta, Kyocera	45–100	72–116	1.5–21	360–400	1024–5680
Laboratory and research systems	Microdrop, Microfab, Fujifilm Dimatix	30	64.96	12–33	1200	1024

Table 4.
Available inkjet printing systems [34, 50].

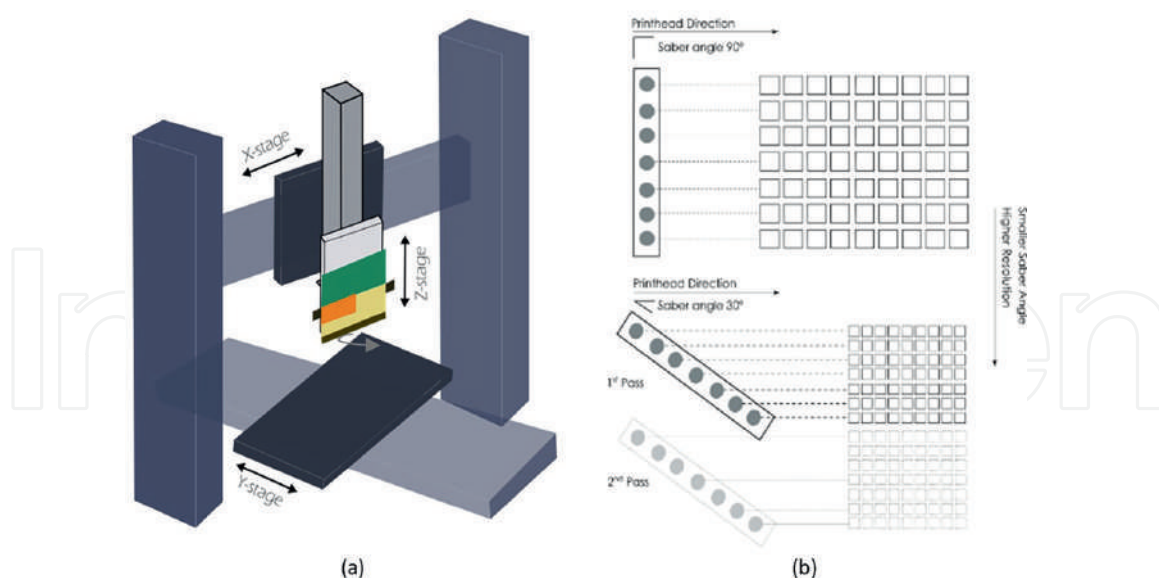


Figure 7.
 (a) Illustration of the XYZ cartesian inkjet printing system with mounted printhead. (b) Depiction of the Printhead in its native position and rotated at a 30-degree angle [113].

(saber angles). To increase resolution, the printhead is rotated towards the movement direction axis. While the printhead is perpendicular to the printing direction, the resolution equals the native distance of the nozzles (lowest resolution). When the angular displacement is decreased, the distance between nozzles is diminished and the printed patterns achieve higher resolution (**Figure 7b**) [113]. In cases where the printhead is manually rotated, operator errors may occur, especially when dealing with small patterns with high resolution, which are more prone to displacement errors. For example, as seen in **Figure 7b**, many patterns demand more than one pass of the printhead be concluded and, if the direction is not perfectly aligned, the pattern will experience displacement between the two passes.

In practice, higher resolution is associated with a higher density of drops per area, which in turn, provides higher conductivity when printing conductive inks. Nonetheless, some issues might arise when the drops are too distanced (low resolution) or too overlapped (high resolution) and printing errors such as flooding, lack of superficial homogeneity, and loss of conductivity can occur, as illustrated in **Figure 8**. Moreover, if several passes are demanded additional attention must be given to assure correct angle alignment [109]. Some designs can also be prone to variability and errors, particularly if the image has sharp right-angle corners or lines whose width does not obey critical spacing rules [108].

Since inkjet printers usually print exclusively when moving in the left–right direction, different orientations of the same patterns may experience differences in the quality output, especially when higher resolutions are involved ($>$ native resolution). This is particularly noticeable if the manual setting of the saber angle is not perfectly aligned. Considering this, to print the correct resolution in the precise position, the inkjet printer software is programmed to compensate for the angular displacement of the head. When this happens, even a slight imprecision during the printhead assembly can propagate printing errors across several printing passes (In **Table 5**, the major figures of merit that allow to identify the quality of printing are summarized, along with their description and observational examples).

Printhead Height. The height of the printhead, i.e., the distance between the nozzle and the substrate (the stand-off distance) can influence the splatter pattern

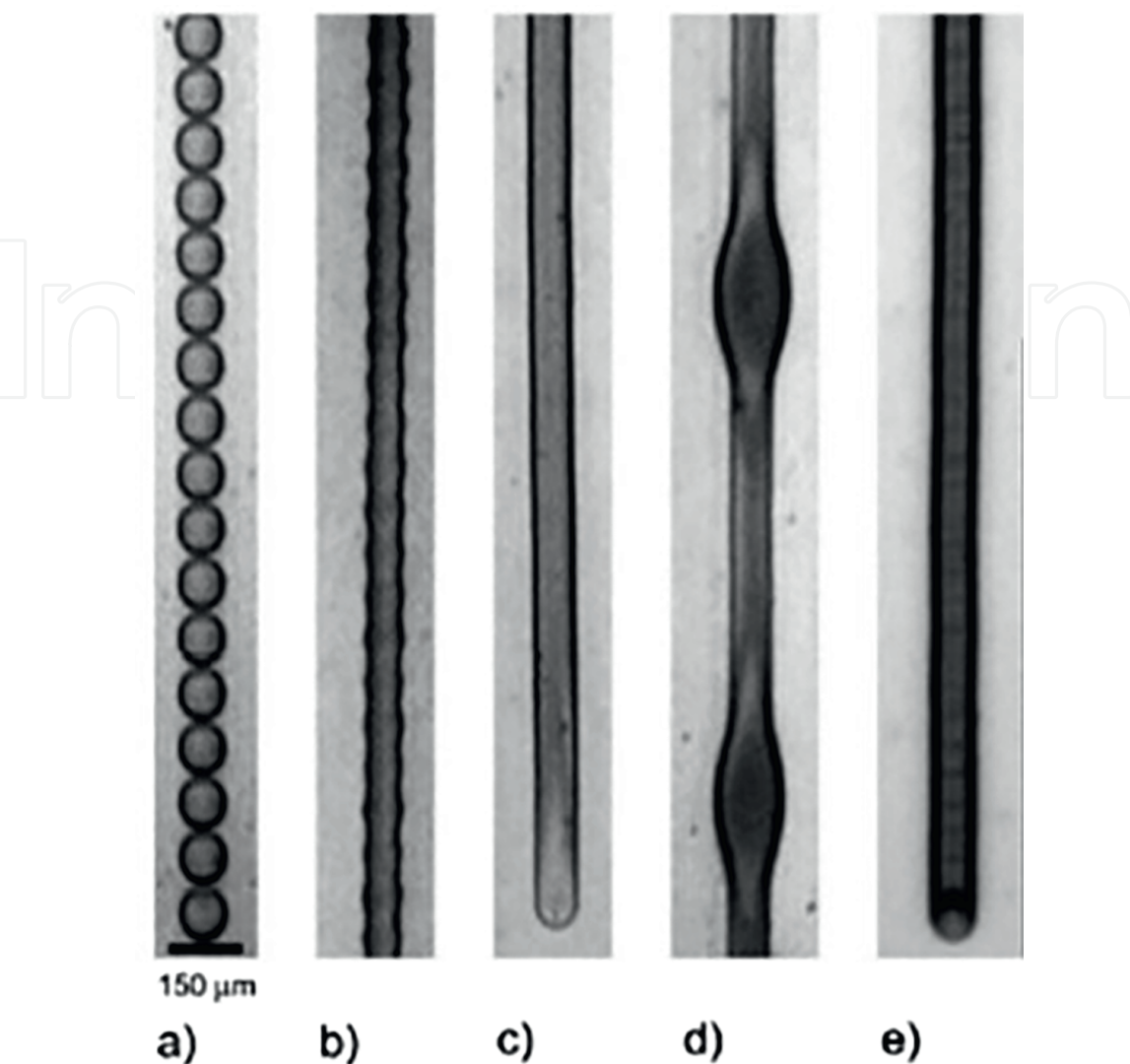


Figure 8. Illustration evidencing the relationship between dot spacing and morphology of printed lines. (a) Large dot spacing caused drops to be isolated from each other. (b) Less drop spacing merges drops but their round edges are still visible. (c) Ideally merged drops forming a homogeneously printed line. (d and e) low drop spacing causing localized bleeding and coffee ring effect at the edges of the printed line, respectively. Reprinted with permission from [97]. Copyright (2022) ACS.

of the drops and their displacing accuracy. Because of this, higher printhead height is correlated with lower printing accuracy (higher prevalence of ink spraying and splatter). An optimum height should be found taking into consideration the type of ink used and the morphology the drops develop during the ejection phase. Some inks, especially metallic nanoparticle-based ones also demand heating of the printhead, as a way of helping the flow of the ink, as this promotes nanoparticle distancing and decreased viscosity, which avoids nozzle clogging [108, 109]. During printing, it is also essential to make sure the distance between the printhead and the substrate remains stable which in some printer models is assured through a vacuum-assisted bed that prevents substrate vibration and displacement [50].

Voltage Waveform. The waveform is the parameter that causes the piezoelectric crystal to deform, generating negative pressure at the printhead nozzles, and causing the ink drops to be jetted. To complete the drop ejection process, a bipolar voltage waveform is responsible for the fill/fire pulses (**Figure 9a**). The higher the voltage, the higher the speed of the generated droplet. This occurs because the pressure

Figures of merit	Description	Observations
Uniformity and homogeneity	Uniformity relates to ink thickness and width irregularities (e.g., line width, raggedness, blurriness). Homogeneity is linked to distribution of ink in the printed pattern area.	Coffee ring effect is an ink inhomogeneity feature. The size of a printed line depends on drop volume and droplet-substrate interactions. Typically, printed line width is higher than the design value. Ink thickness is measured by profilometry or confocal microscopy. Its morphology by optical or SEM. Image analyzer are used for quantitative characterization. Inconsistency due to misfiring, nozzle-plate flooding and satellite drop formation (related to the ink rheology and surface tension)
Consistency	Consistency of ink flow guaranteeing a constant process (drop volume, full dot drop)	
Resolution	Capacity to reproduce printed pattern details	Addressability (dpi, lpi of a inkjet printer or npi of a printhead); dot spacing; sharpness and contrast;
Drop placement error	Difference between the target and impact locations, related to printing accuracy and precision.	Error influenced by the precision of the nozzle manufacturing and the nozzle-substrate distance.
Repeatability	Agreement between successive measurements of drop placement	Can be tested through observation or electrical conductivity measurements (consistent for the same patterns over different prints)
Wettability	Preference of a fluid to maximize the surface contact with the substrate and spread over it	Weber number, Z number, contact angle, surface tension
Adhesion	Adhesion of the ink to the substrate and cohesion between layers	Surface tension, surface energy of the substrate, topography of substrate
Electrical resistivity	Can be measured as surface or volume resistivities	Two-point probes method or Van der Paw method (for better accuracy)
Electromechanical behavior	Deformability of the printed pattern	Gauge factor; geometrical layout of printed pattern
Ink fracture	Crackling of the deposited ink	Optical analysis
Flexibility/stretchability	How much the ink is able to deform and return to its native state without losing its properties	Intrinsically flexible/stretchable inks; Flexible/stretchable substrates; design of patterns to withstand repetitive stress loading

Table 5.
Summary of figures of merit used to classify the quality of the inkjet printing process.

created inside the chamber is consequently superior [116]. To recreate the desired image, the inkjet printer is connected to adequate computer software that supports the upload of the image and allows for the printing settings to be defined. In the case of the piezoelectric DoD method, a voltage is applied across a piezoelectric crystal under a pre-defined time and amplitude pattern, which generates the voltage

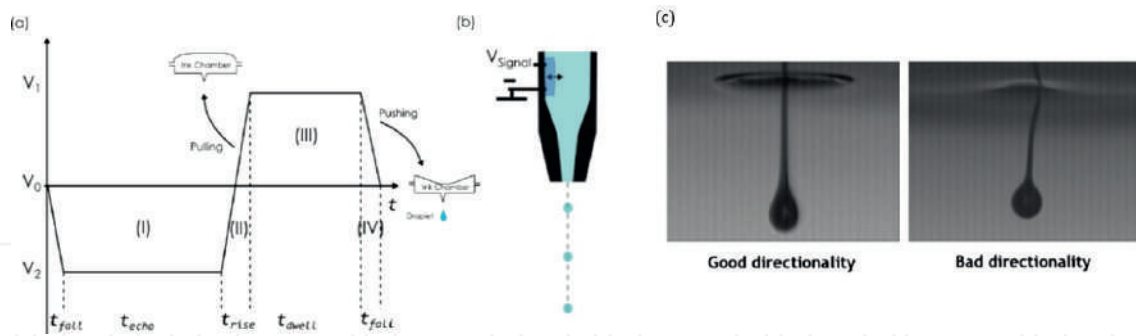


Figure 9. (a) Simple depiction of a waveform. (I) Negative pulse that eliminates residual oscillations after each drop ejection; (II) and (III) are the pressurization and ejection phase, respectively; (b) nozzle pressure chamber as the piezoelectric crystal (darker blue) deforms due to step (III) [114, 115]; (c) jet straightness images obtained from a high-speed camera. Reprinted from [50].

waveform [114]. As depicted in **Figure 9a**, the waveform has four main phases – the damping and relaxation period that prepares the chamber to start the cycle (phase I, or t_{echo}), then, the pressurization (phase II) causes the ink chamber and nozzles to fill and defines the volume that will be ejected. During the next phase (phase III, or dwell time) there is a slight pause for stabilization of the ink inside the chamber. The cycle ends in phase IV, with the ejection of the ink droplets due to the pushing pressure caused by the piezoelectric crystal. Depending on the characteristics of the ink, the waveform can be optimized, and the best jetting performance is associated with fast, round, and stable droplets without tails [114]. To achieve this, the total waveform duration, number of phases, and the individual phase amplitude, durations, and slew rates (slopes), can be manually adjusted [114]. Recent inkjet printers are already equipped with waveform tuning ability, and in some cases encompass real-time drop-watcher high-speed cameras that capture images such as the ones in **Figure 9c** [108, 109]. This allows for simultaneous tracking and optimization of the profile of the jetted ink drops.

Jetting Frequency and Printhead Speed. The frequency in which the piezoelectric crystal is actuated is intimately related to the waveform and the printhead speed, which can be varied, affecting the rate at which droplets are jetted. If the printhead moves at a low speed the printhead nozzles will be actuated at a lower frequency. By generating waveforms with longer echo and dwell times, the jetting frequency will also be stalled, and vice-versa. As a result, this parameter can be simultaneously studied with the voltage and printhead speed to obtain higher quality printing. As seen in **Figure 10**, the shape of the jetted drops is dependent upon the jetting frequency and varies with the ink characteristic (viscosity, rheology, surface tension).

Number of printed layers. It is also a frequently studied parameter, particularly in what concerns its influence on electrical conductivity. To illustrate this, Rihen et al. studied the effects of the number of printed layers (1–5 layers), drop spacing (1016 DPI – 1693 DPI), and curing temperature (75–120°C) in the final conductivity of an Ag ink [89]. In this study, they found that the best conductivity was obtained for 3 printed layers, 1270 DPI, and a curing temperature of 120°C. It was also found that the number of printed layers strongly affected the final conductivity and that when too many layers were printed, excessive ink ejection ended up causing bleeding of the ink during printing and cracks after the heat-treatment was conducted. Hence, when possible, the number of printed layers should be limited to an “optimum minimum”

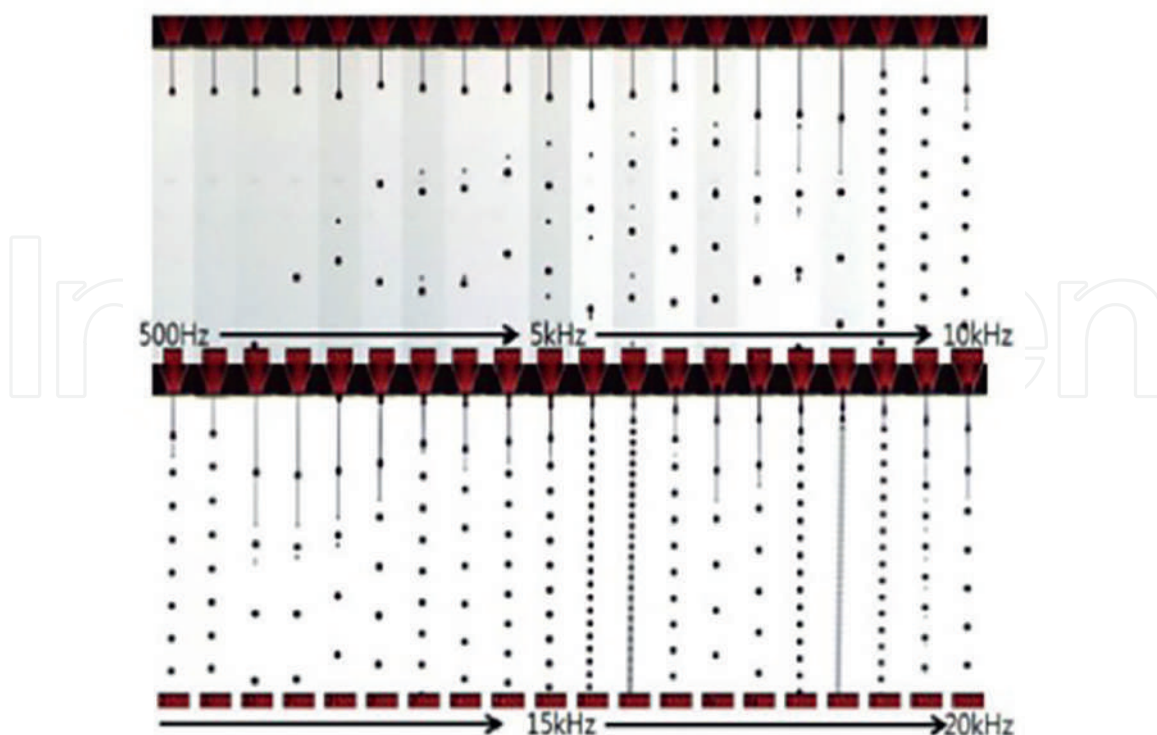


Figure 10.
 Jetting behavior with increasing frequency. Reprinted from [117] with permission of AIP publishing.

as it can end up affecting conductivity and printing quality in a negative manner. Moreover, by finding a compromise between resolution and number of layers the printing process can become more economical in terms of ink used.

Design-related variables. The layout of the circuit designs to be printed needs to obey specific rules that depend upon the type of circuit, inkjet printer, printhead, and ink. The process of developing a certain circuit to be printed starts by defining the schematic circuit design in CAD, and after making sure it obeys the rules it is converted to bitmap for printing (**Figure 11a**) [118]. Design-related variables include the minimum resolution, horizontal/vertical line drop spacing, horizontal/vertical line width, horizontal/vertical line thickness, orientation of the design, and the angles of the line connections and design borders [118]. As depicted in **Figure 11c**, different line spacing between two consecutive lines can cause the lines to overlap. Hence, by managing the way the design is created, different results can be obtained depending on the final objective. Moreover, by anticipating the probability of flooding or coffee ring effect of the ink in specific areas, the design can be manipulated to prevent them through pattern compensation methods, as advanced by Vila et al. [119].

2.3.5 Inkjet printing quality indicators

Fabrication of PE devices using IJP faces a series of challenges for enhancing the technology merit indicators, which are application dependent. These relate mainly to printing quality indicators (printed pattern homogeneity, resolution, consistency), electrical conductivity, mechanical durability, and device flexibility/stretchability. In IJP, the printing quality involves complicated interactions between many factors including the printer, the printhead, the substrate, and the ink [49].

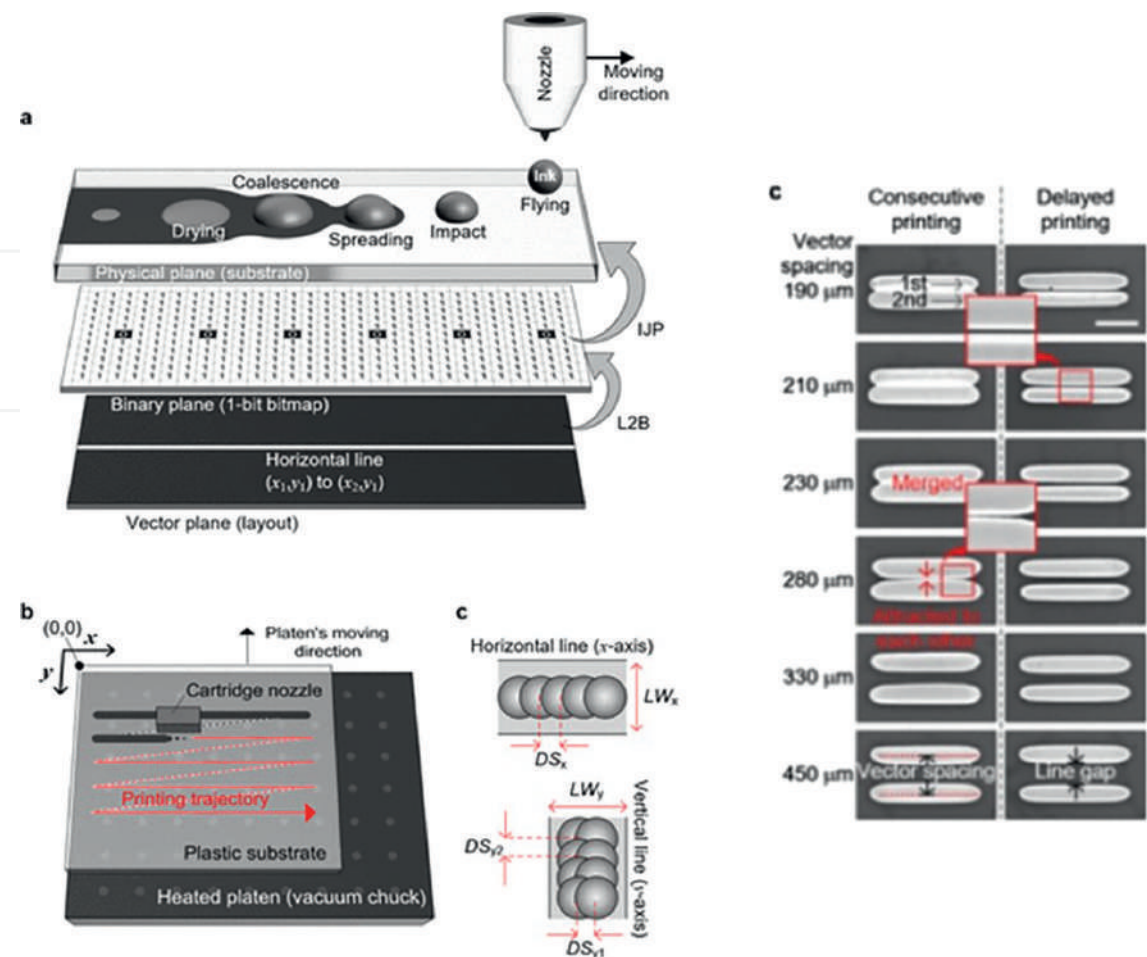


Figure 11. (a) IJP metal track generation along the x -axis (mask-less): From a CAD layout drawing (a vector file) to a binary plane (a bmp file) and from the binary plane to a physical substrate surface. (b) a unidirectional IJP system. (c) Microscopic images of the two printed lines with varying vector spacings from 190 to 450 μm (scale bar is 500 μm).

Printed pattern resolution and uniformity are determined by droplet-substrate interactions, ink solvent evaporation rate, and capillary flow inside the ink droplet. The printed lines' dimensions, namely their width, depend upon the drop spacing and coalescing time. There is a relationship between drop spacing, line width, and electrical resistance. The electrical resistance is directly proportional to the drop spacing and inversely proportional to the line width.

3. Inkjet printing of smart products

IJP is already ubiquitously employed for printing decorative layers of products. In addition to this, during the past decade, it has also started to establish itself as a low-cost manufacturing process for large-area electronics applied to smart devices [43, 50]. As previously stated, potential markets include the development of electrodes and charge transport layers for thin-film devices, energy storage devices, electronic textiles, wearables, and smart tags and sensors for remote monitoring and logistics of marketable goods. In some of these cases, technological advancements have already allowed products to emerge and enter the market [120, 121].

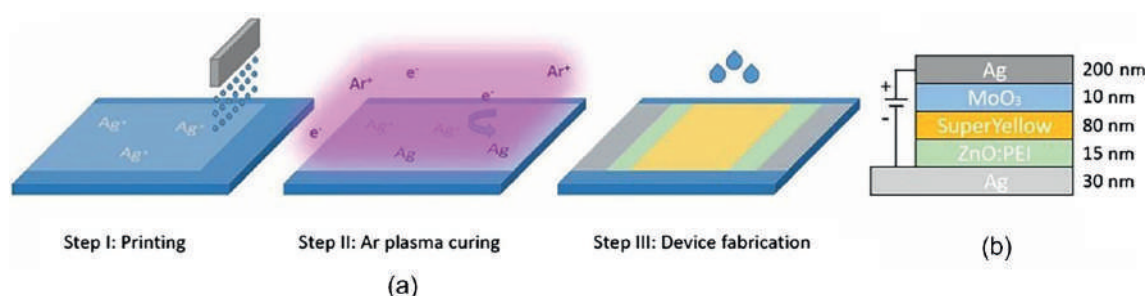


Figure 12.
 Overview of the device fabrication. Reproduced from [123].

3.1 Flexible OLED and QLED

Many devices nowadays encompass screens made from transparent electrodes. These are usually obtained using metal oxides (such as ITO) and employed in light-emitting diodes (LED) devices. As stated above, however, ITO is brittle, and its exploitation and end-of-life cycle processing damaging to the environment. Hence, organic and hybrid alternatives, such as OLED and quantum-dot light-emitting diode (QLED) displays are starting to dominate the markets [122]. Thanks to the characteristics of the employed materials, inkjet printing is often a great manufacturing pathway to develop these devices [123]. As seen in **Figure 12**, ITO-free OLED can be obtained using inkjet-printed and low-temperature plasma-sintered Ag electrodes. A MOD ink was used to optimize the reduction effect of the plasma treatment, and the emissive layer of Super yellow was spin-coated.

Regarding organic printable materials capable of replacing the ITO electrodes, PEDOT:PSS is the favored organic semiconductor. Jürgensen et al. studied the tuning of a PEDOT:PSS solution with surfactants, as a way of inkjet printing green electrodes in OLED with reduced surface tension [124]. Moreover, Cinquino et al. concluded that by granting a surface tension value of 28 – 40 mN/m and adding 40 vol.% of a low-boiling-point co-solvent proper substrate wetting was granted [125]. As for inorganic materials, perovskite nanocrystal (PeNC) solutions have also been investigated as inkjet printable color conversion layers (CCL) in PeNC/OLED hybrid displays [126]. These displays are used universally in entertainment devices, including augmented and virtual reality devices with enhanced performance. Another field of application of these displays respects healthcare devices and photomedicine, in particular, in the development of displays for photodynamic therapy (PDT), which vows to attack cancer cells using specific light-emitting wavelengths [127].

3.2 Organic photovoltaic (OPV) cells

Similarly, regarding OPV cells, the tendency is also to replace metal-oxide alloys with more environmentally friendly and easy to process materials. As an example, Alamri et al. developed fully-inkjet-printed hybrid perovskite photodetectors using Graphene/Perovskite/Graphene [128]. Schackmar and co-workers also came up with an approach to develop all-inkjet-printed absorbers and charge transport layers [129]. As seen in **Figure 13a**, a p-i-n-perovskite solar cell architecture was created. The triple-cation perovskite absorber layer (TCP, brown) and

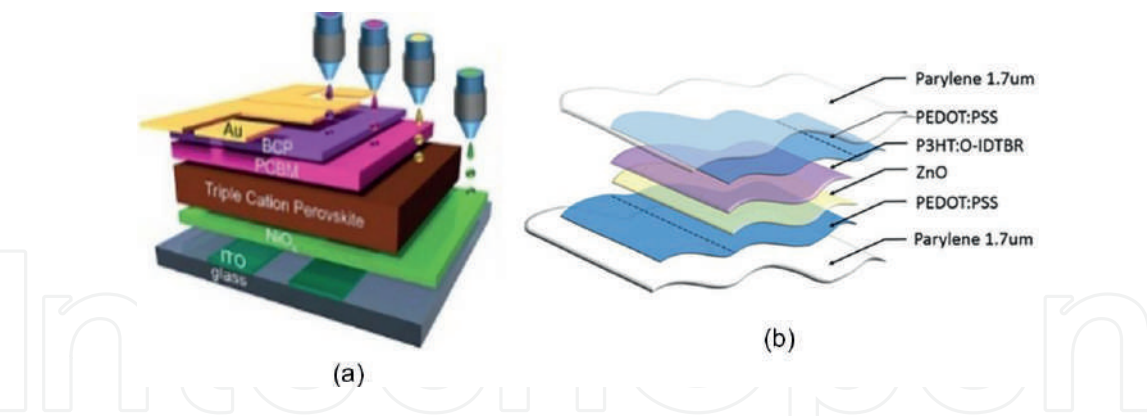


Figure 13.
(a) Schematic of the p - i - n -perovskite solar cell architecture with printed absorber and extraction layers. Reprinted from [129]; (b) schematic of the layer-by-layer composition of the solar cells made from PEDOT:PSS inkjet-printed electrodes. Reprinted from [69].

the double layer ETL made of PCBM and BCP (pink and purple, respectively) were deposited by inkjet printing. Bihar et al. also developed a fully-inkjet printed alternative to develop OPV in which PEDOT:PSS was used to develop the electrodes (Figure 13b) [69].

3.3 Energy storage applications

Inkjet printing technology is being vastly employed in the development of supercapacitors (SC), triboelectric nanogenerators, and batteries. Even though many challenges still have to be overcome for these devices to reach competitive performance, promising alternatives already exist [130]. For example, graphene-based solutions are vastly studied throughout the literature for IJP of supercapacitors [131, 132]. Li et al. inkjet printed disposable micro-supercapacitors (MSC) on paper using conductive inks based on the ternary composite of PEDOT:PSS, graphene quantum dots, and graphene [133]. In Figure 14, the resulting MSC are pictured in different array dispositions.

Giannakou and colleagues developed 3D conformable supercapacitors intended for epidermal energy storage. To achieve this, they inkjet-printed nickel (II) oxide active electrodes over PVA substrate. As a proof-of-concept, the SC was used on the skin of test subjects, and energy from their movements was successfully harvested to light a LED [134]. Energy harvesters can also be printed over textiles as a way of obtaining self-powered garments with sensing and monitoring abilities [135].

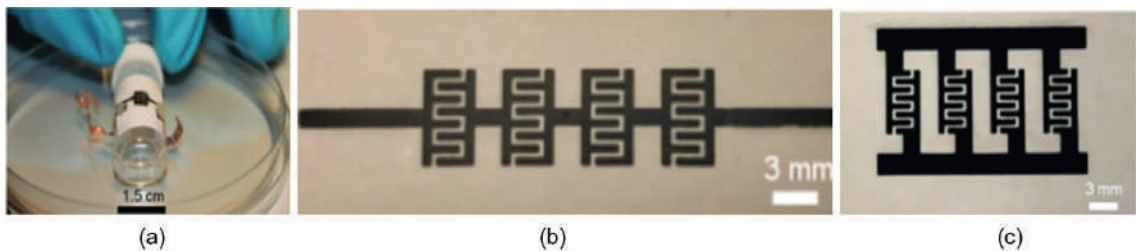


Figure 14.
(a) Microsupercapacitor (MSC) printed on photo paper for flexibility performance test, (b) fully-printed MSC array with 4 MSC connected in series on carton paper, (c) fully-printed MSC array with 4 MSC connected in parallel on carton paper. The bus lines were printed with 17 passes. Reprinted from [133].

VARTA company has recently started to apply inkjet printing to the development of batteries to power sensors, and smart tags for intelligent packaging applications. Different electrochemical systems and electrodes can be printed in a stacked or coplanar manner depending on the envisioned design of the battery [136].

3.4 Sensors, e-textiles, and biomonitoring devices

Sensors are vital to transduce physical changes into readable data. Several inkjettable materials can be used as the functional part of sensors, whose electrical conductivity varies according to those changes and is later processed into digital outputs for monitoring. The most frequently developed physical sensors measure mechanical (pressure, force, strain), temperature, and humidity changes. Metal nanowires [137], metallic nanoparticles [138], polymer micro/nanostructures [139], CNT, and graphene have been applied to the design of piezoresistive flexible tactile sensors [140–142]. To work efficiently, the latter ones must be homogeneously dispersed in an elastomeric matrix, in concentrations above the electrical conductivity percolation threshold [143]. To produce piezoelectric pressure sensors the most used materials are piezoelectric ceramics, ceramic/polymer composites, and single crystals [144, 145]. As for capacitive sensing applications, SWNT/PDMS electrodes are effective options [145, 146]. Inkjet printing has also been extensively used to produce temperature, and humidity sensors that can be applied in standalone settings or, thanks to the development of the IoT can work as scattered sensor networks for remote and connected monitoring applications. Thanks to their inherent conformability, low-cost, biocompatibility, tunability, accuracy, and adequate sensing range, the pressure, temperature, and humidity printable sensors, have started to be applied in e-textiles and biomonitoring applications. As an example, Farooqui et al. successfully developed a smart bandage to remotely monitor chronic wounds through inkjet printing of a resistive sensor sensitive to pH [147].

Wearables and electronic textiles can be used for applications ranging from human-machine interaction (HMI), fashion, haptics, and biomonitoring. Regarding biomonitoring, different sensors can be inkjet-printed over textiles or conformable polymeric substrates (PDMS, PET, PEN, PEEK) and retrieve accurate biological data, thanks to the close proximity to the body. Pressure, strain [67], temperature [148], and humidity sensors [17], are the most frequently printed, nonetheless, photoplethysmography (PPG), electrocardiography (ECG), and electroencephalogram (EEG)

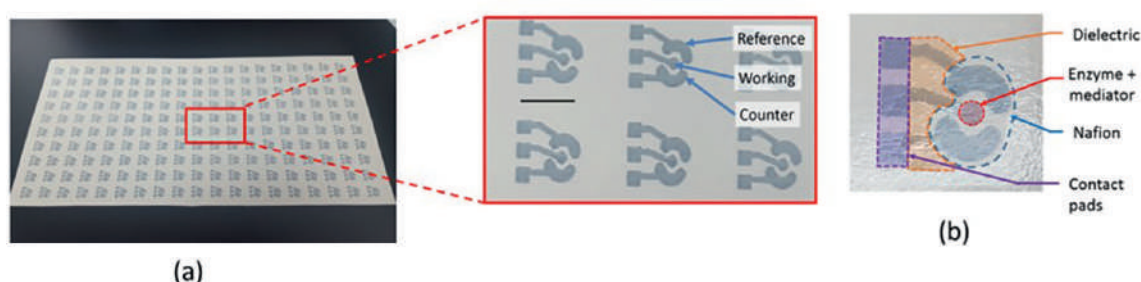


Figure 15.
 (a) Inkjet-printed glucose biosensors; (b) fully printed biosensor and identification of the different printed layers, namely the electrode (PEDOT:PSS), the dielectric, the biological coating containing the enzyme and the mediator, and the encapsulation layer. Reprinted from [156].

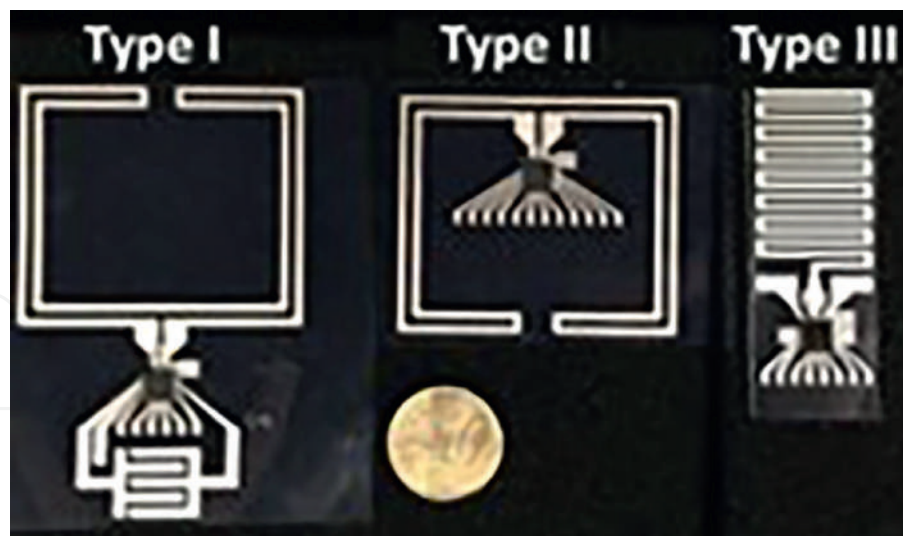


Figure 16. Three types of printed, passive tags on a flexible substrate for operation in the UHF RFID band (902–928 MHz). Reprinted from [161].

sensors can be inkjet-printed as well [49, 135, 149–152]. Electroluminescent devices can also be printed over textiles to enhance their functionality [153].

Flexible printed and biocompatible sensors placed in direct contact with the human body are also valuable for sensing specific biomarkers. This can be achieved by IJP of enzyme-functionalized inks [154]. Mass et al. enzyme-functionalized silica nanoparticles and mixed them with SWCNT to create a bio-ink with catalytic activity [154]. Biocompatible graphene-based biosensors can be printed as well to monitor the effect of antiviral drugs through impedance analysis [155]. Bihar and colleagues also developed a disposable glucose sensor by inkjet printing PEDOT:PSS as electrodes, and a glucose oxidase solution as the sensing material [156]. A dielectric ink was printed to isolate the electrode interconnects as depicted in Figure 15.

3.5 Smart tags and logistics

Inkjet printing can be used in the development of antennas, radio frequency identifier (RFID) chips, and near-field communication (NFC) chips, which can work as smart labels and sensor tags. Temperature, humidity, and strain sensors are usually paired with these labels to develop intelligent packaging and/or tracking applications [157, 158]. For this purpose, paper is one of the most used substrates [159]. Another important application for smart tags is food quality monitoring. By combining humidity, ammonia, temperature, and volatile organic compounds (VOC) sensors the state of perishable goods can be evaluated and the food supply chain optimized accordingly [160]. For this purpose, Quintero et al. developed a multi-sensing platform where an RFID chip was integrated with inkjet-printed sensors (ammonia, humidity, and temperature) over a PEN substrate [160]. Baubauer and co-workers also studied the printing of different types of passive tags over flexible substrates, when integrated with a rigid RFID chip, as illustrated in Figure 16 [161]. In this case, the purpose of the tags was to serve as user-interactive touch sensors. One interesting asset of these types of labels is the fact that they can be reset and reprogrammed.

Since packaging is meant to be disposable, by recovering and reprogramming the tags they can be reused in other applications before being ultimately recycled [162].

4. Advanced inkjet printing techniques

IJP is a mature technology and recently has been used to print functional inks for PE devices. This novel use demanded developments in terms of new printing equipment and inks. As a result, advanced IJP technologies have emerged, responding to the requirements of novel applications. These advanced technologies are focused on increasing printing resolution and speed, printing of high viscosity inks (with higher electrical conductivity), printing over non-planar substrates, and enlarging the range of materials that can be printed.

A novel double-shot IJP technique has been developed, which allows for the deposition of two types of inks at the same position [163]. In this way, conductive and dielectric inks can be printed at the same position, allowing the construction of devices. Reactive inkjet printing, which also uses two nozzles, combines the processes of material deposition and chemical reaction to print over a substrate material, enlarging the type of ink materials.

EHD-IJP allowed high-resolution printing, paving its use in micro/nano manufacturing of electronic devices [45]. EHD-IJP is a direct patterning technique that can also be used as a thin film deposition technique (e.g., electrospraying, electrospinning). Furthermore, multi-nozzle implementation has been proposed, but nozzle density is still low [50]. EHD-IJP also allows printing of high viscosity inks and consequently has huge potential for fabricating 3D patterns [163].

Needle-based printing is a recent technology to dispense relatively high viscosity ink through a fine nozzle [50]. Droplets are ejected from the nozzle exit by the motion of the needle, which can be operated by air pressure or piezoelectric actuator. This technique can handle high viscosity inks.

Micro-plotter is a technology that also allows dispensing of relatively high viscosity ink through a fine nozzle [50]. The dispensing mechanism is based on the ultrasonic pumping action at the core of the micro-plotter head, a micropipette. The mechanism is capable of depositing ink droplets with dot size of less than 2 μm , which is smaller than an inkjet system, even when using relatively high viscosity inks (up to 450 cP).

Other droplet-based techniques have been developed, mainly for printing on non-planar substrates, such as aerosol jet printing, surpassing the limitations of both inkjet and EHD-IJP techniques. Aerosol jet printing uses high-speed ejection of aerosols instead of liquid droplets [164, 165]. The aerosol is produced by atomization of ink, which produces very small droplets with diameters in the range of 1 to 5 μm . Due to the aerodynamic effect, it also allows higher resolution for fabricating micro- and nanoscale devices. Furthermore, aerosol jetting allows different inks to be conformably printed onto the substrate.

High-resolution 3D patterning combines IJP with 3D printing technologies [166]. High-resolution insulating and conductive layers can be printed using multiple print-heads in the same printing system. However, this requires a high degree of deposition precision that can be achieved by the use of phase-change inks (activated by chemical or thermal triggers) with no solvents. 3D structures can also be produced by IJP, by deposition of layer-by-layer of two reactive components, followed by polymerization. This is a technology of current intense research and fast growth.

5. Concluding remarks and future trends

In this chapter, the main topics concerning the IJP manufacturing of printed electronics have been discussed. Being an additive manufacturing technology, some of its advantages concern lower associated costs, material economization, and design freedom. Since its establishment as an alternative for electronics manufacturing, different variations of this technology have emerged, nonetheless, piezoelectric IJP is the most widespread method. Many functional inks have already been optimized for IJP and are commercially available. Despite this, several factors linked to the printing process can still negatively influence the printing output in terms of both printing quality and electrical conductivity and demand optimization.

As for IJP application in the current PE market, there is an undeniable growing tendency. However, it is still early to anticipate the potential of IJP technology in the long run because of all the other options currently being developed. Because of the drawbacks associated with piezoelectric IJP, namely the tendency for nozzles to clog, the limited ink viscosity range (and consequently limited electrical conductivity), and the elevated number of factors that influence the printing process, it is possible that IJP gets to be used in specific niche applications, whereas needle-based and EHD-IJP might ultimately transcend piezoelectric IJP in terms of applicability.

Acknowledgements

This work has been supported by NORTE-06-3559-FSE-000018, integrated invitation NORTE-59-2018-2041, aiming Hiring of Highly Qualified Human Resources, co-financed by the Regional Operational Programme North 2020, thematic area of Competitiveness and Employment, through the European Social Fund, and by the scope of projects with references UIDB/05256/2020 and UIDP/05256/2020, financed by FCT—Fundação para a Ciência e Tecnologia, Portugal.

Author details


Cláudia Buga^{1,2} and Júlio C. Viana^{1,2*}

1 IPC/LASI—Institute for Polymers and Composites/Associated Laboratory for Smart Systems, University of Minho, Guimarães, Portugal

2 DTx Colab—Digital Transformation, University of Minho, Guimarães, Portugal

*Address all correspondence to: jcv@dep.uminho.pt

IntechOpen

© 2022 The Author(s). Licensee IntechOpen. This chapter is distributed under the terms of the Creative Commons Attribution License (<http://creativecommons.org/licenses/by/3.0>), which permits unrestricted use, distribution, and reproduction in any medium, provided the original work is properly cited. 

References

- [1] Cruz SMF, Rocha LA, Viana JC. Printing technologies on flexible substrates for printed electronics. In: Rackauskas S, editor. *Flexible Electronics*. Rijeka: IntechOpen; 2018. DOI: 10.5772/intechopen.76161
- [2] Khan S, Lorenzelli L, Dahiya RS. Technologies for Printing Sensors and Electronics over Large Flexible Substrates: A review. *IEEE Sensors Journal*. 2015;**15**(6):3164-3185
- [3] Matsui H, Takeda Y, Tokito S. Flexible and printed organic transistors: From materials to integrated circuits. *Organic Electronics*. 2019;**75**:105432
- [4] Correia V, Mitra KY, Castro H, Rocha JG, Sowade E, Baumann RR, et al. Design and fabrication of multilayer inkjet-printed passive components for printed electronics circuit development. *Journal of Manufacturing Processes*. 2018;**31**:364-371. DOI: 10.1016/j.jmapro.2017.11.016
- [5] Castro HF, Correia V, Sowade E, Mitra KY, Rocha JG, Baumann RR, et al. All-inkjet-printed low-pass filters with adjustable cutoff frequency consisting of resistors, inductors and transistors for sensor applications. *Organic Electronics*. 2016;**38**:205-212
- [6] Correia V, Oliveira J, Perinka N, Costa P, Sowade E, Mitra KY, et al. All-printed Piezoresistive sensor matrix with organic thin-film transistors as a switch for crosstalk reduction. *ACS Applied Electronic Materials*. 2020;**2**(5):1470-1477. DOI: 10.1021/acsaelm.0c00214
- [7] Franco M, Alves R, Perinka N, Tubio C, Costa P, Lanceros-Mendéz S. Water-based graphene inks for all-printed temperature and deformation sensors. *ACS Applied Electronic Materials*. 2020;**2**(9):2857-2867. DOI: 10.1021/acsaelm.0c00508
- [8] Yap YL, Wang C, Sing SL, Dikshit V, Yeong WY, Wei J. Material jetting additive manufacturing: An experimental study using designed metrological benchmarks. *Precision Engineering*. 2017;**50**:275-285. DOI: 10.1016/j.precisioneng.2017.05.015
- [9] Krykpayev B, Farooqui MF, Bilal RM, Shamim A. A WiFi tracking device printed directly on textile for wearable electronics applications. In: *IEEE MTT-S International Microwave Symposium Digest*. 2016. p. 4
- [10] Ma S, Ribeiro F, Powell K, Lutian J, Møller C, Large T, et al. Fabrication of novel transparent touch sensing device via drop-on-demand inkjet printing technique. *ACS Applied Materials & Interfaces*. 2015;**7**(39):21628-21633
- [11] Ando B, Baglio S, Castorina S, Crispino R, Marletta V. An inkjet printed pressure sensor for applications in active ageing monitoring. In: *SAS 2019-2019 IEEE Sensors Applications Symposium, Conference Proceedings*; 2019
- [12] Dankoco MD, Tesfay GY, Benevent E, Bendahan M. Temperature sensor realized by inkjet printing process on flexible substrate. *Materials Science & Engineering, B: Solid-State Materials for Advanced Technology*. 2016;**205**:1-5
- [13] Vuorinen T, Niittynen J, Kankkunen T, Kraft TM, Mäntysalo M. Inkjet-printed graphene/PEDOT:PSS temperature sensors on a skin-conformable polyurethane substrate. *Scientific Reports*. 2016;**6**(1):35289. DOI: 10.1038/srep35289

- [14] Katerinopoulou D, Zalar P, Sweelssen J, Kiriakidis G, Rentrop C, Groen P, et al. Large-area all-printed temperature sensing surfaces using novel composite thermistor materials. *Advanced Electronic Materials*. 2019;5(2):1-7
- [15] Popov VI, Kotin IA, Nebogatikova NA, Smagulova SA, Antonova IV. Graphene-PEDOT: PSS humidity sensors for high sensitive, low-cost, highly-reliable, flexible, and printed electronics. *Materials*. 2019;12(21):1-9
- [16] Jung M, Lee J, Vishwanath SK, Kwon OS, Ahn CW, Shin K, et al. Flexible multimodal sensor inspired by human skin based on hair-type flow, temperature, and pressure. *Flexible and Printed Electronics*. 2020;5(2):16
- [17] Barmpakos D, Segkos A, Tsamis C, Kaltsas G. A disposable flexible humidity sensor directly printed on paper for medical applications. *Journal of Physics Conference Series*. 2017;931(1): 012003
- [18] Cruz S, Viana JC, Dias D, Rocha LA. Pressure sensing platform for health monitoring. In: 2014 IEEE International Symposium on Medical Measurements and Applications (MeMeA); 2014. pp. 1-5
- [19] Salim A, Lim S. Review of recent inkjet-printed capacitive tactile sensors. *Sensors*. 2017;17(11):2593
- [20] Chiolerio A, Rivolo P, Porro S, Stassi S, Ricciardi S, Mandracci P, et al. Inkjet-printed PEDOT:PSS electrodes on plasma-modified PDMS nanocomposites: Quantifying plasma treatment hardness. *RSC Advances*. 2014;4(93):51477-51485. DOI: 10.1039/C4RA06878E
- [21] Mohammed MG, Kramer R. All-printed flexible and stretchable electronics. *Advanced Materials*. 2017;29(19):1604965. DOI: 10.1002/adma.201604965
- [22] Seipel S, Yu J, Periyasamy AP, Viková M, Vik M, Nierstrasz VA. Characterization and optimization of an inkjet-printed smart textile UV-sensor cured with UV-LED light. *IOP Conf Ser. Materials Science and Engineering*. 2017;254(7):072023
- [23] Gardner SD, Haider MR, Islam MT, Alexander JID, Massoud Y. Aluminum-doped zinc oxide (ZnO) inkjet-printed piezoelectric Array for pressure gradient mapping. *Midwest Symposium on Circuits and Systems*. 2019;2019:1101-1104
- [24] Fang M, Li T, Zhang S, Rao KV, Belova L. Design and tailoring of inks for inkjet patterning of metal oxides. *Royal Society Open Science*. 2020;7(4):200242. Available from: <https://royalsocietypublishing.org/doi/abs/10.1098/rsos.200242>
- [25] Printed Electronics Market 2021: Industry Size, Regions, Emerging Trends, Growth Insights, Development Scenario, Opportunities, and Forecast By 2027 [Internet]. 2021. Available from: <https://www.marketstatsville.com/printed-electronics-market>
- [26] Functional Printing-Global Market Trajectory and Analytics. 2021
- [27] Inkjet Printing Market-Growth, Trends, Covid-19 Impact, and Forecasts (2022-2027) [Internet]. 2021. Available from: <https://www.mordorintelligence.com/industry-reports/inkjet-printing-market>
- [28] Functional Inks-Global Market Trajectory and Analytics [Internet]. 2021. Available from: <https://www.researchandmarkets.com/reports/5302023/>

functional-inks-global-market-trajectory-and

[29] Global Printed Electronics Market-Industry Trends and Forecast to 2028 [Internet]. 2021. Available from: <https://www.databridgemarketresearch.com/reports/global-printed-electronics-market>

[30] Global Functional Printing Market-Industry Trends and Forecast to 2027 [Internet]. 2020. Available from: <https://www.databridgemarketresearch.com/reports/global-functional-printing-market>

[31] IDTechEx. Materials for Printed/Flexible Electronics 2021-2031: Technologies, Applications, Market Forecasts. 2021. IDTechEx Research finds, the most interesting emerging technologies

[32] Cruz SMF, Rocha LA, Viana JC. Printing technologies on flexible substrates for printed electronics. Rackauskas S, editor. Flexible Electronics. London: IntechOpen; 2018. p. 25

[33] Rivadeneyra A, Loghin FC, Falco A. Technological integration in printed electronics. In: Rackauskas S, editor. Flexible Electronics. Rijeka: IntechOpen; 2018. DOI: 10.5772/intechopen.76520

[34] Beedasy V, Smith PJ. Printed electronics as prepared by inkjet printing. Materials. 2020;13(3):704. Available from: <https://pubmed.ncbi.nlm.nih.gov/32033206>

[35] Sattler KD. 21st Century nanoscience—A handbook: Design strategies for synthesis and fabrication Sattler KD, editor. Vol. 1st ed. United Kingdom: Taylor & Francis; 2019. p. 496

[36] Shah M, Lee D-G, Lee B-Y, Hur S. Classifications and applications of inkjet

printing technology: A review. IEEE Access. 2021;(9):140079-140102

[37] Kwon H, Hong J, Nam SY, Choi HH, Li X, Jeong YJ, et al. Overview of recent progress in electrohydrodynamic jet printing in practical printed electronics: Focus on the variety of printable materials for each component. Advanced Materials. 2021;2(17):5593-5615. DOI: 10.1039/D1MA00463H

[38] Yu M, Ahn KH, Lee SJ. Design optimization of ink in electrohydrodynamic jet printing: Effect of viscoelasticity on the formation of Taylor cone jet. Materials and Design. 2016;89:109-115. Available from: <https://www.sciencedirect.com/science/article/pii/S0264127515305505>

[39] Cai S, Sun Y, Wang Z, Yang W, Li X, Yu H. Mechanisms, influencing factors, and applications of electrohydrodynamic jet printing. Nanotechnology Reviews. 2021;10(1):1046-1078. DOI: 10.1515/ntrev-2021-0073

[40] Skarżyński K, Krzemiński J, Jakubowska M, Słoma M. Highly conductive electronics circuits from aerosol jet printed silver inks. Scientific Reports. 2021;11(1):18141. DOI: 10.1038/s41598-021-97312-5

[41] Modak CD, Kumar A, Tripathy A, Sen P. Drop impact printing. Nature Communications. 2020;11(1):4327. DOI: 10.1038/s41467-020-18103-6

[42] Foresti D, Kroll K, Amissah R, Sillani F, Homan K, Poulikakos D, et al. Acoustophoretic printing. Science Advances. 2018;4:eaat1659

[43] Buga CS, Viana JC. A review on materials and technologies for organic Large-area electronics. Advanced Materials Technologies. 2021;6(6):2001016. DOI: 10.1002/admt.202001016

- [44] Le HP. Progress and trends in ink-jet printing technology. *Journal of Imaging Science and Technology*. 1998;**42**:49-62
- [45] Raje P, Murmu NC. A review on electrohydrodynamic-inkjet printing technology. *International Journal of Emerging Technology and Advanced Engineering*. 2014;**4**(5):174-183
- [46] Derby B. Inkjet printing of functional and structural materials: Fluid property requirements, feature stability, and resolution. *Annual Review of Materials Research*. 2010;**40**(1):395-414. DOI: 10.1146/annurev-matsci-070909-104502
- [47] Cummins G, Desmulliez MPY. Inkjet printing of conductive materials: A review. *Circuit World*. 2012;**38**(4):193-213. DOI: 10.1108/03056121211280413
- [48] Nayak L, Mohanty S, Nayak SK, Ramadoss A. A review on inkjet printing of nanoparticle inks for flexible electronics. *Journal of Materials Chemistry C*. 2019;**7**(29):8771-8795. DOI: 10.1039/C9TC01630A
- [49] Yan K, Li J, Pan L, Shi Y. Inkjet printing for flexible and wearable electronics. *APL Materials*. 2020;**8**(12):120705. DOI: 10.1063/5.0031669
- [50] Kwon K-S, Rahman MK, Phung TH, Hoath S, Jeong S, Kim JS. Review of digital printing technologies for electronic materials. *Flexible and Printed Electronics*. 2020;**5**:043003
- [51] Halverson J. The first pictures: Perceptual foundations of Paleolithic art. *Perception*. 1992;**21**(3):389-404. DOI: 10.1068/p210389
- [52] Wijshoff H. Structure and fluid dynamics in piezo inkjet printheads. *Integrated Assessment*. The Netherlands: Univ. Twente, Enschede; 2008
- [53] Hanson A. British Patent 4.681; 1903
- [54] The Nobel Prize in Chemistry 2000. [cited 2020 Nov 28]. Available from: <https://www.nobelprize.org/prizes/chemistry/2000/summary/>
- [55] Brédas JL, Marder SR, Salaneck WR, Heeger AJ, MacDiarmid AG, Shirakawa H. *Macromolecules*. 2002;**35**(4):1137-1139. DOI: 10.1021/ma0118973
- [56] Fan H, Lu Y, Stump A, Reed ST, Baer T, Schunk R, et al. Rapid prototyping of patterned functional nanostructures. *Nature*. 2000;**405**(6782):56-60. DOI: 10.1038/35011026
- [57] Sirringhaus H, Kawase T, Friend RH, Shimoda T, Inbasekaran M, Wu W, et al. High-resolution inkjet printing of all-polymer transistor circuits. *Science*. 2000;**290**(5499):2123-2126. Available from: <https://www.science.org/doi/abs/10.1126/science.290.5499.2123>
- [58] Evans JRG. Direct ink jet printing of ceramics: Experiment in teleology. *British Ceramic Transactions*. 2001;**100**(3):124-128. DOI: 10.1179/096797801681332
- [59] Mypati S, Dhanushkodi SR, McLaren M, Docoslis A, Peppley BA, Barz DPJ. Optimized inkjet-printed silver nanoparticle films: Theoretical and experimental investigations. *RSC Advances*. 2018;**8**(35):19679-19689. DOI: 10.1039/C8RA03627F
- [60] Li W, Li L, Gao Y, Hu D, Li C-F, Zhang H, et al. Highly conductive copper films based on submicron copper particles/copper complex inks for printed electronics: Microstructure, resistivity, oxidation resistance, and long-term stability. *Journal of Alloys and Compounds*. 2018;**732**:240-247. Available from: <https://www.sciencedirect.com/science/article/pii/S0925838817336290>

- [61] Cui W, Lu W, Zhang Y, Lin G, Wei T, Jiang L. Gold nanoparticle ink suitable for electric-conductive pattern fabrication using in ink-jet printing technology. *Colloids and Surfaces A: Physicochemical and Engineering Aspects*. 2010;**358**(1):35-41. Available from: <https://www.sciencedirect.com/science/article/pii/S0927775710000403>
- [62] Kim MG, Kanatzidis MG, Facchetti A, Marks TJ. Low-temperature fabrication of high-performance metal oxide thin-film electronics via combustion processing. *Nature Materials*. 2011;**10**(5):382-388. DOI: 10.1038/nmat3011
- [63] Que M, Guo W, Zhang X, Li X, Hua Q, Dong L, et al. Flexible quantum dot-sensitized solar cells employing CoS nanorod arrays/graphite paper as effective counter electrodes. *Journal of Materials Chemistry A*. 2014;**2**(33):13661-13666. DOI: 10.1039/C4TA02052A
- [64] Dang MT, Lefebvre J, Wuest JD. Recycling indium tin oxide (ITO) electrodes used in thin-film devices with adjacent hole-transport layers of metal oxides. *ACS Sustainable Chemistry & Engineering*. 2015;**3**(12):3373-3381. DOI: 10.1021/acssuschemeng.5b01080
- [65] Guo Y, Zhong M, Fang Z, Wan P, Yu G. A wearable transient pressure sensor made with MXene Nanosheets for sensitive broad-range human-machine interfacing. *Nano Letters*. 2019;**19**(2):1143-1150
- [66] Shi L, Meng L, Jiang F, Ge Y, Li F, Wu X, et al. In situ inkjet printing strategy for fabricating perovskite quantum dot patterns. *Advanced Functional Materials*. 2019;**29**(37):1903648. Available from: <https://onlinelibrary.wiley.com/doi/abs/10.1002/adfm.201903648>
- [67] Cruz S, Dias D, Viana JC, Rocha LA. Inkjet printed pressure sensing platform for postural imbalance monitoring. *IEEE Transactions on Instrumentation and Measurement*. 2015;**64**(10):2813-2820
- [68] Wang Y-F, Sekine T, Takeda Y, Yokosawa K, Matsui H, Kumaki D, et al. Fully printed PEDOT:PSS-based temperature sensor with high humidity stability for wireless healthcare monitoring. *Scientific Reports*. 2020;**10**(1):2467. DOI: 10.1038/s41598-020-59432-2
- [69] Bihar E, Corzo D, Hidalgo TC, Rosas-Villalva D, Salama KN, Inal S, et al. Fully inkjet-printed, ultrathin and conformable organic photovoltaics as power source based on cross-linked PEDOT:PSS electrodes. *Adv. Materials and Technologies*. 2020;**5**(8):2000226. Available from: <https://onlinelibrary.wiley.com/doi/abs/10.1002/admt.202000226>
- [70] Valentini L, Cardinali M, Grkovic M, Uskokovic PS, Alimenti F, Roselli L, et al. Flexible transistors exploiting P3HT on paper substrate and graphene oxide film as gate dielectric: Proof of concept. *Science of Advanced Materials*. 2013;**5**(5):530-533
- [71] Feast WJ, Tsibouklis J, Pouwer KL, Groenendaal L, Meijer EW. Synthesis, processing and material properties of conjugated polymers. *Polymer*. 1996;**37**(22):5017-5047. Available from: <http://www.sciencedirect.com/science/article/pii/0032386196004399>
- [72] Garlapati SK, Divya M, Breitung B, Kruk R, Hahn H, Dasgupta S. Printed electronics based on inorganic semiconductors: From processes and materials to devices. *Advanced Materials*. 2018;**30**(40):1707600. Available from:

<https://onlinelibrary.wiley.com/doi/abs/10.1002/adma.201707600>

[73] Chen C-B, Kao H-L, Chang L-C, Cho C-L, Lin Y-C, Huang C-C, et al. Fabrication of inkjet-printed carbon nanotube for enhanced mechanical and strain-sensing performance. *ECS Journal of Solid State Science and Technology*. 2021;**10**(12):121001. DOI: 10.1149/2162-8777/ac40d4

[74] Aziz A, Bazbouz MB, Welland ME. Double-walled carbon nanotubes ink for high-conductivity flexible electrodes. *ACS Applied Nano Materials*. 2020;**3**(9):9385-9392. DOI: 10.1021/acsanm.0c02013

[75] Akindoyo JO, Ismail NH, Mariatti M. Development of environmentally friendly inkjet printable carbon nanotube-based conductive ink for flexible sensors: Effects of concentration and functionalization. *Journal of Materials Science: Materials in Electronics*. 2021;**32**(9):12648-12660. DOI: 10.1007/s10854-021-05900-y

[76] Ervasti H, Järvinen T, Pitkänen O, Bozó É, Hiitola-Keinänen J, Huttunen O-H, et al. Inkjet-deposited Single-Wall carbon nanotube micropatterns on stretchable PDMS-Ag substrate-electrode structures for Piezoresistive strain sensing. *ACS Applied Materials & Interfaces*. 2021;**13**(23):27284-27294. DOI: 10.1021/acsami.1c04397

[77] Pandhi T, Chandnani A, Subbaraman H, Estrada D. A review of inkjet printed graphene and carbon nanotubes based gas sensors. *Sensors*. 2020;**20**(19):5642

[78] Saidina DS, Eawwiboonthanakit N, Mariatti M, Fontana S, Hérold C. Recent development of graphene-based ink and other conductive material-based inks for

flexible electronics. *Journal of Electronic Materials*. 2019;**48**(6):3428-3450

[79] Huckaba AJ, Garcia-Benito I, Kanda H, Shibayama N, Oveisi E, Kinge S, et al. Inkjet-printed TiO₂/fullerene composite films for planar perovskite solar cells. *Helvetica Chimica Acta*. 2020;**103**(5):e2000044. DOI: 10.1002/hlca.202000044

[80] Winarski DJ. Development of zinc oxide based flexible electronics. Bowling Green State University; 2019

[81] Mirza F, Sahasrabuddhe RR, Baptist JR, Wijesundara MJB, Lee WH, Popa DO. Piezoresistive pressure sensor array for robotic skin. Popa D, MJB W, editors. *Sensors for Next-Generation Robotics III*. Baltimore, Maryland, United States: SPIE; 2016. pp. 168-179

[82] Wang L, Peng H, Wang X, Chen X, Yang C, Yang B, et al. PDMS/MWCNT-based tactile sensor array with coplanar electrodes for crosstalk suppression. *Microsystems & Nanoengineering*. 2016;**2**(1):16065. DOI: 10.1038/micronano.2016.65

[83] Wang Y-F, Sekine T, Takeda Y, Yokosawa K, Matsui H, Kumaki D, et al. Fully printed PEDOT:PSS-based temperature sensor with high humidity stability for wireless healthcare monitoring. *Scientific Reports*. 2020;**10**:2467

[84] Ozioko O, Kumaresan Y, Dahiya R. Carbon nanotube/PEDOT: PSS composite-based flexible temperature sensor with enhanced response and recovery time. In: 2020 IEEE International Conference on Flexible and Printable Sensors and Systems (FLEPS); 2020. pp. 1-4

[85] Yin Z, Tian B, Zhu Q, Duan C. Characterization and application of

PVDF and its copolymer films prepared by spin-coating and langmuir-Blodgett method. *Polymers*. 2019;**11**(12):2033

[86] Haque RI, Vié R, Germainy M, Valbin L, Benaben P, Boddaert X. Inkjet printing of high molecular weight PVDF-TrFE for flexible electronics. *Flexible and Printed Electronics*. 2015;**1**(1):15001. DOI: 10.1088/2058-8585/1/1/015001

[87] Hu X, Ding Z, Fei L, Xiang Y, lin Y. Wearable piezoelectric nanogenerators based on reduced graphene oxide and in situ polarization-enhanced PVDF-TrFE films. *Journal of Materials Science*. 2019;**54**(8):6401-6409. DOI: 10.1007/s10853-019-03339-5

[88] Suganuma K. *Introduction to Printed Electronics*. 1st ed. New York: Springer New York; 2014. p. 124

[89] Riheen MA, Saha TK, Sekhar P. Inkjet printing on PET substrate. *Journal of the Electrochemical Society*. 2019;**166**:B3036-B3039

[90] Ball AK, Das R, Roy SS, Kisku DR, Murmu NC. Experimentation modelling and optimization of electrohydrodynamic inkjet microfabrication approach: A Taguchi regression analysis. *Sadhana-Academy Proceedings in Engineering Sciences*. 2019;**44**(7):1-16. DOI: 10.1007/s12046-019-1146-5

[91] Bucciarelli A, Adami A, Chandaiahgari CR, Lorenzelli L. Multivariable optimization of inkjet printing process of Ag nanoparticle ink on Kapton. In: *2020 IEEE International Conference on Flexible and Printable Sensors and Systems (FLEPS)*; 2020. pp. 1-4

[92] i Garcia ER. *Inkjet printed microelectronic devices and circuits*. Bellaterra, Catalonia: Universitat Autònoma de Barcelona; 2014

[93] Liu Y, Derby B. Experimental study of the parameters for stable drop-on-demand inkjet performance. *Physics of Fluids*. 2019;**31**(3):32004. DOI: 10.1063/1.5085868

[94] Delrot P, Modestino MA, Gallaire F, Psaltis D, Moser C. Inkjet printing of viscous monodisperse microdroplets by laser-induced flow focusing. *Physical Review Applied*. 2016;**6**(2):24003. Available from: <https://link.aps.org/doi/10.1103/PhysRevApplied.6.024003>

[95] Du Z, Yu X, Han Y. Inkjet printing of viscoelastic polymer inks. *Chinese Chemical Letters*. 2018;**29**(3):399-404. Available from: <https://www.sciencedirect.com/science/article/pii/S100184171730373X>

[96] Lee C, Kang BJ, Oh JH. High-resolution conductive patterns fabricated by inkjet printing and spin coating on wettability-controlled surfaces. *Thin Solid Films*. 2016;**616**:238-246. Available from: <https://www.sciencedirect.com/science/article/pii/S0040609016304497>

[97] Soltman D, Subramanian V. Inkjet-printed line morphologies and temperature control of the coffee ring effect. *Langmuir*. 2008;**24**(5):2224-2231. DOI: 10.1021/la7026847

[98] Trantidou T, Elani Y, Parsons E, Ces O. Hydrophilic surface modification of PDMS for droplet microfluidics using a simple, quick, and robust method via PVA deposition. *Microsystems & Nanoengineering*. 2017;**3**(1):16091. DOI: 10.1038/micronano.2016.91

[99] Eom JS, Kim SH. Plasma surface treatment of polyimide for adhesive Cu/80Ni20Cr/PI flexible copper clad laminate. *Thin Solid Films*. 2008;**516**(14):4530-4534. Available from: <https://www.sciencedirect.com/science/article/pii/S0040609008001077>

- [100] Yang S-Y, Yang H-X, Hu A-J. Chapter 4- super engineering plastics and forms. Advanced Polyimide Materials. In: Yang S-Y, editor. Amsterdam, Netherlands: Elsevier; 2018. pp. 137-193
- [101] Cruz S, Rocha L, Viana J. Enhanced printability of thermoplastic polyurethane substrates by silica particles surface interactions. *Applied Surface Science*. 2015;**360**:198-206
- [102] Abu-Khalaf J, Al-Ghussain L, Nadi A, Sarairoh R, Rabayah A, Altarazi S, et al. Optimization of geometry parameters of inkjet-printed silver nanoparticle traces on PDMS substrates using response surface methodology. *Materials*. 2019;**12**(20):3329
- [103] Podhajny RM. Corona treatment of polymeric films. *Journal of Plastic Film & Sheeting*. 1988;**4**(3):177-188. DOI: 10.1177/875608798800400303
- [104] Schlozer R. The top 4 drying methods for inkjet. *Inkjet Insight*. 2020. Available from: <https://inkjetinsight.com/knowledge-base/the-top-4-drying-methods-for-inkjet/> [Internet]
- [105] Li Y, Yang Q, Li M, Song Y. Rate-dependent interface capture beyond the coffee-ring effect. *Scientific Reports*. 2016;**6**(1):24628. DOI: 10.1038/srep24628
- [106] Al-Milaji KN, Zhao H. New perspective of mitigating the coffee-ring effect: Interfacial assembly. *Journal of Physical Chemistry C*. 2019;**123**(19):12029-12041. DOI: 10.1021/acs.jpcc.9b00797
- [107] Majumder M, Rendall CS, Eukel JA, Wang JYL, Behabtu N, Pint CL, et al. Overcoming the “coffee-stain” effect by compositional Marangoni-flow-assisted drop-drying. *The Journal of Physical Chemistry. B*. 2012;**116**(22):6536-6542. DOI: 10.1021/jp3009628
- [108] Chuang MY. Inkjet printing of Ag nanoparticles using dimatix inkjet printer, No 2. technical report. United States: University of Pennsylvania; 2017
- [109] Abbas A, Bajwa I. Inkjet printing of Ag nanoparticles using Dimatix inkjet printer, No 1. Technical Report. United States: University of Pennsylvania; 2017
- [110] Mujal J, Ramon E, Diaz E, Carrabina J, Calleja Á, Martínez R, et al. Inkjet printed antennas for NFC systems. In: 2010 IEEE International Conference on Electronics, Circuits and Systems ICECS 2010- Proceeding; 2010. pp. 1220-1223
- [111] Sowade E, Mitra KY, Ramon E, Martinez-Domingo C, Villani F, Loffredo F, et al. Up-scaling of the manufacturing of all-inkjet-printed organic thin-film transistors: Device performance and manufacturing yield of transistor arrays. *Organic Electronics*. 2016;**30**:237-246. Available from: <http://www.sciencedirect.com/science/article/pii/S156611991530238X>
- [112] Ramon E, Sowade E, Martínez-Domingo C, Mitra KY, Alcalde A, Baumann RR, et al. Large-scale fabrication of all-inkjet-printed resistors and WORM memories on flexible polymer films with high yield and stability. *Flexible and Printed Electronics*. 2021;**6**(1):15003. DOI: 10.1088/2058-8585/abdb40
- [113] Scattareggia S. Inkjet application process development using functional fluids. IARIGAI: The International association of research organizations for the information, media and graphic arts industries. Finland: Aalto University; 2015. p. 23
- [114] Lindh M. Inkjet Deposition of Electrolyte: Towards Fully Printed Light-Emitting Electrochemical Cells. Umeå University; 2013

- [115] Patnaik DN, Subramanian V, Salahuddin SS. Three-dimensional structure formation via inkjet-printed metal nanoparticles: Ink and application development. Berkeley: University of California; 2018
- [116] Hamad AH, Salman MI, Mian A. Effect of driving waveform on size and velocity of generated droplets of nanosilver ink (Smartink). *Manufacturing Letters*. Elsevier. 2020;**24**:14-18
- [117] Kwon K-S, Jang M-H, Park HY, Ko H-S. An inkjet vision measurement technique for high-frequency jetting. *The Review of Scientific Instruments*. 2014;**85**(6):65101. DOI: 10.1063/1.4879824
- [118] Kwon J, Baek S, Lee Y, Tokito S, Jung S. Layout-to-bitmap conversion and design rules for inkjet-printed Large-scale integrated circuits. *Langmuir*. 2021;**37**(36):10692-10701. DOI: 10.1021/acs.langmuir.1c01296
- [119] Vila F, Pallarès J, Ramon E, Terés L. A systematic study of pattern compensation methods for all-inkjet printing processes. *IEEE Transactions on Components, Packaging and Manufacturing Technology*. 2016;**6**(4):630-636
- [120] Solar Cells Reimagined. [cited 2020 Sep 7]. Available from: <https://sauletech.com/>
- [121] Connolly KB. Johnnie Walker 'Smart Bottle' Performs for Consumers and Supply Chain [Internet]. 2015. Available from: <https://www.packagingdigest.com/beverage-packaging/johnnie-walker-smart-bottle-performs-for-consumers-and-supply-chain150306>
- [122] Jia H. Who will win the future of display technologies? *National Science Review*. 2018;**5**(3):427-431. DOI: 10.1093/nsr/nwy050
- [123] Hengge M, Livanov K, Zamoshchik N, Hermerschmidt F, List-Kratochvil EJW. ITO-free OLEDs utilizing inkjet-printed and low temperature plasma-sintered Ag electrodes. *Flexible and Printed Electronics*. 2021;**6**(1):15009. DOI: 10.1088/2058-8585/abe604
- [124] Jürgensen N, Pietsch M, Hai X, Schliske S, Hernandez-Sosa G. Green ink formulation for inkjet printed transparent electrodes in OLEDs on biodegradable substrates. *Synthetic Metals*. 2021;**282**:116930. Available from: <https://www.sciencedirect.com/science/article/pii/S0379677921002368>
- [125] Cinquino M, Prontera CT, Zizzari A, Giuri A, Pugliese M, Giannuzzi R, et al. Effect of surface tension and drying time on inkjet-printed PEDOT:PSS for ITO-free OLED devices. *Journal of Science: Advanced Materials and Devices*. 2022;**7**(1):100394. Available from: <https://www.sciencedirect.com/science/article/pii/S2468217921000708>
- [126] Lee SY, Lee G, Kim DY, Jang SH, Choi I, Park J, et al. Investigation of high-performance perovskite nanocrystals for inkjet-printed color conversion layers with superior color purity. *APL Photonics*. 2021;**6**(5):56104. DOI: 10.1063/5.0044284
- [127] Triana MA, Hsiang E-L, Zhang C, Dong Y, Wu S-T. Luminescent nanomaterials for energy-efficient display and healthcare. *ACS Energy Letters*. 2022;**7**:1001-1020
- [128] Alamri AM, Leung S, Vaseem M, Shamim A, He J-H. Fully inkjet-printed photodetector using a graphene/perovskite/graphene Heterostructure. *IEEE Transactions on Electron Devices*. 2019;**66**(6):2657-2661
- [129] Schackmar F, Eggers H, Frericks M, Richards BS, Lemmer U,

- Hernandez-Sosa G, et al. Perovskite solar cells with all-inkjet-printed absorber and charge transport layers. *Adv. Materials and Technologies*. 2021;**6**(2):2000271. Available from: <https://onlinelibrary.wiley.com/doi/abs/10.1002/admt.202000271>
- [130] Sajedi-Moghaddam A, Rahmanian E, Naseri N. Inkjet-printing Technology for Supercapacitor Application: Current state and perspectives. *ACS Applied Materials & Interfaces*. 2020;**12**(31):34487-34504. DOI: 10.1021/acsami.0c07689
- [131] Sollami Delekta S, Laurila M-M, Mäntysalo M, Li J. Drying-mediated self-assembly of graphene for inkjet printing of high-rate Micro-supercapacitors. *Nano-Micro Letters*. 2020;**12**(1):40. DOI: 10.1007/s40820-020-0368-8
- [132] Sollami Delekta S, Adolfsson KH, Benyahia Erdal N, Hakkarainen M, Östling M, Li J. Fully inkjet printed ultrathin microsupercapacitors based on graphene electrodes and a nano-graphene oxide electrolyte. *Nanoscale*. 2019;**11**(21):10172-10177. DOI: 10.1039/C9NR01427F
- [133] Li Z, Ruiz V, Mishukova V, Wan Q, Liu H, Xue H, et al. Inkjet printed disposable high-rate on-paper Microsupercapacitors. *Advanced Functional Materials*. 2022;**32**(1):2108773. DOI: 10.1002/adfm.202108773
- [134] Giannakou P, Tas MO, Le Borgne B, Shkunov M. Water-transferred, inkjet-printed Supercapacitors toward conformal and epidermal energy storage. *ACS Applied Materials & Interfaces*. 2020;**12**(7):8456-8465. DOI: 10.1021/acsami.9b21283
- [135] Huang T-T, Wu W. Inkjet-printed wearable Nanosystems for self-powered technologies. *Advanced Materials Interfaces*. 2020;**7**(12):2000015. DOI: 10.1002/admi.202000015
- [136] VartaAG. Printed Electronics for Medical and Lesiure Use. 2020 [cited 2021 Aug 24]. Available from: <https://www.advancedbatteriesresearch.com/articles/20633/printed-electronics-for-medical-and-lesiure-use>
- [137] Gong S, Schwalb W, Wang Y, Chen Y, Tang Y, Si J, et al. A wearable and highly sensitive pressure sensor with ultrathin gold nanowires. *Nature Communications*. 2014;**5**:1-8
- [138] Yang Z, Wang D-Y, Pang Y, Li Y-X, Wang Q, Zhang T-Y, et al. Simultaneously detecting subtle and intensive human motions based on a silver nanoparticles bridged graphene strain sensor. *ACS Applied Materials & Interfaces*. 2018;**10**(4):3948-3954. DOI: 10.1021/acsami.7b16284
- [139] Pan L, Chortos A, Yu G, Wang Y, Isaacson S, Allen R, et al. An ultra-sensitive resistive pressure sensor based on hollow-sphere microstructure induced elasticity in conducting polymer film. *Nature Communications*. 2014;**5**(1):3002. DOI: 10.1038/ncomms4002
- [140] Shi J, Li X, Cheng H, Liu Z, Zhao L, Yang T, et al. Graphene reinforced carbon nanotube networks for wearable strain sensors. *Advanced Functional Materials*. 2016;**26**(13):2078-2084. DOI: 10.1002/adfm.201504804
- [141] Cardenas JA, Andrews JB, Noyce SG, Franklin AD. Carbon nanotube electronics for IoT sensors. *Nano Futures*. 2020;**4**(1):12001. DOI: 10.1088/2399-1984/ab5f20
- [142] Mousavi S, Howard D, Zhang F, Leng J, Wang CH. Direct 3D printing of highly anisotropic, flexible, constriction-resistive sensors for multidirectional

proprioception in soft robots. *ACS Applied Materials & Interfaces*. 2020;**12**:15631-15643

[143] Zare Y, Rhee KY. Simulation of percolation threshold, Tunneling distance, and conductivity for carbon nanotube (CNT)-reinforced nanocomposites assuming effective CNT concentration. *Polymers*. 2020;**12**(1):114. Available from: <https://www.mdpi.com/2073-4360/12/1/114>

[144] Chen Z, Wang Z, Li X, Lin Y, Luo N, Long M, et al. Flexible piezoelectric-induced pressure sensors for static measurements based on nanowires/graphene Heterostructures. *ACS Nano*. 2017;**11**(5):4507-4513. DOI: 10.1021/acsnano.6b08027

[145] Chen S, Wu N, Ma L, Lin S, Yuan F, Xu Z, et al. Noncontact heartbeat and respiration monitoring based on a hollow microstructured self-powered pressure sensor. *ACS Applied Materials & Interfaces*. 2018;**10**(4):3660-3667. DOI: 10.1021/acscami.7b17723

[146] Lipomi DJ, Vosgueritchian M, Tee BC-K, Hellstrom SL, Lee JA, Fox CH, et al. Skin-like pressure and strain sensors based on transparent elastic films of carbon nanotubes. *Nature Nanotechnology*. 2011;**6**(12):788-792. DOI: 10.1038/nnano.2011.184

[147] Farooqui MF, Shamim A. Low cost inkjet printed smart bandage for wireless monitoring of chronic wounds. *Scientific Reports*. 2016;**6**(1):28949. DOI: 10.1038/srep28949

[148] Kuzubasoglu BA, Sayar E, Bahadir SK. Inkjet-printed CNT/PEDOT:PSS temperature sensor on a textile substrate for wearable intelligent systems. *IEEE Sensors Journal*. 2021;**21**(12):13090-13097

[149] Lo L-W, Zhao J, Wan H, Wang Y, Chakrabartty S, Wang C. An inkjet-printed PEDOT:PSS-based stretchable conductor for wearable health monitoring device applications. *ACS Applied Materials & Interfaces*. 2021;**13**(18):21693-21702. DOI: 10.1021/acscami.1c00537

[150] Ryu G, You J, Kostianovskii V, Lee E, Kim Y, Park C, et al. Flexible and printed PPG sensors for estimation of drowsiness. *IEEE Transactions on Electron Devices*. 2018;**65**(7):2997-3004

[151] Gupta R. Biomedical sensors and their interfacing. *Smart Sensors, Measurement and Instrumentation*. 2017;**25**:219-248

[152] Welch KC, Kulkarni AS, Jimenez AM, Douglas B. Wearable sensing devices for human-machine interaction systems. In: 2018 United States National Committee of URSI National Radio Science Meeting (USNC-URSI NRSM); 2018. pp. 1-2

[153] Liao Y, Zhang R, Wang H, Ye S, Zhou Y, Ma T, et al. Highly conductive carbon-based aqueous inks toward electroluminescent devices{,} printed capacitive sensors and flexible wearable electronics. *RSC Advances*. 2019;**9**(27):15184-15189. DOI: 10.1039/C9RA01721F

[154] Mass M, Veiga LS, Garate O, Longinotti G, Moya A, Ramón E, et al. Fully inkjet-printed biosensors fabricated with a highly stable ink based on carbon nanotubes and enzyme-functionalized nanoparticles. *Nanomaterials*. 2021;**11**(7):1645

[155] Schultz A, Knoll T, Urban A, Schuck H, von Briesen H, Germann A, et al. Novel cost-efficient graphene-based impedance biosensor for the analysis of viral Cytopathogenicity and

the effect of antiviral drugs. *Frontiers in Bioengineering and Biotechnology*. 2021;**9**:718889. Available from: <https://pubmed.ncbi.nlm.nih.gov/34381768>

[156] Bihar E, Wustoni S, Pappa AM, Salama KN, Baran D, Inal S. A fully inkjet-printed disposable glucose sensor on paper. *npj Flexible Electronics*. 2018;**2**(1):30. DOI: 10.1038/s41528-018-0044-y

[157] Wang L, Wu Z, Cao C. Technologies and fabrication of intelligent packaging for perishable products. *Applied Sciences*. 2019;**9**(22):4858

[158] Urbano O, Perles A, Pedraza C, Rubio-Arraez S, Castelló ML, Ortola MD, et al. Cost-effective implementation of a temperature traceability system based on smart RFID tags and IoT services. *Sensors*. 2020;**20**(4):1163

[159] Zikulnig J, Hirschl C, Rauter L, Krivec M, Lammer H, Riemelmoser F, et al. Inkjet printing and characterisation of a resistive temperature sensor on paper substrate. *Flexible and Printed Electronics*. 2019;**4**(1):15008. DOI: 10.1088/2058-8585/ab0cea

[160] Quintero AV, Molina-Lopez F, Smits ECP, Danesh E, van den Brand J, Persaud K, et al. Smart RFID label with a printed multisensor platform for environmental monitoring. *Flexible and Printed Electronics*. 2016;**1**(2):25003. DOI: 10.1088/2058-8585/1/2/025003

[161] Baumbauer CL, Anderson MG, Ting J, Sreekumar A, Rabaey JM, Arias AC, et al. Printed, flexible, compact UHF-RFID sensor tags enabled by hybrid electronics. *Scientific Reports*. 2020;**10**(1):16543. DOI: 10.1038/s41598-020-73471-9

[162] Machiels J, Appeltans R, Bauer DK, Segers E, Henckens Z, Van Rompaey W,

et al. Screen printed antennas on Fiber-based substrates for sustainable HF RFID assisted E-fulfilment smart packaging. *Materials*. 2021;**14**(19):5500

[163] Huang Q, Zhu Y. Printing conductive nanomaterials for flexible and stretchable electronics: A review of materials, processes, and applications. *Advanced Materials Technologies*. 2019;**4**(5):1-41

[164] Abdolmaleki H, Kidmose P, Agarwala S. Droplet-based techniques for printing of functional inks for flexible physical sensors. *Advanced Materials*. 2021;**33**(20):2006792. DOI: 10.1002/adma.202006792

[165] Wiklund J, Karakoç A, Palko T, Yiğitler H, Ruttik K, Jäntti R, et al. A review on printed electronics: Fabrication methods, inks, substrates, applications and environmental impacts. *Journal of Manufacturing and Materials Processing*. 2021;**5**(3):89

[166] Guo Y, Patanwala HS, Bognet B, Ma AWK. Inkjet and inkjet-based 3D printing: Connecting fluid properties and printing performance. *Rapid Prototyping Journal*. 2017;**23**(3):562-576. DOI: 10.1108/RPJ-05-2016-0076